ISTANBUL TECHNICAL UNIVERSITY ★ GRADUATE SCHOOL OF SCIENCE ENGINEERING AND TECHNOLOGY

ELECTROSPUN CARBON NANOFIBER BASED COMPOSITES AS ANODE MATERIAL FOR LITHIUM-ION BATTERIES

Ph.D. THESIS

Mahmut DİRİCAN

Department of Nanoscience and Nanoengineering

Nanoscience and Nanoengineering Programme

NOVEMBER 2015

ISTANBUL TECHNICAL UNIVERSITY ★ GRADUATE SCHOOL OF SCIENCE ENGINEERING AND TECHNOLOGY

ELECTROSPUN CARBON NANOFIBER BASED COMPOSITES AS ANODE MATERIAL FOR LITHIUM-ION BATTERIES

Ph.D. THESIS

Mahmut DİRİCAN
(513102007)

Department of Nanoscience and Nanoengineering

Nanoscience and Nanoengineering Programme

Thesis Advisor: Assoc. Prof. Dr. Hüseyin KIZIL

NOVEMBER 2015

İSTANBUL TEKNİK ÜNİVERSİTESİ ★ FEN BİLİMLERİ ENSTİTÜSÜ

LİTYUM-İYON BATARYALAR İÇİN ELEKTRO EĞİRME YÖNTEMİYLE ÜRETİLMİŞ CARBON NANOLİF TABANLI KOMPOZİT ANOT MALZEMELERİ

DOKTORA TEZİ

Mahmut DİRİCAN
(513102007)

Nanobilim ve Nanomühendislik Anabilim Dalı

Nanobilim ve Nanomühendislik Programı

Tez Danışmanı: Doç. Dr. Hüseyin KIZIL

KASIM 2015

Mahmut Dirican, a Ph.D. student of ITU Graduate School of Science, Engineering and Technology student ID 513102007, successfully defended the dissertation entitled "ELECTROSPUN CARBON NANOFIBER BASED COMPOSITES AS ANODE MATERIAL FOR LITHIUM-ION BATTERIES", which he prepared after fulfilling the requirements specified in the associated legislations, before the jury whose signatures are below.

Thesis Advisor : **Assoc. Prof. Dr. Hüseyin KIZIL** ....
Istanbul Technical University

Jury Members : **Prof. Dr. Levent TRABZON** ....
Istanbul Technical University

Prof. Dr. Hüseyin ÇİMENOĞLU ....
Istanbul Technical University

Prof. Dr. Ayhan BOZKURT ....
Fatih University

Prof. Dr. Ayhan MERGEN ....
Marmara University

Date of Submission : 11 September 2015
Date of Defense : 24 November 2015

To my beloved parents and family,

FOREWORD

I would like to express my sincerest appreciation to my advisor Assoc. Prof. Dr. Hüseyin Kızıl for his supervising, supporting and teaching of the philosophy to do good research during my Ph.D. studies. I also would like to offer my sincere gratitude to Prof. Xiangwu Zhang for his guidance, encouragement and patience throughout the course of this research. My experience of working with them had a profound impact on me as an individual as well as a scientist. I also would like to thank Prof. Levent Trabzon and Prof. Ayhan Bozkurt for serving on my advisory committee and their guidance.

I would like to acknowledge the Council of Higher Education of Turkey for financially supporting me through my Ph.D. studies.

I would like to thank Mr. Mümin Balaban, Mr. Emre Altınağac, and Mr. Muhammet Bekin at Istanbul Technical University for their cooperation and support during my Ph.D. study. I also would like to thank Dr. Philip D. Bradford, Dr. Meltem Yanılmaz, Dr. Kun Fu, Dr. Shu Zhang, Mr. Özkan Yıldız, Mr. Yao Lu, Mr. Han Jiang, Ms. Yeqian Ge, Mr. Chen Chen, Mr. Jiadeng Zhu, Mr. Guanjie Xu, Ms. Ying Ji, Ms. Xiaomeng Fang, Mr. Yavuz Çaydamlı, and Alper Gürarslan at North Carolina State University for their earnest cooperation and warmhearted support during the periods of my research.

Finally, I would like to thank all those people who gave me emotional support during this work and throughout my life.

November 2015 Mahmut DİRİCAN
(Research Assistant)

TABLE OF CONTENTS

Page

FOREWORD ... **ix**
TABLE OF CONTENTS ... **xi**
ABBREVIATIONS ... **xiii**
LIST OF TABLES ... **xv**
LIST OF FIGURES ... **xviii**
SUMMARY ... **xxiii**
ÖZET ... **xxv**
1. INTRODUCTION ... **1**
- 1.1 Overview of Electrochemical Energy Storage and Conversion Systems ... 1
- 1.2 Overview of Lithium-Ion Batteries ... 2
  - 1.2.1 Introduction ... 2
  - 1.2.2 Cathodes ... 5
    - 1.2.2.1 Layered lithium transition metal oxides ... 5
    - 1.2.2.2 Lithium manganese oxides spinels ... 6
    - 1.2.2.3 Lithium transition-metal phosphate ... 7
  - 1.2.3 Anodes ... 8
    - 1.2.3.1 Carbonaceous materials ... 10
    - 1.2.3.2 Tin-based anode materials ... 15
    - 1.2.3.3 Silicon ... 17
    - 1.2.3.4 Cobalt oxide ... 23
    - 1.2.3.5 Manganese oxide ... 25
    - 1.2.3.6 Titanium oxide ... 26
  - 1.2.4 Electrolytes ... 27
- 1.3 Overview of Electrospinning Process ... 29
  - 1.3.1 Introduction ... 29
  - 1.3.2 Applications of electrospun nanofibers ... 31
  - 1.3.3 Polyacrylonitrile as a precursor to carbon fibers ... 32
  - 1.3.4 Polyvinyl alcohol as a precursor to carbon nanofiber composites ... 35

2. RESEARCH OBJECTIVES ... **37**
3. CARBON-ENHANCED ELECTRODEPOSITED SnO_2/CARBON NANOFIBER COMPOSITES AS ANODE FOR LITHIUM-ION BATTERIES ... **41**
- 3.1 Introduction ... 41
- 3.2 Experimental ... 44
  - 3.2.1 Chemicals and reagents ... 44
  - 3.2.2 Electrospinning and carbonization of nonporous carbon nanofibers ... 44
  - 3.2.3 Electrospinning and carbonization of porous carbon nanofibers ... 44
  - 3.2.4 Electrodeposition and CVD coating of nonporous and porous carbon nanofibers ... 45
  - 3.2.5 Structure characterization ... 45
  - 3.2.6 Electrochemical evaluation ... 46

3.3 Results and Discussion 46
3.3.1 Morphology and structure 46
3.3.2 Electrochemical performance 52
3.4 Conclusions 57
4. CARBON-CONFINED PVA-DERIVED SILICON/SILICA/CARBON NANOFIBER COMPOSITES AS ANODE FOR LITHIUM-ION BATTERIES 59
4.1 Introduction 59
4.2 Experimental 61
4.2.1 Nanofiber preparation 61
4.2.2 Structure characterization 62
4.2.3 Electrochemical evaluation 62
4.3 Results and Discussion 62
4.3.1 Morphology and structure 62
4.3.2 Electrochemical performance 69
4.4 Conclusions 74
5. FLEXIBLE BINDER-FREE SILICON/SILICA/CARBON NANOFIBER COMPOSITES AS ANODE FOR LITHIUM-ION BATTERIES 75
5.1 Introduction 75
5.2 Experimental 77
5.2.1 Nanofiber preparation 77
5.2.2 Structure characterization 78
5.2.3 Mechanical testing 78
5.2.4 Electrochemical evaluation 78
5.3 Results and Discussion 79
5.3.1 Morphology and structure 79
5.3.2 Mechanical properties 86
5.3.3 Electrochemical performance 87
5.4 Conclusions 92
6. SiO_2-CONFINED SILICON/CARBON NANOFIBER COMPOSITES AS ANODE FOR LITHIUM-ION BATTERIES 95
6.1 Introduction 95
6.2 Experimental 97
6.2.1 Nanofiber preparation 97
6.2.2 Structure characterization 98
6.2.3 Electrochemical evaluation 98
6.3 Results and Discussion 99
6.3.1 Morphology and structure 99
6.3.2 Electrochemical performance 105
6.4 Conclusions 112
7. CONCLUSIONS AND RECOMMENDATIONS 113
7.1 Conclusions 113
7.2 Recommendation for Future Work 117
REFERENCES 119
CURRICULUM VITAE 135

ABBREVIATIONS

ALD : Atomic layer deposition
CNFs : Carbon nanofibers
CNTs : Carbon nanotubes
CVD : Chemical vapor deposition
DEC : Diethyl carbonate
DMF : *N,N*-dimethylformamide
EDS : Energy-dispersive X-Ray spectroscopy
EC : Ethylene carbonate
EMC : Ethylmethyl carbonate
FTIR : Fourier transform infrared spectroscopy
FESEM : Field emission scanning electron microscopy
MWCNT : Multi-wall carbon nanotube
PLD : Pulsed laser deposition
PAN : Polyacrylonitrile
PA : Polyamide
PE : Polyethylene
PEO : Polyethylene oxide
PI : Polyimide
PS : Polystyrene
PVC : Polyvinylchloride
PVDF : Poly(vinylidene fluoride)
PVA : Polyvinyl alcohol
SEM : Scanning electron microscopy
SWCNT : Single-wall carbon nanotube
SEI : Solid electrolyte interface
TEM : Transmission electron microscope
TEOS : Tetraethyl orthosilicate
XRD : X-Ray diffraction

LIST OF TABLES

Page

Table 1.1 : Comparisons between different anode materials 9
Table 3.1 : Compositions of nanofiber composites based on element analysis measurement. 48

LIST OF FIGURES

Page

Figure 1.1 : Simplified Ragone plot of the energy storage domains for the various electrochemical energy conversion systems compared to an internal combustion engine and turbines and conventional capacitors [3]……... 2
Figure 1.2 : Comparison of the different battery technologies in terms of volumetric and gravimetric energy density [4]…………………………………….. 3
Figure 1.3 : Schematic of a lithium-ion battery [9]. 4
Figure 1.4 : Structure of layered lithiated transition metal oxides, $LiMO_2$ (M = Ni, Co, Mn) [13]………………………………………………………… 6
Figure 1.5 : Structure of the cubic spinel $LiMn_2O_4$ [13]……………………………..7
Figure 1.6 : Structure of olivine $LiFePO_4$ [13]……………………………………… 8
Figure 1.7 : Potentials and charge densities of candidate anode materials. On the right are presented salient features of the lithium-ion battery technology [28]………………………………………………………………10
Figure 1.8 : Schematic representation of the structure of graphitizing (but non-graphitic) carbon (A) and non-graphitizing carbon (B) [30]………… 11
Figure 1.9 : Schematic of lithium intercalation in graphite. (A) Lithium is inserted in every 2nd carbon hexagon and (B) between the graphite layers [9]…..11
Figure 1.10 : Charge-discharge curves for CNFs anode at 0.1 and 10 C rates [39].. 14
Figure 1.11 : Structures of different phases in the Li-Sn system [47]……………...16
Figure 1.12 : Galvanostatic charge-discharge profiles for a micro-Si (10 μm particle) anode [8]…………………………………………………………...18
Figure 1.13 : Schematic of the materials design. (A) A conventional slurry coated SiNP electrode. (B) A novel Si@void@C electrode. The void space between each Si nanoparticles and the nanoscale carbon coating layer allows the Si to expand without rupturing the coating layer, which ensures that a stable and thin SEI layer forms on the outer surface of the carbon. Also, the volume change of the Si nanoparticles is accommodated in the void space and does not change the microstructure of the electrode. (C) A magnified schematic of an individual Si@void@C particle showing that the Si nanoparticle expands without breaking the carbon coating or disrupting the SEI layer on the outer surface [83]……………………………………..20
Figure 1.14 : Electrochemical cycling results for Si@void@C electrodes. Delithiation capacity and coulomb efficiency of the first 1000 galvanostatic cycles between 0.01−1 V. The rate was C/10 for one cycle, then C/3 for 10 cycles, and 1C for the later cycles [82]……… 21
Figure 1.15 : Electrochemical characteristics of DWSiNTs tested between 1 V and 0.01 V. Capacity retention of different silicon nanostructures (a). All samples were cycled at the same charge/discharge rate of C/5. The calendar life and delithiation capacity of DWSiNTs can also be seen in this figure. Lithiation/delithiation capacity and coulombic efficiency of DWSiNTs cycled at 12C for 6,000 cycles (b). Voltage profiles plotted

for the 1st, 1,000th, 2,000th, 3,000th and 6,000th cycles (c). Galvanostatic charge/discharge profiles (d) and capacity (e) of DWSiNTs cycled at various rates from 1C to 20C [84]…………….. 22
Figure 1.16 : Schematic illustration (cross sectional views along both directions perpendicular (top) and parallel (bottom) to the tube axis) of the self-supported topotactic transformation process for formation of needlelike Co_3O_4 nanotubes. a) Single-crystalline β-$Co(OH)_2$ nanoneedles grown along [001] direction. b) After surface reconstruction, loose platelet-walls form with possibly some Co_3O_4 nanoparticles (black dots) intercalated. c) Co_3O_4 nanotubes with compact wall, overall tube axis is [111] [86]……………………………………………………..24
Figure 1.17 : Morphology and structure characterization of the self-supporting Co_3O_4. (a) Low-magnification SEM image, the inset is a side view. (b) High-magnification SEM image [90]……………………………...25
Figure 1.18 : a) Structure of $Li_4Ti_5O_{12}$ and $Li_7Ti_5O_{12}$, showing no volume change after charge and discharge. b) Scanning electron microscopy under low and high magnification of MSNP-LTO, showing secondary and primary particles. c,d) Charge and discharge curves of micron-size LTO and MSNP-LTO, respectively. The test was carried out in half cell. Initially, half cells were charged and discharged at 0.2-C rate, and then they were charged at 1-C rate and discharged at different rates [97]…………………………………………………………... 27
Figure 1.19 : Comparison of the diameters of electrospun fibers and biological and technological objects [107]……………………………………….. 29
Figure 1.20 : A) Schematic diagram showing a laboratory setup for electrospinning. B) Photograph of an electrospinning jet captured by a high-speed video showing the bending instability of the jet [112]……………………...30
Figure 1.21 : Different electrospun fiber morphologies: (A) beaded, (B) ribbon, (C) porous fibers, and (D) core-shell [113]……………………………… 31
Figure 1.22 : Molecular structure of PAN [123]…………………………………... 32
Figure 1.23 : PAN precursor carbon fiber conversion process [123]……………… 33
Figure 1.24 : Proposed chemistry of PAN stabilization [123]……………………...34
Figure 1.25 : Structure changes for PAN precursor during carbonization [124]…...35
Figure 1.26 : FESEM images of (a) Si/PVA nanofiber composite and (b) Si/PVA-derived carbon composite (the inset shows XRD patterns of nano-Si/C composite) [128]……………………………………………………...36
Figure 3.1 : Schematic illustration of the fabrication processes of SnO_2@CNF (A), SnO_2@CNF@C (B), SnO_2@PCNF (C), and SnO_2@PCNF@C (D) composites………………………………………………………… 43
Figure 3.2 : FTIR spectra of CNFs (A) and oxidized CNFs (B)…………………... 47
Figure 3.3 : EDS spectrum of SnO_2@PCNF@C composite……………………… 48
Figure 3.4 : SEM images of SnO_2@CNF (A), SnO_2@CNF@C (B), SnO_2@PCNF (C), and SnO_2@PCNF@C (D) composites…………………………... 49
Figure 3.5 : SEM images of SnO_2@CNF (A), SnO_2@CNF@C (B), SnO_2@PCNF (C), and SnO_2@PCNF@C (D) composites…………………………... 50
Figure 3.6 : SEM images of SnO_2@CNF (A), SnO_2@CNF@C (B), SnO_2@PCNF (C), and SnO_2@PCNF@C (D) composites…………………………... 51
Figure 3.7 : WAXD patterns of CNFs (A), SnO_2@CNF (un-calcined) (B), SnO_2@CNF (C), and SnO_2@CNF@C (D) composites……………….52

Figure 3.8 : Galvanostatic charge-discharge profiles of (A) CNF@SnO_2, (B) CNF@SnO_2@C, (C) PCNF@SnO_2, and (D) PCNF@SnO_2@C composites…………………………………………………………… 53
Figure 3.9 : Cycling performance comparison of CNFs, CNF@SnO_2, and CNF@SnO_2@C composites……….. 55
Figure 3.10 : Cycling performance comparison of PCNFs, PCNF@SnO_2, and PCNF@SnO_2@C composites……………………………………….. 56
Figure 3.11 : Rate capability of PCNF@SnO_2@C composite cycled at different current densities……………………………………………………57
Figure 4.1 : Schematic illustration of the fabrication process of Si/SiO2/PVA nanofibers (I), Si/SiO2/C nanofibers (II), and CVD carbon-coated Si/SiO2/C nanofibers (III)…………………………………………… 61
Figure 4.2 : FTIR spectra of PVA nanofibers, SiO_2/PVA nanofibers, Si/SiO_2/PVA nanofibers, Si/SiO_2/C nanofibers, and CVD carbon-coated Si/SiO_2/C nanofibers……………………………………………………….. 64
Figure 4.3 : Schematic of SiO_2/PVA network structure…………………………… 65
Figure 4.4 : SEM images of Si/SiO_2/PVA nanofibers (A), Si/SiO_2/C nanofibers (B), and CVD carbon-coated Si/SiO_2/C nanofibers (C)……………………66
Figure 4.5 : TEM images of SiO_2/C nanofibers (A), Si/SiO_2/C nanofibers (B), CVD carbon-coated Si/SiO_2/C nanofibers (C), and high-magnification TEM image of CVD carbon-coated Si/SiO_2/C nanofibers (D)……………... 67
Figure 4.6 : WAXD patterns of Si/SiO_2/C nanofibers and CVD carbon-coated Si/SiO_2/C nanofibers…………………………………………………..68
Figure 4.7 : Raman spectra of Si/SiO_2/C nanofibers and CVD carbon-coated Si/SiO_2/C nanofibers…………………………………………………..69
Figure 4.8 : Galvanostatic charge-discharge profiles of Si/C nanofibers (A), Si/SiO_2/C nanofibers (B), and CVD carbon-coated Si/SiO_2/C nanofibers (C)………………………………………………………………….. 71
Figure 4.9 : Cycling performance (A) and coulombic efficiencies (B) of Si/C nanofibers, Si/SiO_2/C nanofibers, and CVD carbon-coated Si/SiO_2/C nanofibers……………………………………………………………...72
Figure 4.10 : Rate capability of CVD carbon-coated Si/SiO_2/C nanofibers cycled at different current densities……………………………………………74
Figure 5.1 : Schematic illustration of the fabrication process of flexible Si/SiO_2/PAN nanofibers, flexible Si/SiO_2/C nanofibers, and CVD carbon-coated flexible Si/SiO_2/C nanofibers…………………………………………78
Figure 5.2 : Thermogravimetric analysis curves of flexible SiO_2/C nanofibers, inflexible Si/C nanofibers, flexible Si/SiO_2/C nanofibers, and CVD carbon-coated flexible Si/SiO_2/C nanofibers…………………………80
Figure 5.3 : Photographs of a flexible Si/SiO_2/C nanofiber mat. Free-standing, flexible Si/SiO_2/C nanofibers can be folded without any structural damage……………………………………………………………... 81
Figure 5.4 : SEM images of flexible SiO_2/C nanofibers (A), inflexible Si/C nanofibers (B), flexible Si/SiO_2/C nanofibers (C), and CVD carbon-coated flexible Si/SiO_2/C nanofibers (D)…………………………...82
Figure 5.5 : TEM images of flexible SiO_2/C nanofibers (A), inflexible Si/C nanofibers (B), flexible Si/SiO_2/C nanofibers (C), and CVD carbon-coated flexible Si/SiO_2/C nanofibers (D)…………………………...83
Figure 5.6 : High-magnification TEM image of a CVD carbon-coated flexible Si/SiO_2/C nanofiber………………………………………………... 84

Figure 5.7 : FTIR spectra of flexible Si/SiO_2/PAN nanofibers (1), flexible SiO_2/C nanofibers (2), inflexible Si/C nanofibers (3), flexible Si/SiO_2/C nanofibers (4), and CVD carbon-coated flexible Si/SiO_2/C nanofibers (5)………………………………………………………………….. 85
Figure 5.8 : WAXD patterns of inflexible Si/C nanofibers (1), flexible Si/SiO_2/C nanofibers (2), and CVD carbon-coated flexible Si/SiO_2/C nanofibers (3)…………………………………………………………………...86
Figure 5.9 : Mechanical properties. (A) typical tensile stress-strain curves of flexible Si/SiO_2/C nanofibers and inflexible Si/C nanofibers; (B) photograph of inflexible Si/C nanofibers during compression test, inset shows the visible crack on the tested sample; (C) photograph of flexible Si/SiO_2/C nanofibers sample while compression test, inset shows undamaged sample after testing…………………………………………………87
Figure 5.10 : Galvanostatic charge-discharge profiles of inflexible Si/C nanofibers, flexible Si/SiO_2/C nanofibers, and CVD carbon-coated flexible Si/SiO_2/C nanofibers for first (A), second (B), fifth (C), and fiftieth (D) cycles……………………………………………………………89
Figure 5.11 : Cycling performance (A) and coulombic efficiencies (B) of inflexible Si/C nanofibers, flexible Si/SiO_2/C nanofibers, CVD carbon-coated flexible Si/SiO_2/C nanofibers, and flexible SiO_2/C nanofibers………91
Figure 5.12 : Rate capability (A) and coulombic efficiency (B) of CVD carbon-coated flexible Si/SiO_2/C nanofibers cycled at different current densities…………………………………………………………92
Figure 6.1 : Schematic illustration of the fabrication process of electrospun Si@PAN nanofibers, Si@C nanofibers, and Si@C-SiO_2 nanofibers……………98
Figure 6.2 : SEM images of Si@C nanofiber composite (A) and Si@C-SiO_2 nanofiber composites with different coating times: (B) 0.5 h, (C) 1 h, and (D) 2h……………………..100
Figure 6.3 : TEM images of Si@C nanofiber composite (A) and Si@C-SiO_2 nanofiber composites with different coating times: (B) 0.5 h, (C) 1 h, and (D) 2h…………………………………………………………101
Figure 6.4 : High-magnification TEM images of Si@C nanofiber composite (A) and Si@C-SiO_2 nanofiber composites with different coating times: (B) 0.5 h, (C) 1 h, and (D) 2h……………………………………………...102
Figure 6.5 : TEM images of Si@C nanofiber composite (A) and Si@C-SiO_2 nanofiber composites with different coating times: (B) 0.5 h, (C) 1 h, and (D) 2h…………………………………………………………103
Figure 6.6 : WAXD patterns of Si@C nanofiber composite (1) and Si@C-SiO_2 nanofiber composites with different coating times: (2) 0.5 h, (3) 1 h, and (4) 2h……………………………………………………………104
Figure 6.7 : Raman spectra of Si@C nanofiber composite (1) and Si@C-SiO_2 nanofiber composites with different coating times: (2) 0.5 h, (3) 1 h, and (4) 2h……………………………………………………………105
Figure 6.8 : Galvanostatic charge-discharge profiles of Si@C nanofiber composite (A) and Si@C-SiO_2 nanofiber composites with different coating times: (B) 0.5 h, (C) 1 h, and (D) 2h…………………………………….. 106
Figure 6.9 : Cycling performance (A) and coulombic efficiencies (B) of Si@C nanofiber composite and Si@C-SiO_2 nanofiber composites with different coating times: 0.5 h, 1 h, and 2h………………………….. 108

Figure 6.10 : Coulombic efficiencies of Si@C nanofiber composite and Si@C-SiO_2 nanofiber composites with different coating times: 0.5 h, 1 h, and 2h with a cutoff voltage window of 0.01 and 1.0 V……………………109

Figure 6.11 : Rate capability of Si@C-SiO_2 nanofiber composite with 0.5 h coating time cycled at different current densities…………………………... 110

Figure 6.12 : TEM images of cycled Si@C nanofiber composite (A) and Si@C-SiO_2 nanofiber composites with different coating times: (B) 0.5 h, (C) 1 h, and (D) 2h after 50 cycles……………………………………….. 111

ELECTROSPUN CARBON NANOFIBER BASED COMPOSITES AS ANODE MATERIAL FOR LITHIUM-ION BATTERIES

SUMMARY

Among the various currently-used rechargeable battery technologies, rechargeable lithium-ion batteries are considered as the most promising rechargeable batteries in recent years because of their distinguished properties such as high energy density, long cycle life, good thermal stability, no memory effect and good power performance. Exploring high-capacity electrode materials for lithium-ion batteries is crucial for technological improvements on mobile electronic devices, large-scale smart grids and electric vehicle technologies using lithium-ion batteries as the power source. Current commercial lithium-ion batteries use graphitic materials in the anode. However, the theoretical capacity (372 mAh g^{-1}) of graphitic anode materials cannot meet the ever-growing capacity requirements of future portable electronics and electric vehicle technologies. Lithium storage capacities of alloy-type anodes (e.g., silicon, tin, germanium, and their oxides) are much higher than that of currently used intercalation-type graphite anode. Among different alloy-type anodes, Si and tin dioxide (SnO_2) are considered as the most promising candidates for next-generation lithium-ion batteries because of their high gravimetric and volumetric capacities. In this work, we focused on fabricating novel composite nanofibers and exploring their potential applications as anode materials for new-generation, high-performance rechargeable lithium-ion batteries. In one of the studies, we introduced carbon-enhanced binder-free SnO_2-electrodeposited carbon nanofibers (CNF@SnO_2) and SnO_2-electrodeposited porous carbon nanofiber (PCNF@SnO_2) composites that can sustain their structural stability during repeated charge-discharge cycling. Combination of porous nanofiber structure and nanoscale carbon confinement led to a novel carbon-coated PCNF@SnO_2 composite anode with high capacity retention and large coulombic efficiency. In another study, novel carbon-confined polyviniyl alcohol (PVA)-derived silicon/silica/carbon nanofiber composite anodes with improved electrochemical performance were successfully fabricated for high-capacity lithium-ion batteries. High-energy, flexible lithium-ion batteries become critically important with technological improvements on portable and bendable electronic equipment such as rollup displays, implantable medical devices, active radio-frequency identification tags, and wearable devices. Hence, we introduced flexible silicon/silica/carbon (Si/SiO_2/C) nanofiber composite anode materials with superior electrochemical performance for next-generation flexible and high-energy lithium-ion batteries. We also introduced nanoscale silica-coated silicon/carbon (Si@C-SiO_2) nanofiber composites that can maintain their structural stability during repeated cycling. Nanoscale SiO_2 coating of Si@C nanofibers helped preserve the Si particles within the nanofiber structure, resulting in stable solid electrolyte interphase formation and improved cycling performance. Results indicate that novel composite nanofiber anodes with increased reversible capacity and enhanced capacity retention were successfully developed for next-generation lithium-ion batteries. Hopefully, introduced anode designs will open up new opportunities to develop high-performance electrode materials for next-generation lithium-ion batteries, which are the outstanding

energy storage systems for addressing the developing challenge of the sustainable energy sources and reducing the consumption of fossil fuels.

LİTYUM-İYON BATARYALAR İÇİN ELEKTRO EĞİRME YÖNTEMİYLE ÜRETİLMİŞ CARBON NANOLİF TABANLI KOMPOZİT ANOT MALZEMELERİ

ÖZET

Lityum-iyon bataryalar, yüksek enerji yoğunluğu, uzun ömürlü oluşu ve iyi güç performansı göstermesi vb. özelliklerinden dolayı mevcut şarj edilebilir batarya teknolojileri içerisinde en çok tercih edilen batarya tipi olarak öne çıkmaktadır. Son yıllarda cep telefonu ve dizüstü bilgisayar gibi taşınabilir cihazlar ve elektrikli arabalarda elde edilen teknolojik yeniliklerle beraber bu cihazların ihtiyaç duyduğu enerji gereksinimini sağlayacak lityum-iyon bataryalar için yüksek kapasitede anot malzemesi geliştirilmesi büyük önem arz etmektedir. Lityum iyonlarıyla alaşım oluşumu seklinde reaksiyon veren ve bu şekilde lityum iyon saklama özelliği bulunan lityum aktif malzemelerden oluşan anotların (silikon, kalay, germanyum ve oksitleri vb.) lityum depolama kapasitesi günümüzde ticari olarak kullanılan grafit tabanlı anotlardan (375 mAh g^{-1}) çok daha yüksektir. Örneğin anot olarak kullanılabilecek saf kalayın teorik kapasitesi 992 mAh g^{-1} iken bu değer silikonda 4200 mAh g^{-1}'a kadar ulaşabilmektedir. Ancak, lityum depolama kapasitesi yüksek olan bu aktif malzemelerin hacmi şarj işlemi (lityum iyonunu yapısına katması) esnasında büyük oranda artmaktadır. Örneğin silikonda oluşan hacim genişlemesi % 400 civarındayken, kalay için % 300 civarında hacim genişlemesi oluşmaktadır. Deşarj işlemiyle yapıdan lityum iyonunun çıkması sonucunda hacim genişlemesi kaybolmaktaysa da anot için yapısal bozunum (pulvarizasyon) kaçınılmazdır. Şarj-deşarj işlemi esnasında meydana gelen aktif malzemenin pulvarizasyonu stabil olmayan katı elektrolit ara yüz (SEI) oluşumunu ve iletkenlik sağlayıcı karbonla lityum aktif malzeme arasındaki elektronik iletkenliğin kaybolması sorunlarını beraberinde getirmektedir. Aktif malzemede meydana gelen bu problemlerden dolayı pil kapasitesi stabil olmamakta ve hızla düşmektedir.

Lityum aktif malzemelerde oluşan bu problemlerin önüne geçebilmek amacıyla değişik yapıda kompozit malzemelerden oluşan anotlar üzerine son zamanlarda çok sayıda çalışma yapılmaktadır. Bu çalışmaların büyük bir kısmını nano üretim teknikleri kullanılarak yeni anot malzemesi geliştirilmesi oluşturmaktadır. Yapılan çalışmalar sonucunda nano boyutlarda lityum aktif malzeme (Si, Sn vb.) kullanılması ve nano boyuttaki bu malzemelerin karbon yapıların içerisine homojen bir dağılımla hapsedilmesi şimdiye kadar en olumlu sonuçların alındığı metotlar olarak dikkat çekmektedir. Nano boyutta lityum aktif malzeme/karbondan oluşan kompozit anotlardaki lityum aktif malzeme bileşeni yüksek lityum depolama kapasitesine sahipken, karbon bileşeni ise mükemmel elektronik iletkenlik ve yapısal stabilite özelliği sağlamaktadır.

Bu çalışmada lityum-iyon bataryalarda kullanılmak üzere kompozit nanoliflerden oluşan, yüksek kapasiteli anot malzemeleri geliştirilmesi üzerine araştırmalar yapılmıştır. Bu amaçla kompozit nanoliflerden oluşan yeni anot malzemelerin üretimi

gerçekleştirilmiş ve elde edilen anotların elektrokimyasal performansları detaylı olarak analiz edilmiştir.

Lityum-iyon bataryalar için yüksek kapasitede anot geliştirilmesi üzerine yapılan çalışmalardan ilkinde dış yüzeyi nano mertebede (10 nm) amorf karbonla kaplanmış olan SnO_2/gözenekli karbon kompozit nanoliflerden oluşan anot malzemesi elde edilmesi üzerine deneysel çalışmalar yapılmıştır. Bu amaçla ilk olarak elektro eğirme ve karbonizasyon işlemleri sonucu gözenekli karbon nanolifler üretilmiştir. Elde edilen gözenekli yapıdaki karbon nanoliflerin yüzeyi elektro kaplama yöntemiyle SnO_2 nanoparçacıklarla kaplanarak yüksek kapasiteli anot oluşturulması amaçlanmıştır. Elektro kaplama işlemi için kullanılan karbon nanoliflerin gözenekli yapıda olması lif yüzeyine daha fazla SnO_2 kaplanabilmesine ve bunun sonucu olarak daha yüksek anot kapasitesi elde edilmesine imkân vermiştir. Elektro kaplama işlemi sonucunda elde edilen SnO_2/carbon kompozit nanoliflerin dış yüzeyi son olarak kimyasal buhar biriktirme (chemical vapor deposition, CVD) yöntemiyle nano boyutta amorf karbonla kaplanmış ve bu şekilde uzun anot ömrü oluşturulması hedeflenmiştir. Üretilen kompozit nanoliflerin herhangi bir bağlayıcı kimyasal ve akim toplayıcı kullanımına gerek olmadan direkt olarak lityum-iyon bataryalar için anot malzemesi olarak kullanılması üzerine deneysel çalışmalar yapılmıştır. Elektrokimyasal test sonuçlarına göre gözenekli yapıda karbon nanolif kullanıldığında daha yüksek anot kapasitesi elde edildiği gözlemlenmiştir. Bununla beraber gözenekli karbon nanoliflerin yüzeyine daha fazla SnO_2 nanoparçacık kaplandığı yapısal karakterizasyon çalışmalarıyla da ispatlanmıştır. Ayrıca elektrokimyasal testlerden elde edilen sonuçlara göre amorf karbonla kaplanmış olan SnO_2/karbon kompozit nanoliflerin amorf karbon kaplanmamış olana göre çok daha uzun anot ömrü gösterdiği saptanmıştır. Yapılan çalışma sonucu elde edilen amorf karbon kaplanmış SnO_2/gözenekli karbon kompozit nanolif anotların uygulanan 100 şarj-deşarj işlemi sonucunda ilk kapasitesinin yüzde 78'ini koruduğu ve kolombik verimliliğinin yüzde 99.8 olduğu gözlemlenmiştir.

Yüksek kapasiteli anot geliştirilmesi üzerine yapılan diğer bir çalışmada dış yüzeyi nano mertebede (10 nm) amorf karbonla kaplanmış olan silikon/silika/karbon (Si/SiO_2/karbon) kompozit nanoliflerden oluşan anot malzemesi geliştirilmesi üzerine araştırmalar yapılmıştır. Bu amaçla ilk olarak Si nanoparçacıklar, sol-jel tetra etil orto silikat (TEOS) solüsyonu ve polyvinil alkol (PVA)'den elde edilen çözeltiden elektro eğirme yöntemiyle Si/SiO_2/PVA kompozit nanolifleri üretilmiştir. Elde edilen nanolifler uygulanan karbonizasyon işlemi sonucunda Si/SiO_2/karbon kompozit nanoliflere dönüştürülmüştür. Karbonizasyon işlemi sonucunda elde edilen Si/SiO_2/karbon kompozit nanoliflerin herhangi bir bağlayıcı kimyasal ve akim toplayıcı kullanımına gerek olmadan direkt olarak lityum-iyon bataryalar için anot malzemesi olarak kullanılması üzerine batarya testleri yapılmıştır. Oluşturulan Si/SiO_2/karbon kompozit nanoliflerin yapısındaki silikon yüksek anot kapasitesi sağlaması için kullanılmıştır. Yapıdaki silika ise şarj-deşarj işlemleri esnasında silikonda meydana gelen hacimsel genişlemenin karbon yapısına zarar vermeden soğurulması amacıyla oluşturulmuştur. Ayrıca üretilen Si/SiO_2/karbon kompozit nanoliflerin dış yüzeyi daha sonra kimyasal buhar biriktirme (CVD) yöntemiyle nano boyutta amorf karbonla kaplanarak anot ömrünün uzatılması amaçlanmıştır. Üretilen anotlarla yapılan batarya testlerine göre yapısında silika bulunan kompozit nanoliflerin (Si/SiO_2/karbon kompozit nanolifler) Si/karbon kompozit nanoliflere göre çok daha yüksek anot ömrü ve batarya performansı verdiği tespit edilmiştir. Elektrokimyasal testlerden elde edilen sonuçlara göre ayrıca amorf karbonla kaplanmış olan

Si/SiO_2/karbon kompozit nanoliflerin amorf karbon kaplanmamış olana göre çok daha uzun anot ömrü gösterdiği gözlemlenmiştir. Yapılan çalışmada üretilen amorf karbon kaplanmış Si/SiO_2/karbon kompozit nanolif anotların uygulanan batarya testlerinde 50 şarj-deşarj işlemi sonucunda ilk kapasitesinin yüzde 91.0'ini koruduğu ve kolombik verimliliğinin yüzde 97.4 olduğu belirlenmiştir.

Katlanabilir ekranlar, vücuda implante edilebilir medikal cihazlar ve giyilebilir elektronik cihazlar gibi katlanabilir özellikteki elektronik cihaz teknolojilerinde son yıllarda ortaya çıkan yeniliklerle beraber bu cihazlarda enerji kaynağı olarak kullanılacak esnek lityum-iyon bataryaların ve dolayısıyla esnek elektrot malzemelerinin geliştirilmesi kritik derecede önem arz etmektedir. Yapılan diğer bir çalışmayla katlanabilir lityum-iyon bataryalar için yüksek kapasiteli, esneyebilir anot malzemesi geliştirilmesi üzerine araştırmalar yapılmıştır. Bu amaçla esneyebilir ve katlanabilir özellikte, yüksek kapasiteli silikon/silika/karbon (Si/SiO_2/karbon) kompozit nanoliflerden oluşan anot malzemeleri geliştirilmiştir. Esnek anot üretimi için ilk olarak Si nanoparçacıklar, sol-jel tetra etil orto silikat (TEOS) solüsyonu ve poliakrolinitril (PAN)'den oluşan çözeltiden elektro eğirme yöntemiyle Si/SiO_2/PAN kompozit nanolifleri üretilmiştir. Üretilen kompozit nanolifler uygulanan karbonizasyon işlemi sonucunda Si/SiO_2/karbon kompozit nanoliflere dönüştürülmüştür. Karbonizasyon işlemi sonucunda elde edilen Si/SiO_2/karbon kompozit nanoliflerin, yapısında silika bulunmayan Si/karbon kompozit nanoliflerin tersine oldukça esnek yapıda hatta katlanabilir özellikte olduğu gözlemlenmiştir. Üretilen Si/SiO_2/karbon kompozit nanoliflerin herhangi bir bağlayıcı kimyasal ve akim toplayıcı kullanımına gerek olmadan direkt olarak lityum-iyon bataryalar için esnek anot malzemesi olarak kullanılması üzerine batarya testleri yapılmıştır. Esnek Si/SiO_2/karbon kompozit nanoliflerin yapısındaki silikon üretilen anot malzemesinin yüksek lityum kapasitesi vermesi amacıyla kullanılmıştır. Yapıdaki silika ise üretilen anot malzemesine esneyebilme özelliği vermesi amacıyla oluşturulmuştur. Oluşturulan silika yapısı üretilen anot malzemesine esneyebilme özelliği vermesi yanında şarj-deşarj işlemleri esnasında silikonda meydana gelen hacimsel genişlemenin karbon yapısına zarar vermeden soğurulması işlevini de görmüştür. Üretilen esnek Si/SiO_2/karbon kompozit nanoliflerin dış yüzeyi daha sonra kimyasal buhar biriktirme (CVD) yöntemiyle nano boyutta amorf karbonla kaplanarak elde edilen esnek yapıdaki anotların ömrünün uzatılması amaçlanmıştır. Yapılan mekanik testlerle üretilen Si/SiO_2/karbon kompozit nanoliflerin yüksek derecede esneyebilir özellikte oldukları kanıtlanmıştır. Yapılan batarya testlerine göre esnek Si/SiO_2/karbon kompozit nanoliflerin kırılgan özellikteki Si/karbon kompozit nanoliflere göre daha yüksek anot ömrü ve batarya performansı verdiği tespit edilmiştir. Ayrıca, elektrokimyasal testlerden elde edilen sonuçlara göre amorf karbonla kaplanmış olan esnek Si/SiO_2/karbon kompozit nanoliflerin anot ömrünün amorf karbon kaplanmamış olana göre daha uzun olduğu tespit edilmiştir. Çalışma sonucu geliştirilen amorf karbon kaplanmış esnek Si/SiO_2/karbon kompozit nanolif anotların uygulanan batarya testlerinde 50 şarj-deşarj işlemi sonucunda ilk kapasitesinin yüzde 86.7'sini koruduğu ve kolombik verimliliğinin yüzde 96.7 olduğu gözlemlenmiştir.

Yapılan başka bir çalışmada dış yüzeyi nano mertebede, değişik kalınlıklarda (7, 10 ve 15 nm) silika (SiO_2) kaplanmış silikon/karbon (SiO_2-Si/karbon) kompozit nanoliflerden oluşan yüksek kapasiteli anot malzemesi geliştirilerek optimum anot performansını sağlayan SiO_2 kaplama kalınlığının tespit edilmesi üzerine deneysel çalışmalar gerçekleştirilmiştir. Çalışmada ilk olarak Si nanoparçacıklar, PAN ve dimetilformamit (DMF)'den elde edilen çözeltiden elektro eğirme yöntemiyle Si/PAN kompozit nanolifleri üretilmiştir. Elde edilen nanolifler uygulanan karbonizasyon işlemi sonucunda Si/karbon kompozit nanoliflere dönüştürülmüştür. Üretilen Si/karbon kompozit nanoliflerin dış yüzeyi daha sonra değişik kalınlıklarda SiO_2 kaplanarak SiO_2-Si/karbon kompozit nanolif anot malzemeleri elde edilmiş ve bu şekilde anot ömrünün uzatılması amaçlanmıştır. Elde edilen SiO_2-Si/karbon kompozit nanoliflerin lityum-iyon bataryalar için anot malzemesi olarak kullanılması üzerine batarya testleri yapılmıştır. Oluşturulan SiO_2-Si/karbon kompozit nanoliflerin yapısındaki silikon yüksek lityum kapasitesi sağlaması için kullanılmıştır. Üretilen anotlara uygulanan batarya testlerine göre nano boyutta SiO_2 kaplanmış bütün Si/karbon (SiO_2-Si/karbon) kompozit nanoliflerin SiO_2 kaplanmamış Si/karbon kompozit nanoliflere göre daha yüksek anot ömrü ve batarya performansı gösterdiği tespit edilmiştir. Elektrokimyasal testlerden elde edilen sonuçlara göre SiO_2-Si/karbon kompozit nanolifler için optimum anot performansı 7 nm'lik SiO_2 kaplamasıyla elde edilmiştir. Yapılan çalışmada üretilen 7 nm'lik SiO_2 kaplanmış SiO_2-Si/karbon kompozit nanolif anotların uygulanan 50 şarj-deşarj işlemi sonucunda ilk kapasitesinin yüzde 89.8'ini koruduğu ve kolombik verimliliğinin yüzde 97.2 olduğu gözlemlenmiştir.

Yapılan çalışmada sunulan özgün anot malzemelerinin yeni nesil lityum-iyon bataryalar için yüksek kapasiteli anot malzemelerinin geliştirilmesi için yapılacak yeni çalışmalarda araştırmacılar için yol gösterici nitelikte olacağı temenni edilmektedir.

1. INTRODUCTION

1.1 Overview of Electrochemical Energy Storage and Conversion Systems

Electrochemical energy storage and conversion technologies include batteries, fuel cells, and supercapacitors. Fuel cell is an electrochemical energy conversion device; on the other hand, batteries and supercapacitors are electrochemical energy storage devices. In such systems chemical energy is directly converted into electrical energy without any pollution, which makes them environmentally friendly [1]. In batteries and fuel cells, chemical energy is converted into electrical energy via the redox reactions at the anode and cathode. On the other hand, electrochemical capacitors are either based on the theory of charge storage in electrical double-layer with high-surface-area electrodes or redox reactions provide high pseudo capacitance at the interface of the electroactive species [2]. Ragone plot or diagram has been used to map the power and energy densities of electrochemical energy storage and conversion systems. Figure 1.1 shows a typical Ragone plot of the energy storage systems for the various electrochemical energy conversion domains compared with conventional capacitors and internal combustion engines and turbines. As can be seen in Ragone plot, fuel cells can be considered as high-energy systems, whereas supercapacitors are considered to be high-power systems. Compared to other systems, batteries show intermediate power and energy characteristics. From Figure 1.1 it can also be seen that, none of single electrochemical power source can show the energy and power density characteristics of combustion engine. It is very obvious that, competitive behavior in comparison to combustion engines (high power and high energy density) can be achieved if the available electrochemical power systems are combined [3]. Cost, performance, and reliability are the major factors that ensure the success of batteries in the market over the other two systems. Growth in lithium-ion battery market would result with the development of the sustainable energy sources and reduce the consumption of fossil fuels.

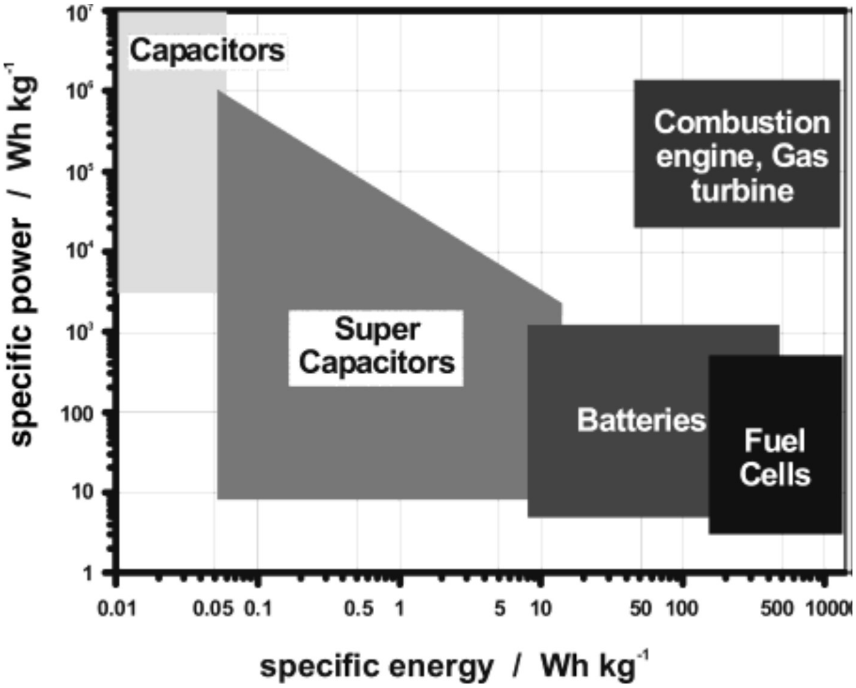

Figure 1.1 : Simplified Ragone plot of the energy storage domains for the various electrochemical energy conversion systems compared to an internal combustion engine and turbines and conventional capacitors [3].

1.2 Overview of Lithium-Ion Batteries

1.2.1 Introduction

Since lithium is the most electropositive and the lightest metal with a density of only 0.53 g cm^{-3} it is very suitable to design of storage systems with high energy density. The lithium-ion battery was first introduced in the 1970s by assembling of primary Li cells. Because of their high capacity and versatile discharge rate, they first used as power sources for calculators, watches, and implantable medical devices. Later on, rechargeable lithium-ion batteries drew great attention in both fundamental studies and practical applications [4]. As illustrated in Figure 1.2 lithium-ion batteries store comparatively more energy than nickel-metal hydride, nickel-cadmium, or lead acid batteries. Versatile properties such us high specific energy density, longer cycle life, low self-discharge rate, thermal stability, and no memory effect also make lithium-ion batteries superior to their competitors. Because of their superior properties, including high energy density, good cycle life and good power performance, lithium-ion batteries are considered as the most preferred rechargeable battery technology in recent years [5, 6].

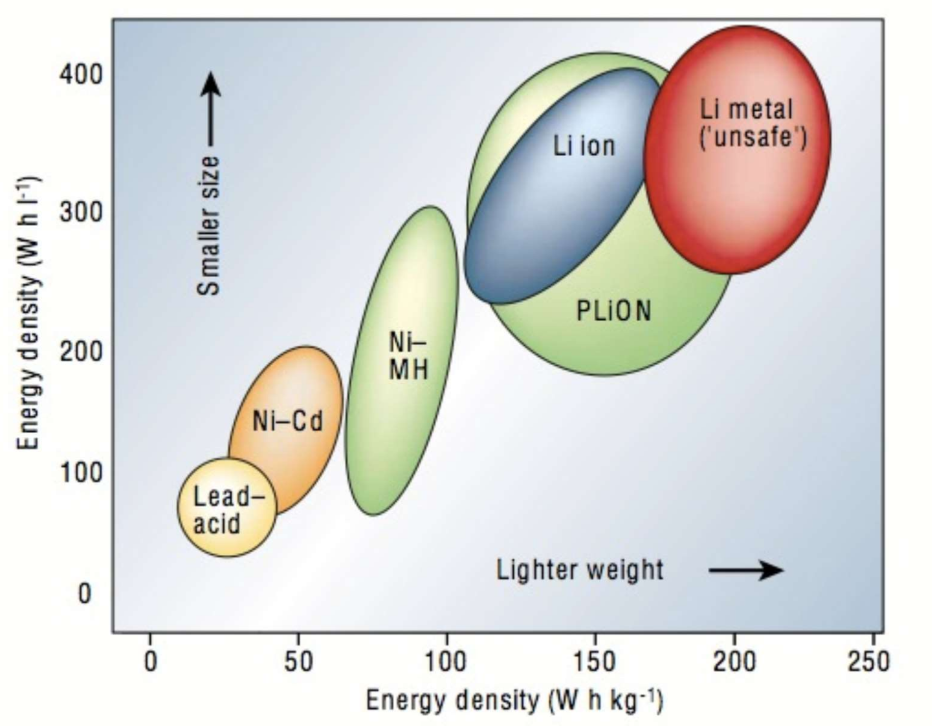

Figure 1.2 : Comparison of the different battery technologies in terms of volumetric and gravimetric energy density [4].

When lithium-ion batteries first introduced lithium metal was directly used as the negative electrode material. However, as anode, lithium metal revealed a safety issue caused by lithium dendrite, which led to short circuit and hazardous explosions. To prevent the safety problems and improve the cycle life metallic lithium was replaced by lithium insertion compounds [7].

The existing lithium-ion battery technology is based on the combination of a lithium metal oxide or phosphate cathode ($LiCoO_2$, $LiMn_2O_4$, and $LiFePO_4$) and a carbon anode [8]. Nowadays mostly graphite is used as the anode host while the layered $LiCoO_2$ is used as the cathode host in lithium-ion cells. As the electrolyte a lithium-containing salt solution such as $LiPF_6$ dissolved in an aprotic solvents like ethylene carbonate (EC) and diethyl carbonate (DEC) mixture is used [1]. Figure 1.3 shows the basic operating principle of a lithium-ion battery. During discharging and charging processes, lithium ions intercalate and deintercalate between the anode and cathode through the electrolyte. For instance in a $LiCoO_2$/graphite cell, during charging, lithium ions are produced from the layered $LiCoO_2$ cathode, pass across the electrolyte, and then intercalate into the graphite layers in the anode. Upon discharging, lithium ions leave the graphite layers, transferring through the electrolyte, and then intercalate back into the layered cathode [9].

Their chemical reactions are described as below:

Cathode: $LiCoO_2 \leftrightarrow Li1\text{-}xCoO_2 + xLi^+ + xe^-$ (1.1)

Anode: $6C + xLi^+ + xe^- \leftrightarrow Li_xC_6$ (1.2)

Generally, working potentials of cathodes are higher than 3.0 V versus Li^+/Li and working potentials of anodes are lower than 2.0 V versus Li^+/Li.

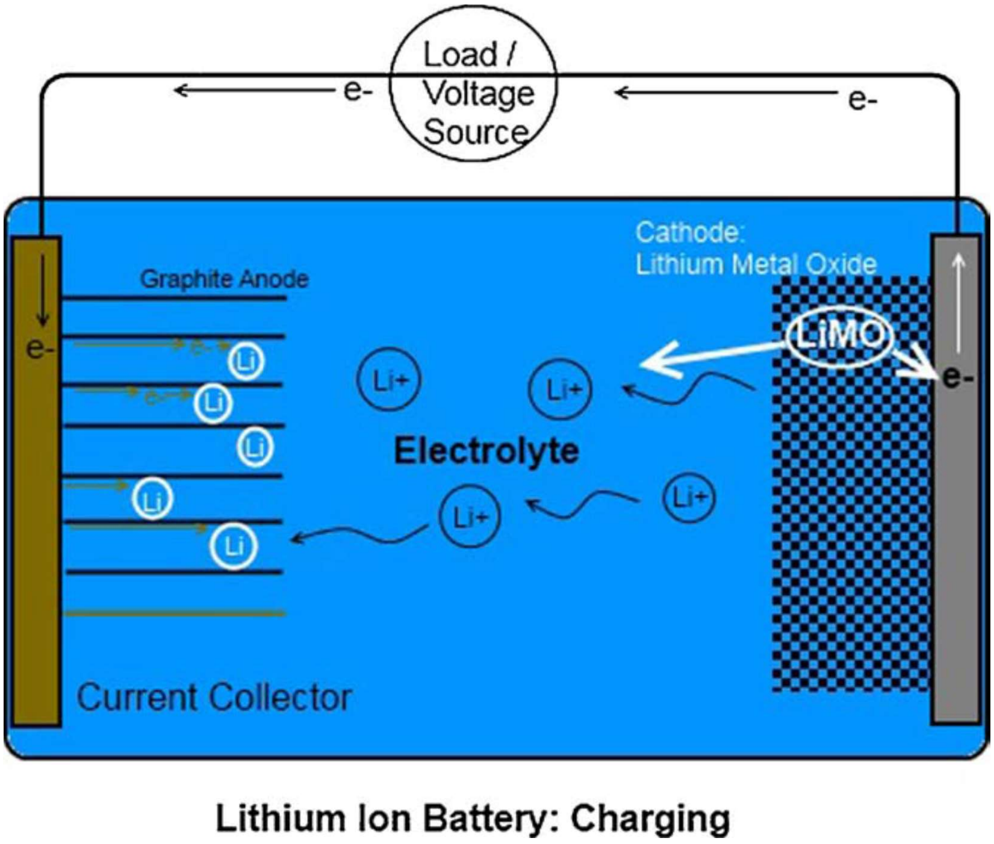

Figure 1.3 : Schematic of a lithium-ion battery [9].

An ideal rechargeable lithium-ion battery should have high specific energy and energy density that require the electrode materials to provide high specific capacity and large potential difference between the cathode and anode. The ability being highly reversible in specific charge capacity for hundreds of charge/discharge cycles is also a key factor for rechargeable lithium-ion batteries [7].

1.2.2 Cathodes

For almost two decades, $LiCoO_2$ has been considered as the dominant cathode material for lithium-ion batteries, which are produced for portable electronic devices such as laptops and cell phones. However, the high cost, poor thermal stability at elevated temperatures and high toxicity of $LiCoO_2$ make it unsuitable for using in larger-scale applications. Furthermore, lithium-ion batteries introduced for electric vehicles require higher energy density than the state-of-the-art lithium-ion battery to further reduce the weight and size of battery packs that power electric cars [10]. These requirements are the major driving force for the development of alternative layered structured cathode materials for lithium-ion batteries. Therefore, battery manufacturers have sifted their researches to find alternative materials to replace $LiCoO_2$, and examples of those alternative materials include layered lithium nickel oxide ($LiNiO_2$), lithium manganese spinels ($LiMn_2O_4$), vanadium oxides (LiV_3O_8), and olivines ($LiMPO_4$, M = Fe, Co, Mn or Ni) [11].

1.2.2.1 Layered lithium transition metal oxides

To date lithiated nickel and cobalt oxides, $LiMO_2$ (M= Ni, Co or Ni/Co) (Figure 1.4) are the most studied cathodes for lithium-ion batteries. Layer structured $LiCoO_2$ is the most widely used material for commercial production, because of its simple production method. Its average capacity is 140 mAh g^{-1} [11]. The price of cobalt has been increasing continuously, replacing cobalt with more abundant Ni/Mn is a cost effective and sustainable strategy to cover increasing demand of the market. $LiNiO_2$ has same crystal structure with $LiCoO_2$ and its working voltage is more than 3.7 V and theoretical capacity is 275 mAh g^{-1}. The $LiNiO_2$ provides important advantages, such as less toxicity, lower price and higher reversible capacity (200 mAh g^{-1}) as compared to $LiCoO_2$. However, it suffers from a few problems, such as irreversible phase transformation, difficulty in synthesis due to its tendency to form Ni-rich, non-stoichiometric phases, thermal instability and safety concerns [12].

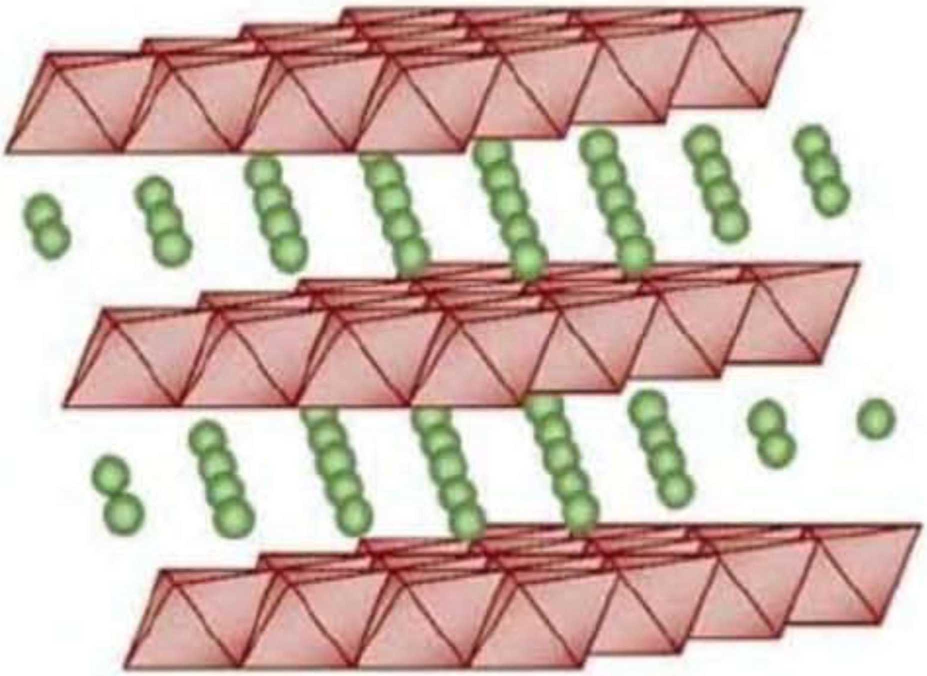

Figure 1.4 : Structure of layered lithiated transition metal oxides, $LiMO_2$ (M = Ni, Co, Mn) [13].

1.2.2.2 Lithium manganese oxides spinels

Lithium manganese oxide spinels, $LiMe_xMn_{2-x}O_4$ (Me = Metal element), are another type of cathode materials that are of extensive interest because of their low cost, environmental friendliness, good safety characteristics, and high power capability. Structure of the cubic spinel $LiMn_2O_4$ (lithium manganese oxide) is shown in Figure 1.5. They have been extensively studied as positive electrode materials of large-size lithium-ion batteries for power sources of hybrid electric vehicles [14, 15]. The main obstacle to commercialize $LiMn_2O_4$ is the significant capacity fading at elevated temperatures because lithium manganese oxides can be severely corroded in acidic electrolyte. A slight lithium ions deficiency causes the tetragonal phase formation provided that the materials obtained at high temperatures are rapidly quenched in the solid CO_2 [16, 17].

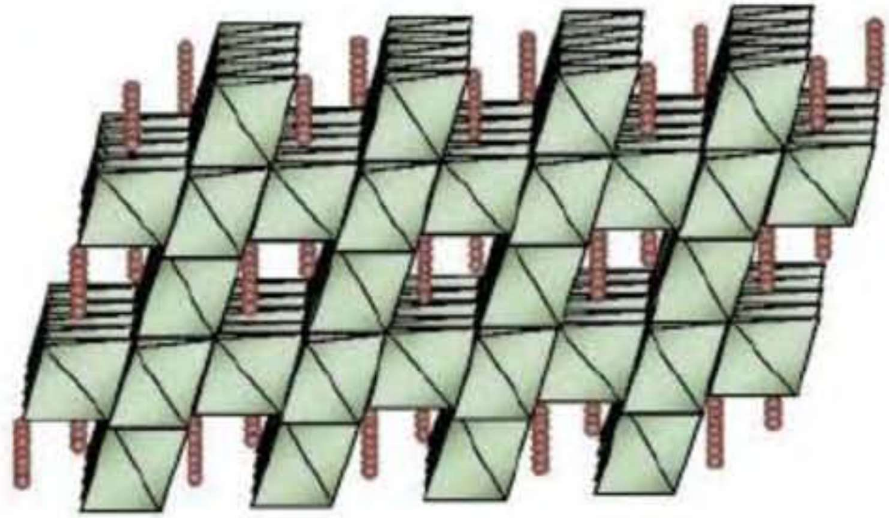

Figure 1.5 : Structure of the cubic spinel $LiMn_2O_4$ [13].

1.2.2.3 Lithium transition-metal phosphate

$LiFePO_4$ (Figure 1.6) was first introduced by Padhi et al. as a potential cathode material for lithium-ion batteries in 1997 and was regarded the safest cathode material for state-of-the-art lithium-ion batteries. It has a theoretical capacity of 170 mAh g^{-1} and is environmentally friendly and cheaper to produce compared with $LiCoO_2$. Furthermore, it shows good thermal stability and excellent cycle stability. These superior properties make it an attractive candidate for large scale battery applications, such as power sources for electric vehicles and hybrid electrical vehicles [11]. However, ionic diffusion and electronic conductivity are vital issues for $LiFePO_4$ cathode material and thus doping $LiFePO_4$ with supervalent cations that enhance the material conductivity at the crystal level or coating it with conductive materials such as carbons from organic precursors becomes critically important [18, 19]. Moreover, reducing the size of $LiFePO_4$ particles into the nanoscale range and dispersing them into carbon structure are proven to be efficient strategies because of the reduced distance for ionic and electronic transport [20, 21].

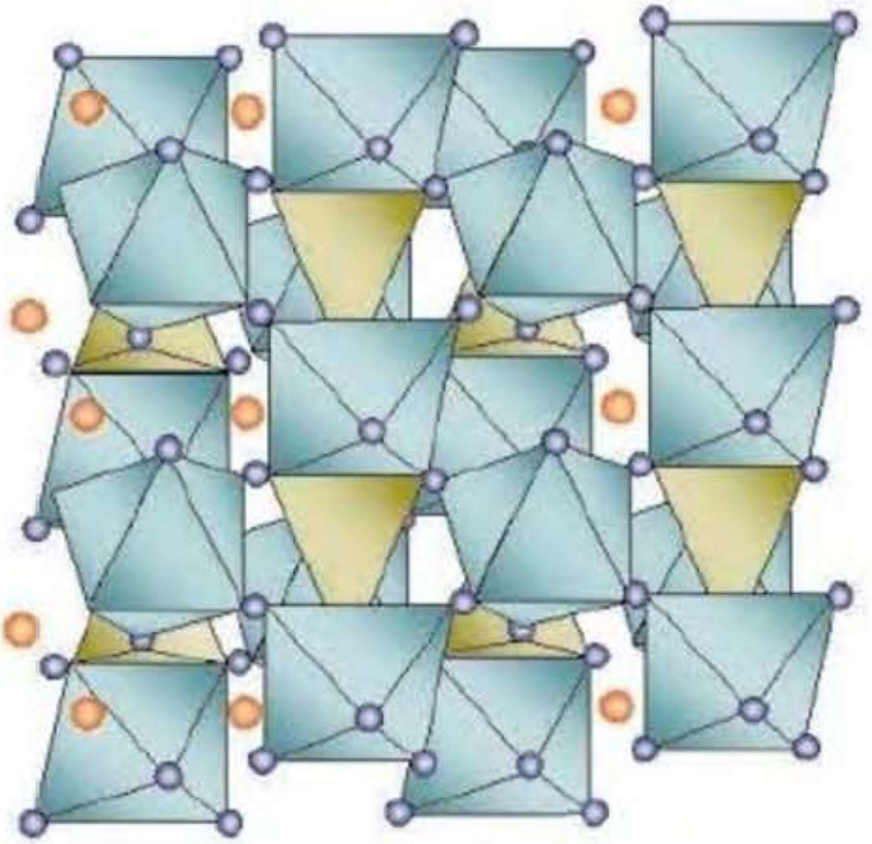

Figure 1.6 : Structure of olivine $LiFePO_4$ [13].

1.2.3 Anodes

Because of its high energy density, metallic lithium is considered as an excellent anode material and is used in primary lithium cells. However, its use in rechargeable Li-ion batteries may cause serious safety problems because the lithium dendrites can trigger an internal short circuit. Currently, most of the commercial lithium-ion batteries use graphite as the anode material. Furthermore, various other carbonaceous materials, lithium alloys and transition metal oxides are among the most promising alternatives for the anode and dominate current researches on the anode materials. Table 1-1 [22-26]lists the most commonly studied anode materials and their characteristics. Because of their advantages such as high charge-discharge capacities, favorable cycle stability, low cost and high safety compared to metallic lithium, they will continue the dominance in future rechargeable lithium-ion batteries. A summary of potentials and charge densities of candidate anode materials is shown in Figure 1.7. The emphasis is placed herein on three types of anode materials that can deliver high capacities and energy densities with low cost and good safety [27, 28].

Table 1.1: Comparisons between different anode materials.

Anode Material	Characteristics
Graphite	- High conductivity; theoretical capacity of 372 mAh g^{-1}; working potential is close to lithium anode. - Poor compatibility with electrolyte.
Disordered Carbon	- Includes soft (graphitizing) carbon and hard (non-graphitizing) carbon, both are amorphous; good compatibility with electrolyte; Soft carbon is the mostly used anode in power batteries.
Transition Metal Oxide	- High capacity; excellent rate performance. - High cost; poor cycling performance; high initial capacity loss.
Silicone Based Material	- High theoretical capacity of over 4000 mAh $^{-1}$. - Significant volume expansion; poor cycling performance.
Tin Based Material	- High specific capacity; safe. - Volume expansion; poor cycling performance.

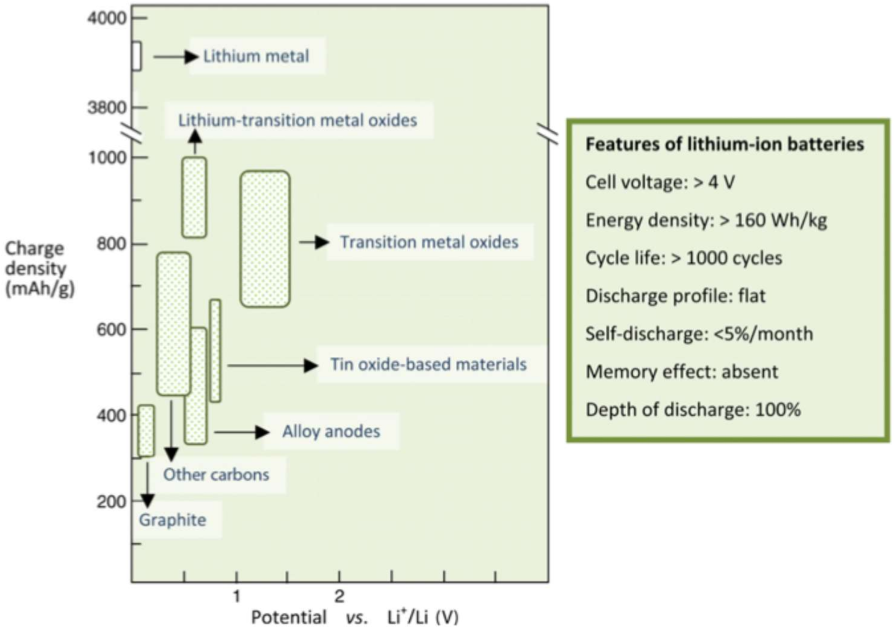

Features of lithium-ion batteries
Cell voltage: > 4 V
Energy density: > 160 Wh/kg
Cycle life: > 1000 cycles
Discharge profile: flat
Self-discharge: <5%/month
Memory effect: absent
Depth of discharge: 100%

Figure 1.7 : Potentials and charge densities of candidate anode materials. On the right are presented salient features of the lithium-ion battery technology [28].

1.2.3.1 Carbonaceous materials

Carbon is nontoxic, inexpensive and abundant. The carbon materials have indicated lower initial irreversible capacities, higher cycle-ability and faster mobility of Li in the solid phase. The carbon-based electrodes were developed to eliminate problems of lithium metal deposition, lithium dendrite formation. Carbon materials can generally be divided into graphite and disordered carbon. Disordered carbon materials have smaller cyrstallites, random rotations, turbostratic disorder and do not have the typical ABABABAB… stacking structure like graphite [29]. Disordered carbons basically can be either in the forms of non-graphitizing (hard) or graphitizing (soft) carbons. Figure 1.8 demonstrates the structures of graphitizing and non-graphitizing carbon [30]. Hard carbon materials have graphite-like layers that are not orientated like the crystalline structure of graphite and it is difficult to remove the turbostratic disorder at any temperature. On the other hand, soft carbon materials are those produced from materials generally containing more hydrogen and it is easy to remove the turbostratic disorder by heating around 2300 °C. Under same conditions, soft carbon materials are less porous and softer than hard carbon materials [29, 30].

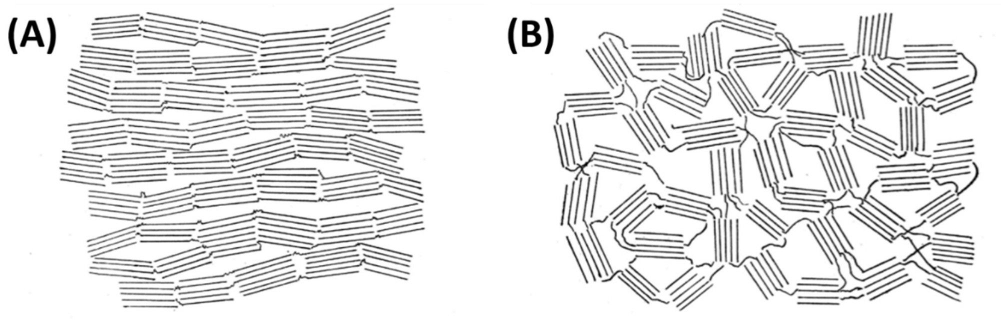

Figure 1.8 : Schematic representation of the structure of graphitizing (but non-graphitic) carbon (A) and non-graphitizing carbon (B) [30].

Commercial lithium-ion batteries have employed graphite as the anode material since the first manufacture of artificial graphite by E.G. Acheson at the end of the nineteenth century. Graphite is widely used in commercial lithium-ion batteries because of their low potential, high capacity retention, low cost and high safety [31]. Graphite is characterized as a stack of hexagonally bonded sheets of carbon held together by van der Waals forces and can insert only 1 lithium for every 6 carbon atoms (Figure 1.9). Lithium ions can be inserted between the planes of graphite based on the disparity of forces between two carbons in the same sheet or two adjacent sheets. Due to the repulsion of lithium ions, they can only combine on every second carbon hexagon in the graphite sheet thus limiting the amount of lithium ions to 1 for every 6 carbon atoms. This determines the theoretical capacity of graphite during charging and discharging, which is 372 mAh g^{-1} [9].

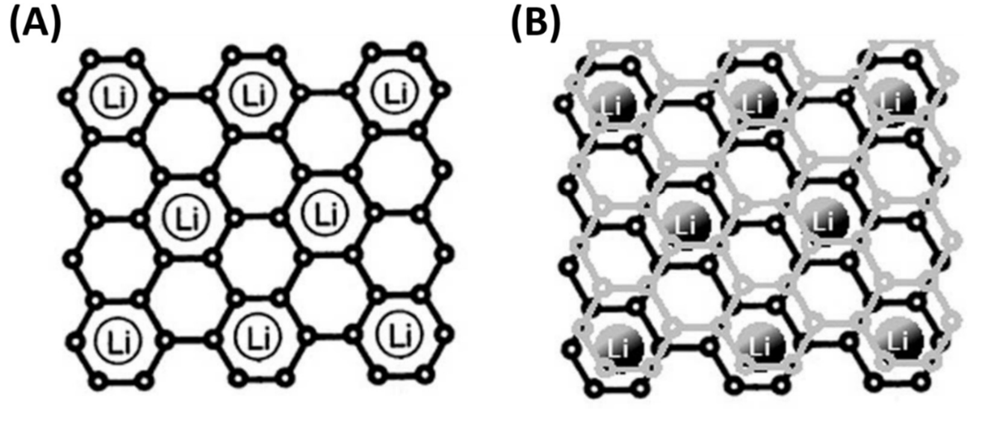

Figure 1.9 : Schematic of lithium intercalation in graphite. (A) Lithium is inserted in every 2nd carbon hexagon and (B) between the graphite layers [9].

The capacity of carbonaceous materials is determined by several factors like preparation method, crystal structure, particle size, surface area, surface species and types of electrolytes. Compared to graphitic materials, hard carbon materials have several advantages, such as higher capacity, longer cycle life, and low cost of production. Although hard carbons show larger reversible capacity they suffer from three major deficiencies: low density, large irreversible capacity and large hysteresis between charge and discharge [32]. Zheng et al. revealed that the large hysteresis occurs because of lithium accommodation at sites on hydrogen-terminated edges of hexagonal carbon fragments and alters the bond from sp^2 to sp^3. And the extent of hysteresis is proportional to the hydrogen content in the electrode structures [33].

Since disordered carbon materials possess different structure from graphite (smaller crystallite size and random crystallite orientation) lithium storage mechanism of disordered carbon is different from that of graphite. To explain why the disordered carbon could provide a high-energy density for rechargeable lithium-ion batteries, several models have been proposed and the mechanism is still controversial. Matsumura and his co-workers proposed three kinds of mechanism for disordered carbon. According to their results, when the disordered carbon is 30% fully charged, Li^+ mainly insert into the graphitic layers. Later on Li^+ would be doped on the surface of the crystallite. Finally, Li^+ would be doped at the edge of the graphitic layers. Due to these extra interaction mechanisms, disordered carbon could store more lithium than graphite so that have a higher energy density [34].

Apart from the above-discussed carbon materials, many other promising carbon materials are of great interest, below are some examples of novel and promising carbonaceous anode materials.

Recently, the high surface-to-volume ratio and perfect surface activities of 1D nanostructural carbon materials have drawn great interest in their development for the next generation high performance rechargeable lithium-ion battery anodes. Proposed concepts of using novel 1D nanostructural materials, such as tubes, wires, and fibers, have shown great promising [35].

After the discovery of carbon nanotubes (CNTs), researchers reported numerous studies about using CNTs as anodes for rechargeable lithium-ion batteries. CNTs can intercalate the Li ions between the pseudographitic layers and/or inside the central tubes. Generally, with the decrease of the number of graphite layers in CNTs, both electronegativity and maximum Li ion insertion increase. The lithium storage capacity of CNTs depends on the effective diffusion of Li ions into stable sites located on the surface and/or inside the individual nanotubes. The spaces between multi-wall carbon nanotube (MWCNT) layers or the interstitial sites of close-packed single-wall carbon nanotube (SWCNT) bundles can also storage Li ions, leading to relatively high Li_xC capacity [36, 37].

CNFs can also be used as the anodes for rechargeable lithium-ion batteries. Unlike CNTs, which require a long diffusion time for the Li-ion insertion and desertion, Li ions can diffuse more easily through the surface discontinuities in the walls of CNFs to result in increased Li storage capacity at normal charge and discharge rates. Because of the defects, including a large number of lattice defects, surface defects along their length, and open ends in CNFs, easy diffusion of Li ions are ensured [38, 39]. Wei et al. reported high rate capability CNF anode materials, which is produced by chemical vapor deposition (CVD) method. Because of the hybrid features of disordered and graphitic carbon, introduced CNFs anodes deliver a specific reversible capacity of about 461 mAh g^{-1} at 0.1 C. Even at a very high charge-discharge current rate of 10 C, these CNF anodes still can have a reversible capacity of about 170 mAh/g with a 95% coulombic efficiency (Figure 1.10) [39].

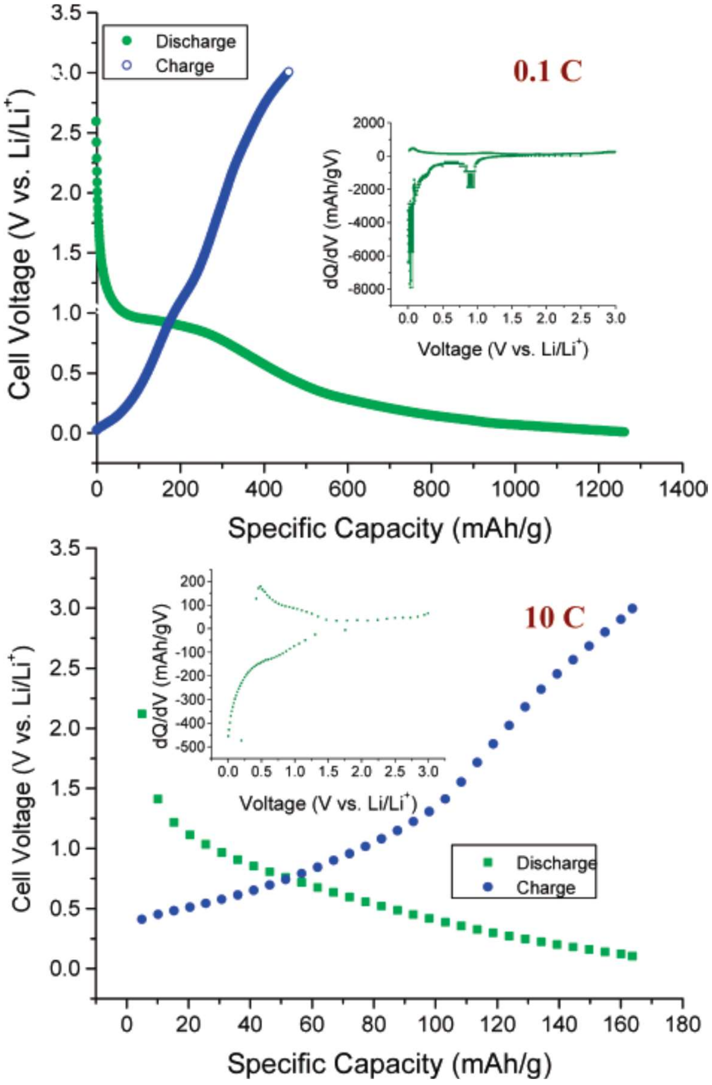

Figure 1.10 : Charge-discharge curves for CNFs anode at 0.1 and 10 C rates [39].

Porous carbon materials have attracted great attention as promising anode materials for lithium-ion batteries. Porous carbonaceous materials with different pore size, ranging from nanometer to micrometer scale have been electrochemically investigated. These porous carbon materials have been demonstrated to show a notably higher specific capacity than traditional graphitic carbons, although in many cases a relatively high irreversibility is also accompanied [40, 41]. For example, Ji et al. prepared porous carbon nanofibers (CNFs) anode materials via electrospinning of a blend of polyacrylonitrile (PAN) and poly-L-lactic acid (PLLA) solutions and subsequent heat treatment processes. During heat treatment process, the PLLA ingredient of the PAN/PLLA bicomponent nanofibers is degraded at elevated temperatures to obtain porous CNFs structure. For the introduced porous CNFs anodes, they reported a reversible specific capacity of 435 mAh g^{-1} at a current density of 50 mA g^{-1} over 50 cycles, which is higher than theoretical value of graphite (372 mAh g^{-1}) [41].

1.2.3.2 Tin-based anode materials

Among different potential candidates for anode materials, tin-based materials have been considered as one of the most promising alternatives because of their large theoretical capacity. However, large irreversible capacity and fast capacity fading caused by the huge volume expansion during cycling have hindered the practical application of tin-based anode materials in lithium-ion batteries. Similar to other alloy-type anode materials, insertion of lithium ions into the Sn structure during the charging causes high volumetric change (up to 300%), which results in intense pulverization and loss of electrical contact between the active material and carbon conductor. The crack of the electrode leads to the decrease of conductivity and increase of internal resistance of the cell, finally the failure of the cell [42, 43].

Tin

Sn delivers a relatively high theoretical capacity of 994 mAh g^{-1}, which is about 2.5 times of the capacity of graphite and have been given considerable attention for use as negative-electrode materials in lithium-ion batteries.[44, 45] However, like other Group IV element, one major problem is that the cyclability of the Sn electrode is poor due to large volume change and pulverization of the electrode during lithiation and delithiation processes [46]. Li-Sn binary-phase diagram suggests that tin forms seven different phases when reacted with lithium: $Li_{22}Sn_5$, Li_7Sn_2, $Li_{13}Sn_5$, Li_5Sn_2, Li_7Sn_3, LiSn and Li_2Sn_5. Figure 1.11 demonstrates the structure of different phases in the Li-Sn system [47]. The electrochemical reaction of tin with lithium metal can be described as the following:

$$\mathrm{Sn} + x\mathrm{Li}^+ + x\mathrm{e}^- \rightleftharpoons \mathrm{Li}_x\mathrm{Sn}\ (0 \leq x \leq 4.4) \qquad (1.3)$$

A reversible reaction of tin with excess lithium metal results in the formation of the binary intermetallic compound $Li_{4.4}Sn$ [48].

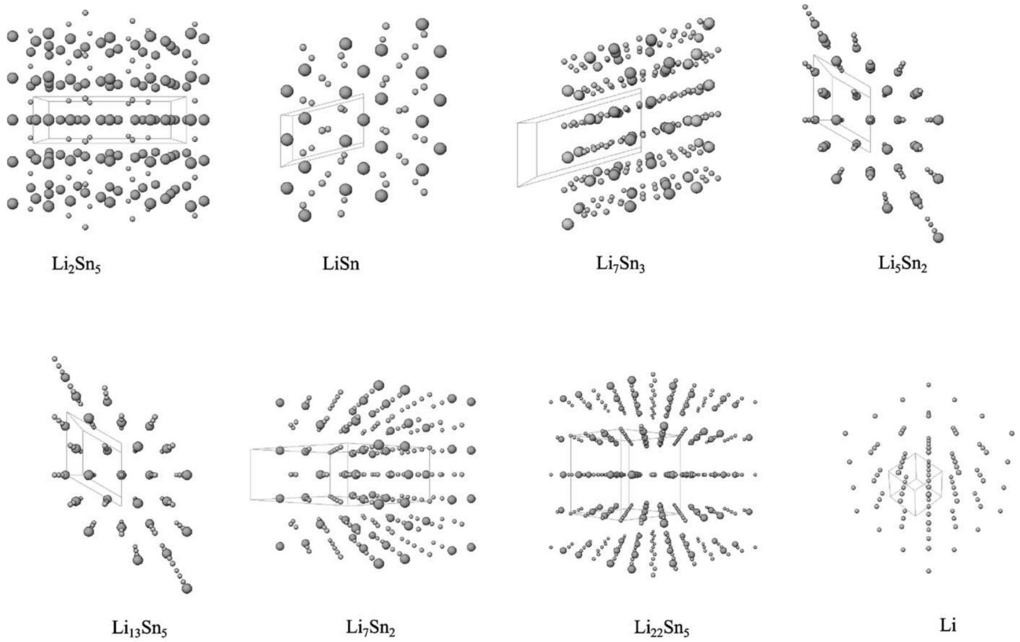

Figure 1.11 : Structures of different phases in the Li-Sn system [47].

Tin oxides

Tin oxides (SnO_x, x = 1 and 2) are considered as one of the most promising candidates for next-generation lithium-ion battery applications because of their high capacity, low cost, high abundance, and low toxicity.[49, 50] For SnO_2 based anodes, two principle electrochemical reactions occur during charge-discharge cycling:

$$SnO_2 + 4Li^+ + 4e^- \rightarrow Sn + 2Li_2O \qquad (1.4)$$

$$Sn + xLi^+ + xe^- \leftrightarrow Li_xSn \ (0 \leq x \leq 4.4) \qquad (1.3)$$

The first reaction leads to the reduction of SnO_2 to Sn and is irreversible. Formation of a solid electrolyte interface (SEI) at low voltage with this first reaction brings together apparent capacity decrease of the electrode during the initial cycles. In contrast, the second reaction is reversible. During insertion and extraction processes, lithium ions are repeatedly stored and released by the forming of alloyed Li_xSn and de-alloyed Sn, respectively [51, 52]. For the second reaction, the theoretical capacity is reported as 790 mAh g^{-1}, which is more than twice the theoretical capacity of graphite. However, similar to other alloy-type anode materials, insertion of lithium ions into the Sn structure during the second reaction causes high volumetric change (up to 300%), which results in intense pulverization and loss of electrical contact between the active material and carbon conductor [43, 53, 54]. Aforementioned drawbacks cause severe capacity fading of SnO_2 based anodes during lithium insertion and extraction processes. Preparation of porous structural SnO_2, reducing the size of SnO_2 particles into the nanoscale range and dispersing them into carbon structures are proven to be two effective methods for addressing the volumetric change problem of SnO_2 based anodes. If SnO_2 particles contain porous structures, the pores can play the role of a structure buffer for accommodation of large volume expansion upon cycling. Hence, porous SnO_2 shows no clear particle aggregation, high reversible capacity, and suppressed volume change. These electrochemical performance improvements can be attributed to the ability of mesoporous Sn to expand and contract with less structural degradation [55, 56]. Although using the nanoscaled SnO_2 can reduce the pulverization associated with the volumetric change, the cycling performance is still unsatisfactory because of the severe aggregation of nanoscale SnO_2 particles during the lithiation and de-lithiation processes [57, 58]. Dispersing SnO_2 nanoparticles in carbon structures leads to SnO_2/carbon nanocomposites with improved cycling performance [59]. In SnO_2/carbon nanocomposite anodes, the carbon matrix serves as a physical buffer to accommodate the volume change of the active material (i.e., cushion effect) during cycling [60, 61]. Nevertheless, carbon has limited lithium storage capacity, leading to reduced ultimate capacity for most SnO_2/carbon nanocomposite anodes [52, 54, 62].

Superior properties of the SnO_2/carbon composite nanostructures are related to these important factors: (1) small size of SnO_2 embedded within the nanospaces of porous carbon matrix hinders two-phase Li-Sn alloys formation, (2) interconnected carbon framework prevents particle aggregation, and (3) electronically conducting structure ensures good electrical conductivity of the electrodes [40]. Some of the reported novel SnO_2-carbon nanocomposite structures are carbon-SnO_2 nanocolloids, SnO_2-carbon composite hollow nanospheres, SnO_2 nanoparticles loaded carbon nanofibers, SnO_2-graphene nanocomposites, SnO_2 nanoparticles loaded carbon nanotube sheets, and porous SnO_2 nanotubes with coaxially grown carbon nanotube overlayers [43, 51, 54, 63-66].

1.2.3.3 Silicon

The development of high-capacity electrode materials for high-energy lithium-ion batteries is critically important for technological improvements on portable electronics and electric vehicle technologies that use lithium-ion batteries as the power source [67, 68]. Current commercial lithium-ion batteries use graphitic materials in the anode.

However, graphitic anode materials cannot meet the capacity requirements of future portable electronics because of their low specific capacity of 372 mAh g^{-1} [67, 69, 70]. Lithium storage capacity of alloy-type anodes, such as silicon (Si), tin, germanium, etc., is much higher than that of commercially-used intercalation-type graphite anodes. Among all alloy-type anodes, Si has the highest theoretical capacity of 4200 mAh g^{-1}, making it the best candidate for next-generation high-energy lithium-ion batteries [71, 72]. However, early studies on Si anodes demonstrated that the insertion of lithium ions into Si during cycling induces large volumetric change (up to 400%), which causes intense pulverization of active Si material, loss of electrical contact between Si and carbon conductor, and unstable SEI formation on the Si surface [73-75]. These drawbacks bring together the performance degradation of active Si material during repetitive lithiation and delithiation processes. An example of the charge/discharge curves of Si powder anode with an average size of 10 μm was demonstrated in Figure 1.12. Due to the large volume changes during the lithium insertion and extraction processes the capacity of the Si anode decreases. On the first lithiation Si provides high capacity, but capacity quickly fades during ongoing cycles. The reversible capacity of the Si anode decreases by 70% even after only five cycles [8].

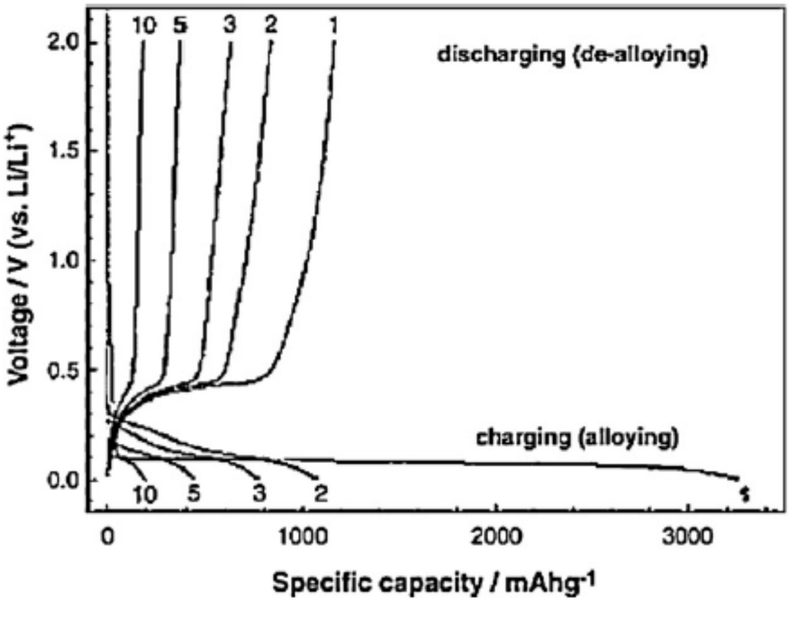

Figure 1.12 : Galvanostatic charge-discharge profiles for a micro-Si (10 μm particle) anode [8].

To eliminate the aforementioned drawbacks, novel Si-based composite anodes have been widely investigated. Among them, Si/carbon (Si/C) composites have drawn great attention, which combine the advantageous properties of Si (high capacity) and C (excellent electronic conductivity and structural stability). Maintaining the structural integrity of the electrode despite the 400% volume expansion of Si and stabilizing the SEI structure during cycling processes are, hence, the most crucial challenges for the development of Si/C based anodes [76, 77]. So far, there are several novel strategies for preserving the structural integrity of Si/C anode materials. One of them is to reduce the size of Si particles into nanoscale range to minimize the cracking and pulverization of these particles [78, 79]. Another strategy is to create open spaces between active Si particles and carbon matrix to accommodate the volume expansions of Si during cycling. For this purpose, SiO_2-coated Si nanoparticles are embedded in carbon matrix and subsequent HF acid treatment process is used to etch away the sacrificial SiO_2 layer to create a buffer zone between Si and carbon matrix [80, 81].

Liu et al. reported a novel yolk-shell structure for electrochemically stable Si anode (Figure 1.13) [82]. They successfully sealed commercially available Si nanoparticles inside nanoscale, self-supporting carbon shells, with rationally designed void space in between the Si particles and carbon shells. Void space between the carbon shell and the Si particles accommodate the expansion of Si without deforming the carbon shell or impairing the stable SEI formation on the electrode surface. Their structure showed high capacity (2833 mAh g^{-1} at C/10), long cycle life (1000 cycles with 74% capacity retention), and high coulombic efficiency (99.84%) (Figure 1.14).

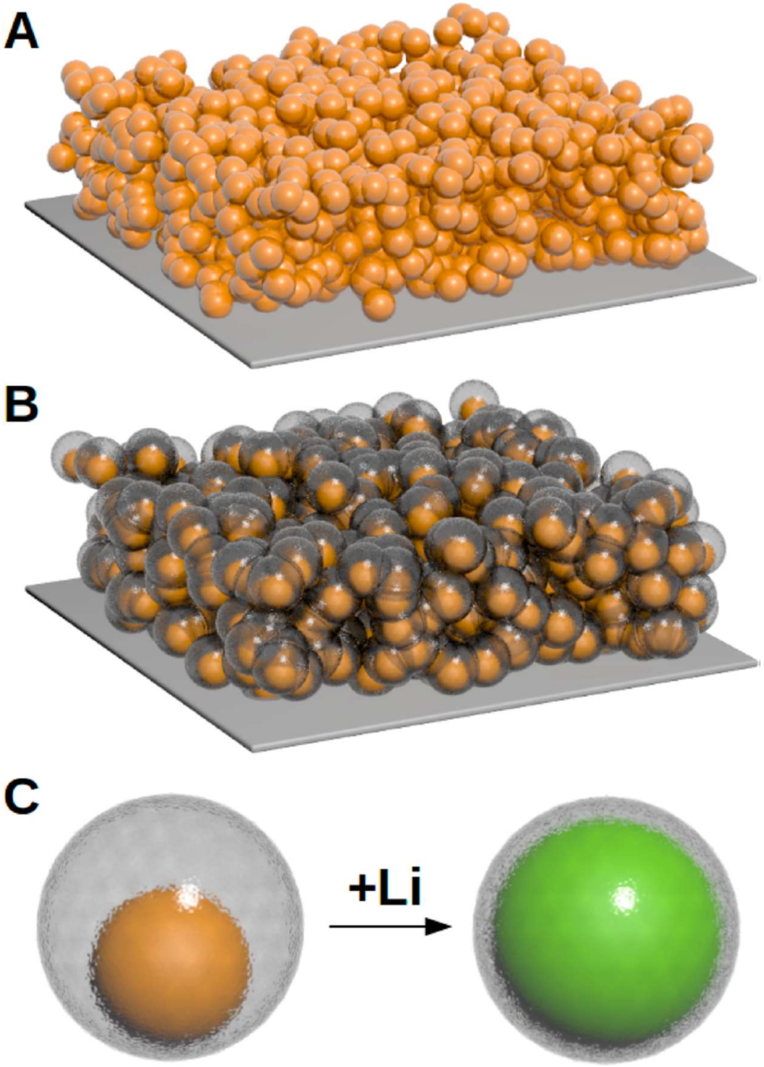

Figure 1.13 : Schematic of the materials design. (A) A conventional slurry coated SiNP electrode. (B) A novel Si@void@C electrode. The void space between each Si nanoparticles and the nanoscale carbon coating layer allows the Si to expand without rupturing the coating layer, which ensures that a stable and thin SEI layer forms on the outer surface of the carbon. Also, the volume change of the Si nanoparticles is accommodated in the void space and does not change the microstructure of the electrode. (C) A magnified schematic of an individual Si@void@C particle showing that the Si nanoparticle expands without breaking the carbon coating or disrupting the SEI layer on the outer surface [83].

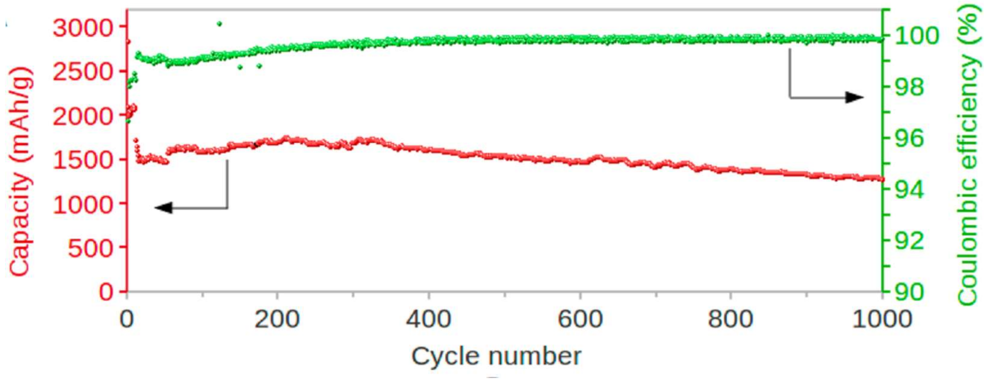

Figure 1.14 : Electrochemical cycling results for Si@void@C electrodes. Delithiation capacity and coulomb efficiency of the first 1000 galvanostatic cycles between 0.01−1 V. The rate was C/10 for one cycle, then C/3 for 10 cycles, and 1C for the later cycles [82].

Wu et al. designed a double-walled Si nanotube (DWSiNTs) by using electrospun carbon nanofiber as the template, followed by nanoscale silicon coating on the surface of carbon nanofibers [84]. Carbon nanofiber core was later removed via an oxidation process, while the SiO_x outside layer was formed on the Si nanotube's surface. The capacity retention of the double-walled Si nanotube anodes were more than 85% after 6000 cycles in a rate of 12C (Figure 1.15). This is because the outer SiO_x surface layer could prevent the inner Si nanotube from contacting the electrolyte, resulting in a good control of SEI formation.

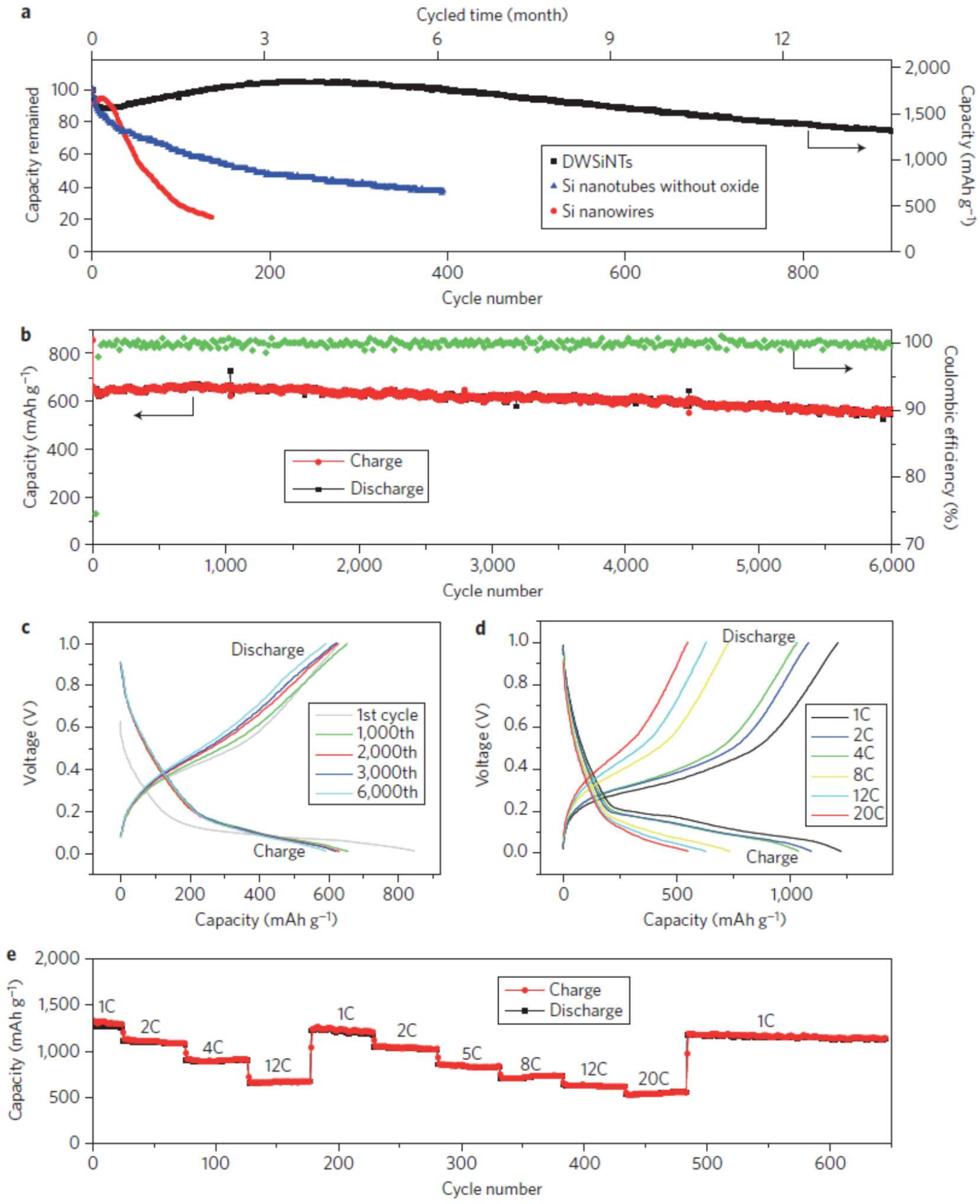

Figure 1.15 : Electrochemical characteristics of DWSiNTs tested between 1 V and 0.01 V. Capacity retention of different silicon nanostructures (a). All samples were cycled at the same charge/discharge rate of C/5. The calendar life and delithiation capacity of DWSiNTs can also be seen in this figure. Lithiation/delithiation capacity and coulombic efficiency of DWSiNTs cycled at 12C for 6,000 cycles (b). Voltage profiles plotted for the 1st, 1,000th, 2,000th, 3,000th and 6,000th cycles (c). Galvanostatic charge/discharge profiles (d) and capacity (e) of DWSiNTs cycled at various rates from 1C to 20C [84].

1.2.3.4 Cobalt oxide

Because of its high specific capacity (around 890 mAh g^{-1}), cobalt oxide is counted as a promising anode candidate for lithium-ion batteries. However, when used as an anode material, it shows a relatively large volume expansion and an unstable SEI formation during the cycling. The volume expansion leads to the pulverization of the active material and loss of electrical conductivity of the anode materials, which result with decreased reversible capacity [85]. The electrochemical conversion reaction of Co_3O_4 can be described as the follows:

$$Co_3O_4 + 8Li^+ + 8e^- \rightleftharpoons 4Li_2O + 3Co \tag{1.5}$$

The main drawback of Co_3O_4 is its poor electronic conductivity. To overcome the low electronic conductivity problem several strategies have been proposed. To date various morphologies of Co_3O_4 have been synthesized to obtain maximum anode performance such as nanotubes, nanowires, nanobelts, and hollow spheres [86-89].

Lou et al. reported needle-like Co_3O_4 nanotubes as lithium-ion battery anode, which was synthesized by a one-step self-supported topotactic transformation approach (Figure 1.16) [86]. The Co_3O_4 nanotubes anode shows excellent rate capability and ultrahigh capacity with nearly 100% capacity retention for over 30 cycles.

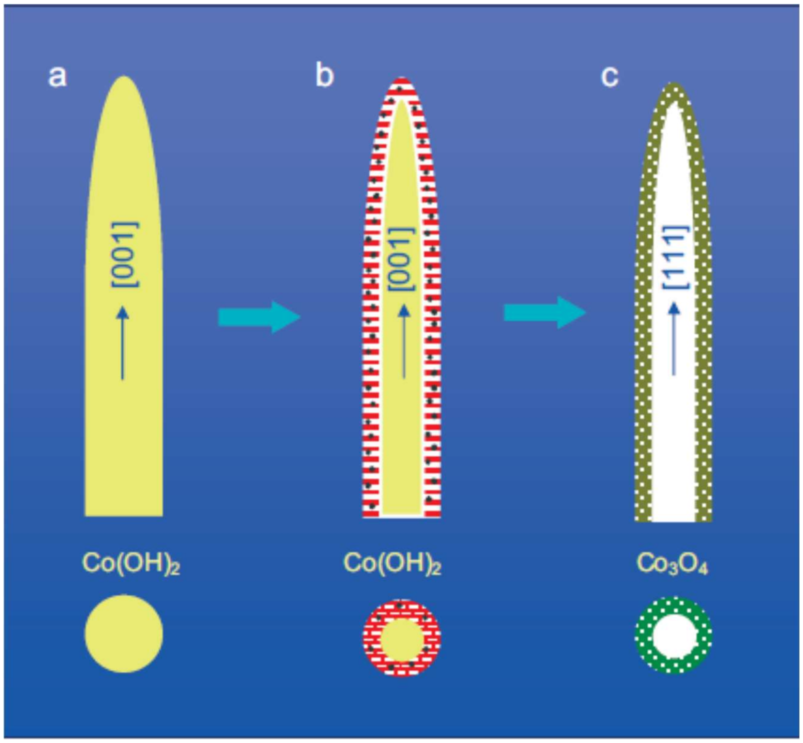

Figure 1.16 : Schematic illustration (cross sectional views along both directions perpendicular (top) and parallel (bottom) to the tube axis) of the self-supported topotactic transformation process for formation of needlelike Co_3O_4 nanotubes. a) Single-crystalline β-$Co(OH)_2$ nanoneedles grown along [001] direction. b) After surface reconstruction, loose platelet-walls form with possibly some Co_3O_4 nanoparticles (black dots) intercalated. c) Co_3O_4 nanotubes with compact wall, overall tube axis is [111] [86].

A template-free method for large-area growth of self-supported Co_3O_4 nanowire arrays, each nanowire is about 500nm in diameter and about 15 mm in length, has been reported by Li et al. [87]. Electrochemical tests reveals that the Co_3O_4 nanowire arrays anode show superior capacity retention compared to other non-self-supported nanowires and commercial Co_3O_4 powders. The charge capacity of the Co_3O_4 nanowire arrays is 700 mAh g^{-1} after 20 cycles, with a capacity retention of over 50 % even at a rate of 50 C. Unique hierarchical architecture leads to the high lithium storage capacity of the Co_3O_4 nanowire arrays.

Fu et al. introduced self-supporting Co_3O_4 with lemongrass-like morphology as anode for lithium-ion batteries (Figure 1.17) [90]. A reversible capacity of 981 mAh g^{-1} at a current density of 0.5 C was obtained over 100 cycles. At a higher current density of 10 C, a specific capacity of 381 mAh g^{-1} could still be observed. The relative good electrochemical performance might be attributed to the unique lemongrass-like morphology of the introduced Co_3O_4 material that can accommodate the volume changes during cycling.

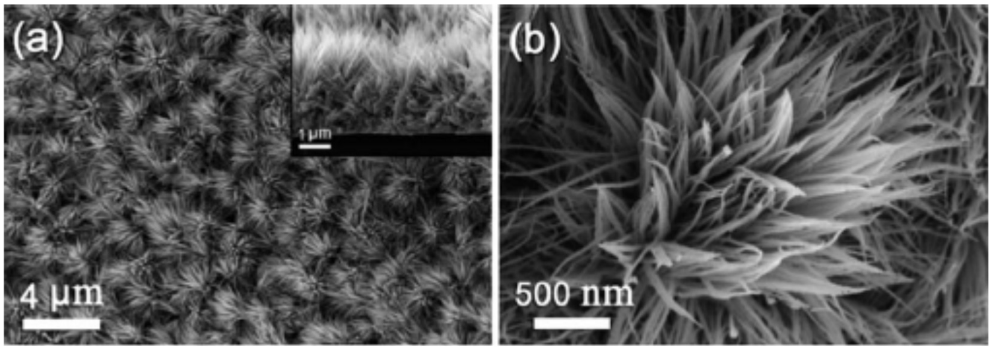

Figure 1.17 : Morphology and structure characterization of the self-supporting Co_3O_4. (a) Low-magnification SEM image, the inset is a side view. (b) High-magnification SEM image [90].

1.2.3.5 Manganese oxide

Manganese oxides with layered or tunneled structures are generally used as cathodes for lithium-ion batteries. Because of their natural abundance and environmental compatibility features manganese oxides are also considered as anode material in various energy storage systems. However, the practical application of manganese oxide-based anodes in rechargeable lithium-ion batteries is limited because of their improper electrical conductivity and large volume change upon repeated cycling processes. Wu et al. reported manganese oxide anodes consisting of interconnected nanowires, which is produced by electrochemical deposition technique [91, 92]. Introduced anode material shows a much larger lithium storage capacity than the traditional graphite materials. The electrode's reversible capacity reaches 1160 mAh g^{-1} at the first cycle and the specific capacity retention is 61% at the 50th cycle. A lithium-ion battery anode composed of MnO submicron particles with an average size of 200 nm through calcination of $MnCO_3$ is introduced by Aragón et al. [93]. Reported MnO particles are proved to be promising anode materials for recharge lithium-ion batteries. Yu et al. reported nanocrystalline MnO thin film materials, which is prepared by a pulsed laser deposition (PLD) method, as anode for lithium-ion batteries [94]. The reversible lithium storage capacity of the MnO thin film electrodes at 0.125 C is over 472 mAh g^{-1} and the capacity retention is more than 90% after 25 cycles. At a rate of 6 C, 55% of the capacity at 0.125 C rate can be obtained for both charge and discharge cycles. In addition, the introduced MnO thin film electrodes show the lowest values of overpotential for both charge and discharge among transition metal oxides. All these distinguished features make the MnO a promising high-capacity anode material for rechargeable lithium-ion batteries.

1.2.3.6 Titanium oxide

Nanostructured TiO_2, such as nanowires and nanotubes, has been considered promising anode material candidate for lithium-ion batteries. Armstrong et al. synthesized the TiO_2 nanowires and tested them as anode material in full lithium-ion batteries [95]. Electrochemical test results reveal that these lithium-ion batteries show the improved capacity compared to similar batteries assembled using $Li_4Ti_5O_{12}$ (225 mAh g^{-1} compared to 150 mAh g^{-1} at C/5). Zhou et al. reported the titania nanotubes with well-ordered mesoporous structures to be used as electrode materials in the rechargeable lithium battery. Such nanostructure provides pathways for both electrons and Li ions, which are essential for a high rate rechargeable lithium-ion batteries [96]. Recently, $Li_4Ti_5O_{12}$ (LTO) has attracted great attention as an anode material for lithium-ion batteries because of its excellent Li-ion insertion and extraction reversibility. Contrary to conventional carbonaceous materials, LTO can store up to three lithium ions with no volume change. Recently, Amine et al. synthesized a LTO structure which has micron-size secondary particles composed of nanometer-size primary particles (MSNP-LTO), as demonstrated in Figure 1.18. The rate capability of this LTO nanostructure was much better than that of the micronized LTO materials. The LTO nanostructure shows superior rate capability because the nano-primary particles could enable faster lithium diffusion via the shorter lithium pathway [97].

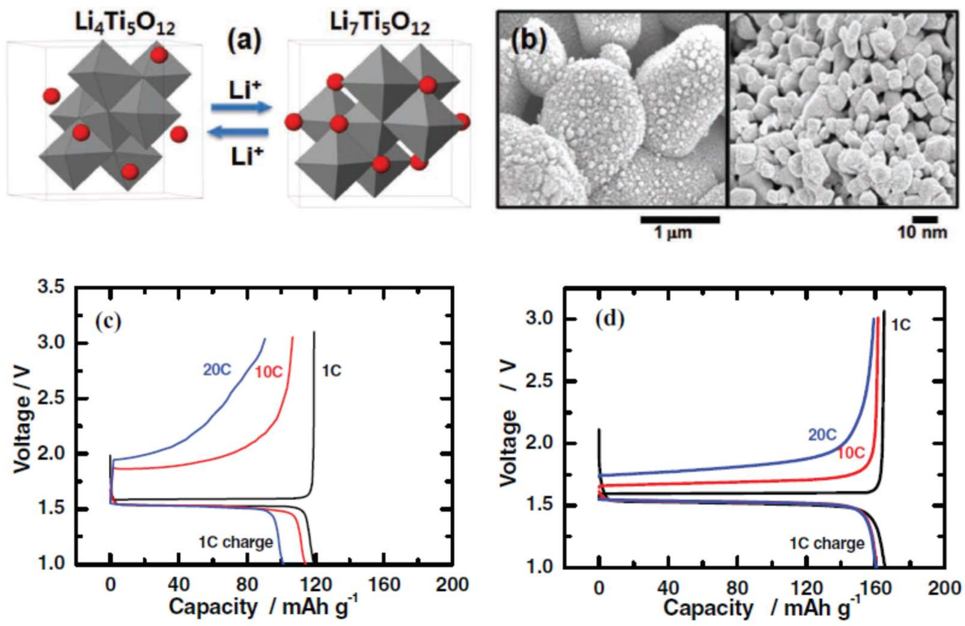

Figure 1.18 : a) Structure of $Li_4Ti_5O_{12}$ and $Li_7Ti_5O_{12}$, showing no volume change after charge and discharge. b) Scanning electron microscopy under low and high magnification of MSNP-LTO, showing secondary and primary particles. c,d) Charge and discharge curves of micron-size LTO and MSNP-LTO, respectively. The test was carried out in half cell. Initially, half cells were charged and discharged at 0.2-C rate, and then they were charged at 1-C rate and discharged at different rates [97].

Although it is very pleasing to obtain improved anode capacity, the total capacity of a battery would not be increased without a corresponding improvement in the cathode capacity. Therefore, the development of higher-capacity cathode materials is very crucial. Furthermore, though most of the novel anode materials highlighted herein show excellent electrochemical performance they would not be attractive for practical implementation if their mass production were not possible. Therefore, new designs of represented anode materials via cost-effective fabrication methods are necessary.

1.2.4 Electrolytes

The electrolyte system of lithium-ion batteries is generally a solution system containing mixed organic solvent and lithium salt. The majority of the electrolyte solution compose of non-proton polar solvents. Polar solvents used in electrolyte system possess high dielectric constants, do not react with lithium, and enable maximum solvation of lithium salt. For lithium-ion batteries, the most important characteristics of an electrolyte are the high Li^+ conductivity and rapid Li^+ motion within the electrolyte and across the electrode/electrolyte interface. Other expected characteristics of an electrolyte system are low toxicity, compatibility with electrode materials, low cost, and good stability [98]. Conventional organic liquid electrolytes show serious decomposition reactions at high temperatures under the circumstances of overcharging. Ionic liquids comprise large organic cations such as imidazolium, pyridinium, and pyrrolidinium and the corresponding coordinated inorganic anions. Because of their unique properties such as lower viscosity and high Li-salt solubility, modified imidazolium cation-based ionic liquids have been considered as competitive electrolytes for sustaining considerable battery performance [99]. Nowadays, solid electrolyte systems are considered as one of the most promising candidates, because they enable the fabrication of lighter and safer all-solid-state batteries with design flexibility in the shape and size. Polymer electrolytes, which can serve as both electrolytes and separators between the anode and cathode, consist of salts dissolved in polymers (for example, polyethylene oxide, PEO), and represent a unique class of solid coordination compounds. In recent years, great attention has been focused on poly(ethylene oxide) (PEO) and related polymers that are blended with Li salts such as $LiXF_6$ (X = P, As, Sb) [99, 100]. In addition to PEO-based polymer electrolytes, poly(vinylidene fluoride) (PVDF)-based polymer electrolytes are also counted as promising candidate with ionic conductivities up to 0.1 S m^{-1} at room temperature. They can act as membranes due to the intrinsically high electrochemical stability in a wide voltage range, good processability, and mechanical properties [101].

Wide use of fully solid polymer electrolytes is prevented by decay in ionic conductivity at temperatures below 70 ^{o}C. In addition to single liquid or solid electrolytes, the development of hybrid electrolyte systems is proposed as a new trend for future lithium-ion batteries. Combinations of two or more electrolytes system may gather advantages of the individual components. For instance, a gel-type membrane electrolyte that offers both high ionic conductivity, i.e., approaching that typical of liquid solutions and good mechanical stability, i.e., those typical of a polymer, can be formed by trapping a typical lithium-ion solution (e.g., $LiPF_6$ in carbonate solvent) in a polymer matrix (e.g., poly(vinylidene fluoride)) [102]. For introducing safe, high-rate, and high-energy cells PVDF-based gel electrolytes have been practically used as electrolyte with a Sn/C anode and a $LiNi_{0.5}Mn_{1.5}O_4$ cathode. Therefore, a suitable combination of novel anode, cathode, and electrolyte materials can lead to unprecedented achievements on rechargeable lithium-ion batteries [102].

1.3 Overview of Electrospinning Process

1.3.1 Introduction

Variety of fabricating methods have already been introduced for generating 1D nanostructures with a various forms, such as nanotubes, nanowires, nanobelts, and nanofibers [103]. Among various methods to prepare one-dimensional nanomaterials, electrospinning is considered as one of the most versatile and promising processes for producing continuous nanofibers for both laboratory-scale research and large-scale. Compared to other nanofiber production techniques, electrospinning enables to generate thin fibers with a relatively wide range fabrication purposes due to its feasibility in generating large quantities of nanofibers with well-defined surface morphologies at relatively low production time and cost [104-106]. Figure 1.19 demonstrates the comparison of the diameters of electrospun fibers and biological and technological objects [107].

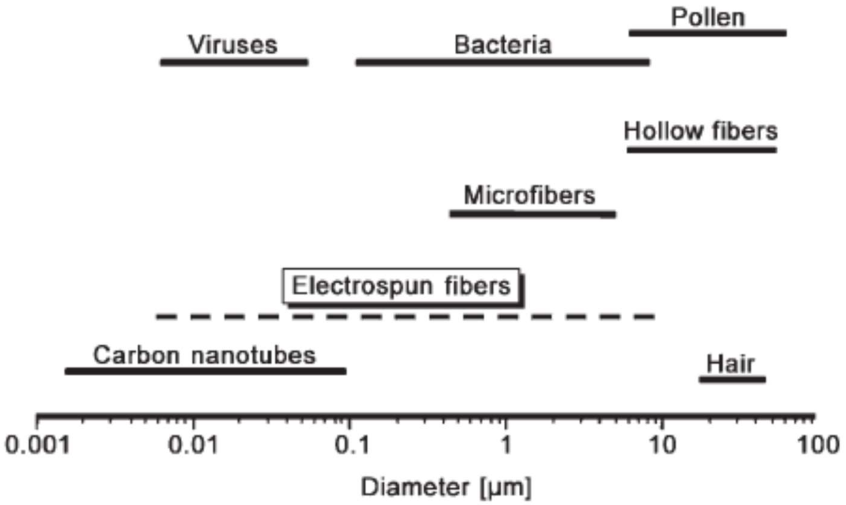

Figure 1.19 : Comparison of the diameters of electrospun fibers and biological and technological objects [107].

A schematic of a typical laboratory-scale electrospinning setup and photograph of an electrospinning jet captured by a high-speed video showing the bending instability of the jet is demonstrated in Figure 1.20A and B. An electrospinning setup mainly consists of a spinneret with a metallic needle, a syringe pump, a collector, and a high-voltage power supply. When the syringe is loaded with a viscous electrospinning solution, the solution is fed to the needle tip by the syringe pump, forming a droplet at the tip. One of the main differences between electrospinning and other mechanically driven spinning techniques is that the extrusion force is generated by the interaction between the charged polymer fluid and an external applied electric field. During the electrospinning process, the drop formed on the needle tip is subjected to two major types of electrostatic forces: the electrostatic repulsion between the surface charges and the coulombic force generated by the external electric field. Under the action of these electrostatic interactions, a conical fluid structure called Taylor cone is formed at the tip of the syringe. At a critical voltage, the repulsive force of the charged polymer overcomes the surface tension of the solution and a charged jet erupts from the tip of the Taylor cone. If the applied voltage is not high enough to form continuous spinning jet, the jet will break up into droplets. If the voltage is sufficiently high, a stable jet will form at the tip of the Taylor cone. The electrified jet is then exposed to a stretching and accelerating process, leading to the formation of a long and thin thread. As the liquid jet is continuously elongated, the solvent is rapidly evaporated and the dry fibers are collected on the surface of the collector forming a non-woven mat with the fiber diameters ranging from several micrometers down to tens of nanometers [107-111].

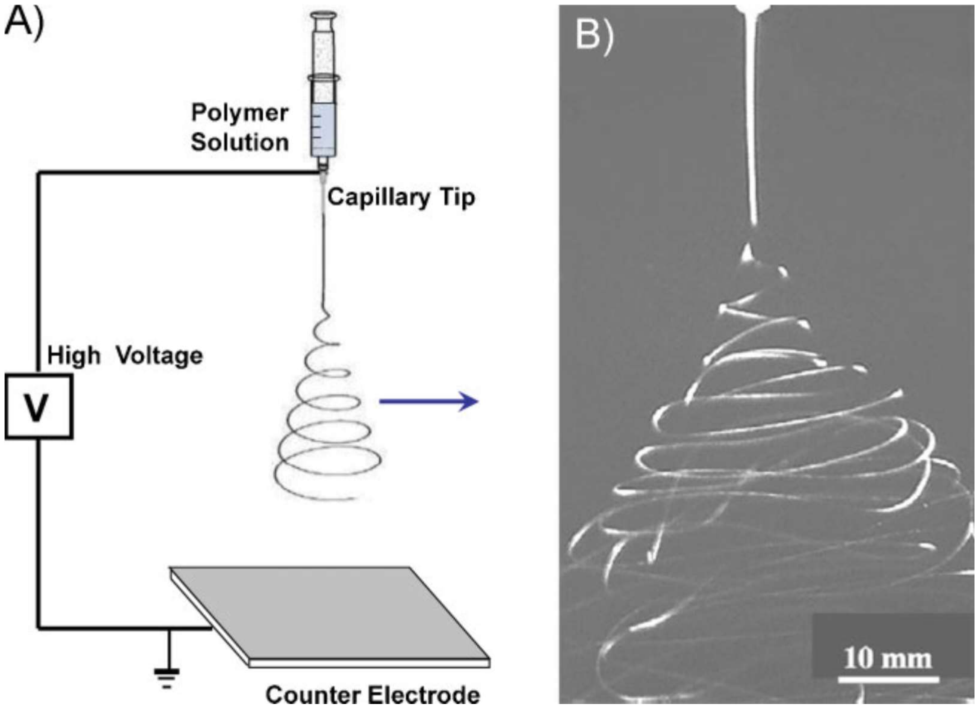

Figure 1.20 : A) Schematic diagram showing a laboratory setup for electrospinning. B) Photograph of an electrospinning jet captured by a high-speed video showing the bending instability of the jet [112].

A wide range of electrospun nanofibers made of natural polymers, polymer blends, ceramic precursors and metal or metal oxides have been investigated. By modifying the electrospinning equipment and methods, various fiber morphologies could be obtained, such as beaded structure, ribbon structure, porous fibers, and core-shell fibers (Figure 1.21). Statistics on electrospinning related publications show that about 40–60% of the researchers focus on applications such as tissue engineering, medical prostheses, drug delivery, and wound healing. In addition to biomedical applications, electrospinning method has also been used in other areas such as sensors, filters and separation membranes, templates for nanotube materials, protective layer, composite materials, and energy applications [113].

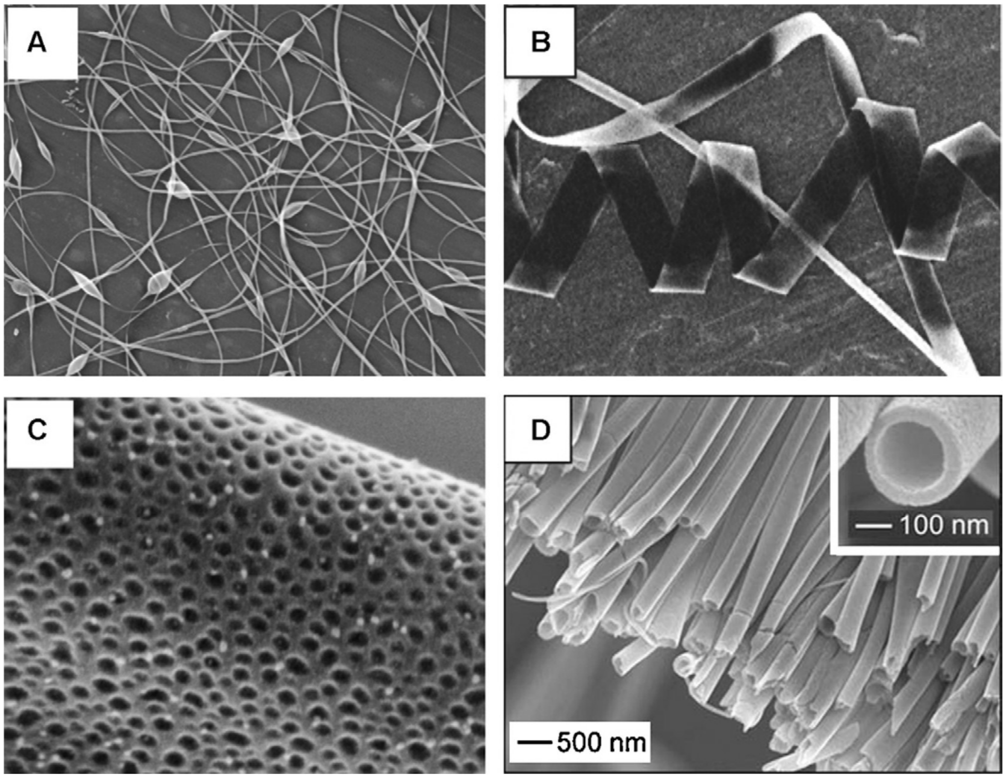

Figure 1.21 : Different electrospun fiber morphologies: (A) beaded, (B) ribbon, (C) porous fibers, and (D) core-shell [113].

1.3.2 Applications of electrospun nanofibers

Electrospun nanofibers have a series of distinctive properties, such as large specific surface areas and superior mechanical properties. Due to these unique properties, electrospun nanofibers have been applied in the field of reinforced composites, membranes, smart cloths, supports for enzymes and catalysts, electronic and optical devices, and energy storage and storage systems, such as rechargeable lithium-ion batteries, fuel cells, solar cells, and supercpacitors [104-106, 114, 115].

However, there are still many challenges with the mass-production of electrospun nanofibers and hence commercial use of electrospun fiber mats is still limited. In most of the eletrospun nanofiber related studies small-scale electrospinning devices are used for nanofiber production. Although the fabrication of nanofibers in mass-production scale is possible, more efforts are still needed to evaluate the characteristics and performance of the fibers produced by the large-scale equipment. In addition, it is a big challenge to produce uniformly distributed nanofibers with an average diameter below 100 nm, which is especially the case for melt electrospinning method due to its processing drawbacks. Also, other non-electrospinning technologies, such as the melt-blown and micro fiber production technologies used in the fiber industry, have the potential of fabricating submicron fibers. On the other hand, hybrid technologies are still under investigation for possible mass production of nanofibers [116, 117].

1.3.3 Polyacrylonitrile as a precursor to carbon fibers

Various polymers have been used as precursors for carbon fiber production, e.g., polyacrylonitrile (PAN), polyvinylchloride (PVC), polyimide (PI), polyamide (PA), polyethylene (PE), polystyrene (PS), polyvinyl alcohol (PVA), pitch, cellulose, viscose and so on [115, 118-121]. Among all of these carbon fiber precursors, PAN is considered as principle precursor in the production of commercial carbon fibers due to its high dielectric constant [122]. The molecular structure of PAN is demonstrated in Figure 1.22. PAN-based carbon fibers are fabricated by oxidative stabilization of PAN precursor fibers in an air atmosphere and subsequent carbonization process in inert gas.

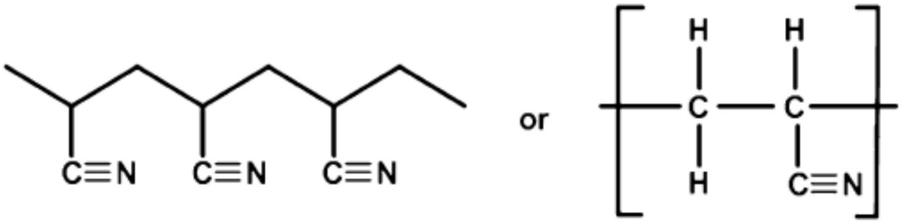

Figure 1.22 : Molecular structure of PAN [123].

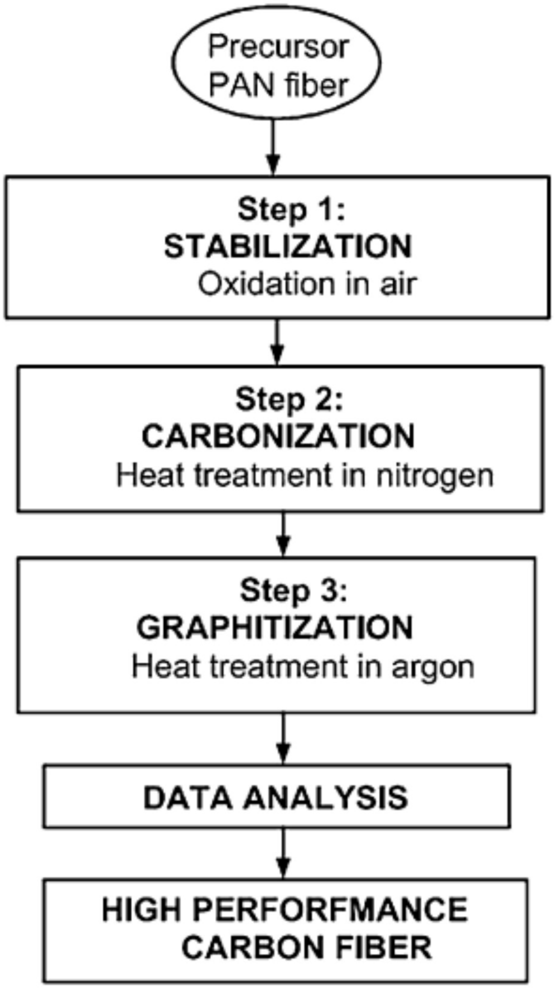

Figure 1.23 : PAN precursor carbon fiber conversion process [123].

The conversion from PAN fiber precursor to high performance carbon fiber is a long-time process and can be divided into three major steps; oxidative stabilization, high temperature carbonization, and graphitization (Figure 1.23) [123]. The first heat treatment (oxidative stabilization) is applied at 250-300 ºC in air environment. During oxidative stabilization process, PAN is involved in complicated chemical reaction processes, including cyclization, dehydrogenation, aromatization, oxidation and crosslinking (Figure 1.24) and conjugated ladder structure is formed [123, 124]. Oxidative stabilization process changes the chemical structure of the PAN fibers and makes them thermally stable and hence stabilized fibers do not melt during the following carbonization process. Recent studies also indicated that the stabilization process plays key role in converting PAN fibers to infusible stable ladder polymer, and to create crosslink between PAN molecules [123, 125, 126]. During the second thermal treatment step (carbonization) the stabilized fibers are subjected to heat treatment at enhanced temperatures (600-1300 °C) in an inert gas, such as nitrogen or argon. With the carbonization process, non-carbon atoms are removed from the structure in the forms of methane, hydrogen, hydrogen cyanide, water, carbon dioxide and ammonia, and a turbostatic structure is formed. The change of PAN structure during the carbonization is demonstrated in Figure 1.25. Compared to the precursor fibers, the carbonized fibers have higher density, reduced diameter, and are 40-50 % of their original weight [123, 125, 126]. After carbonization process, as produced carbon fibers can be directly used in different applications areas. On the other hand, for further improvement on the fiber performance, post graphitization process could be applied by heating up to 3000 °C to obtain high modulus graphitic structures [123].

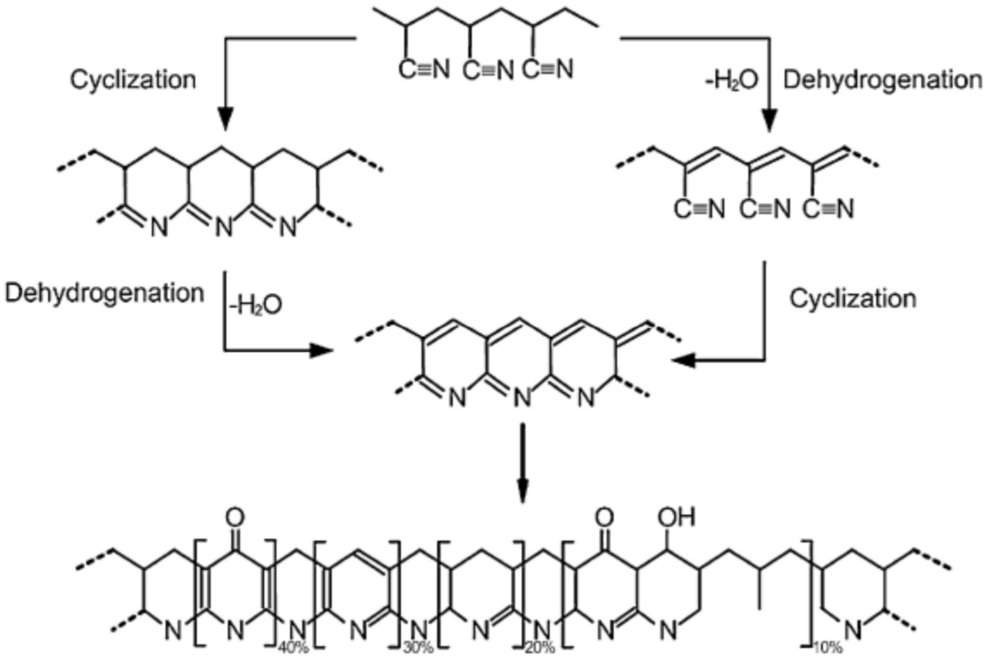

Figure 1.24 : Proposed chemistry of PAN stabilization [123].

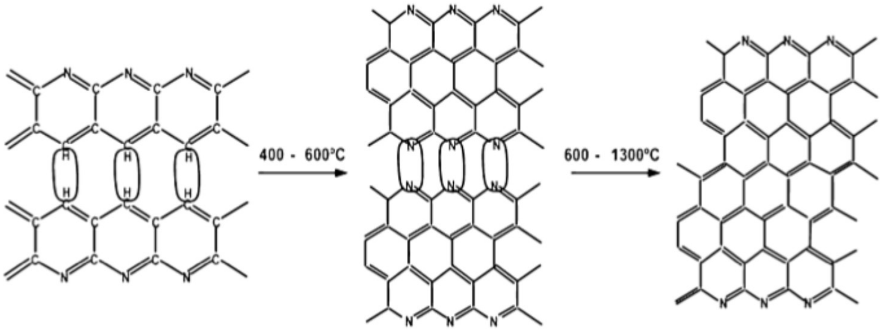

Figure 1.25 : Structure changes for PAN precursor during carbonization [124].

1.3.4 Polyvinyl alcohol as a precursor to carbon nanofiber composites

Polyvinyl alcohol (PVA) is a water-soluble thermoplastic polymer and has been investigated for using as a carbon precursor in fundamental researches, even though it is easily decomposed at elevated temperatures and provides low carbon yield [122]. PVA can be used for the fabrication of composite carbon nanofibers through thermal treatment processes [110]. Zhu et al. reported Fe_3O_4-filled PVA-based composite carbon nanofibers through carbonization at a relatively low carbonization temperature (600 ◦C). The resultant composite nanofibers revealed outstanding conductive and magnetic properties, which are maintained by the superhydrophobic surface feature of the composite nanofibers [127]. Fan et al. successfully synthesized Si/disordered carbon composite as anode for lithium-ion batteries through the electrospinning of Si nanoparticles-PVA solution followed by pyrolysis under argon environment. Field emission scanning electron microscopy (FESEM) images of as prepared Si/PVA nanofiber composite and Si/PVA-derived carbon composite is shown in Figure 1.26a and b [128].

In our study, composite carbon nanofibers (CNFs) prepared from electrospun PAN and PVA precursor nanofibers are used as anode materials in rechargeable lithium-ion batteries. The structural and morphological characteristics of PAN and PVA nanofibers based CNFs are beneficial to obtain improved electrochemical performance for rechargeable lithium-ion batteries.

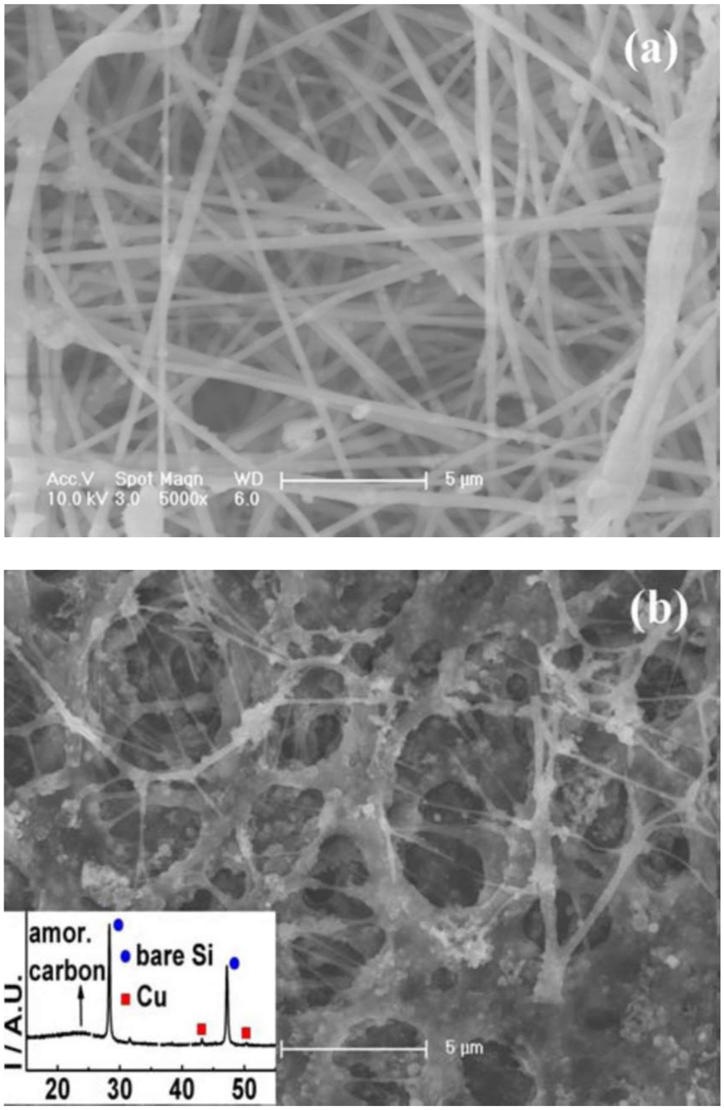

Figure 1.26 : FESEM images of (a) Si/PVA nanofiber composite and (b) Si/PVA-derived carbon composite (the inset shows XRD patterns of nano-Si/C composite) [128].

2. RESEARCH OBJECTIVES

The demand for high-performance lithium-ion batteries in terms of high power, high capacity and high rate capability is ever growing. To meet these requirements, it is very crucial to develop new anode materials to replace the currently used limited-capacity anodes, which is generally graphite. Lithium storage capacities of alloy-type anodes (e.g., silicon, tin, germanium, and their oxides) are much higher than that of currently-used intercalation-type graphite anode. Among different alloy-type anodes, Si and tin dioxide (SnO_2) are considered as the most promising candidates for next-generation lithium-ion batteries because of their high gravimetric and volumetric capacities. The main objective of this work is to fabricate novel composite nanofibers and discover their potential applications as anode materials for new-generation high-performance rechargeable lithium-ion batteries. For this purpose we have designed and fabricated novel SnO_2/C and Si/C composite nanofiber structures to combine the advantages of carbon (long cycle life) and lithium active (high storage capacity) materials and improve the electrochemical performance of the introduced composite nanofibers as anode materials for high-performance rechargeable lithium-ion batteries. The research work includes:

(I) Carbon-Enhanced Electrodeposited SnO_2/Carbon Nanofiber Composites as Anode for Lithium-Ion Batteries

Due to their high capacity, low cost, high abundance, and low toxicity tin oxides (SnO_2) are considered as promising anode material candidate for next-generation lithium-ion batteries. However, severe volume changes of SnO_2 anodes during the cycling lead to intense pulverization and loss of electrical contact between the active material and carbon conductor. In this proposed work, we introduced binder-free SnO_2-electrodeposited carbon nanofibers (CNF@SnO_2) and SnO_2-electrodeposited porous carbon nanofibers (PCNF@SnO_2) composites that can maintain their structural stability during repeated charge-discharge cycling. Both CNF@SnO_2 and PCNF@SnO_2 composites were also coated with amorphous carbon layers by chemical vapor deposition (CVD) method to further improve the structural stability and electrochemical performance.

The results of this work are discussed in Chapter 3.

(II) Carbon-Confined PVA-Derived Silicon/Silica/Carbon Nanofiber Composites as Anode for Lithium-Ion Batteries

Recently, Si/carbon (Si/C) composite anodes have drawn great attention, which can potentially combine the advantageous properties of Si (high capacity) and C (excellent electronic conductivity and structural stability). However, maintaining the structural integrity of the electrode despite the 400% volume expansion of Si and stabilizing the SEI structure during cycling processes are the most crucial challenges for the development of Si/C based anodes. In this work, new electrode design has been proposed to overcome the aforementioned problems of Si/C based anodes. For this purpose, two different Si/C based anodes were synthesized: $Si/SiO_2/C$ nanofiber composite and chemical vapor deposition (CVD) carbon-coated $Si/SiO_2/C$ nanofiber composite. Si/SiO_2/polyvinyl alcohol (PVA) nanofiber composites were first produced by electrospinning of a mixture of silicon nanoparticles, sol-gel tetraethyl orthosilicate (TEOS) solution, and aqueous PVA solution. After electrospinning, the resultant Si/SiO_2/PVA nanofiber composites were carbonized to obtain $Si/SiO_2/C$ nanofibers, which formed free-standing conductive nonwoven mats and were used directly as binder-free anodes for lithium-ion batteries. $Si/SiO_2/C$ nanofibers were also coated with nanoscale amorphous carbon layer by CVD technique to ensure maintaining of the Si nanoparticles within the carbon nanofiber matrix during repetitive charging and discharging processes.

The results of this work are discussed in Chapter 4.

(III) Flexible Binder-Free Silicon/Silica/Carbon Nanofiber Composites as Anode for Lithium-Ion Batteries

Development of high-capacity flexible electrode materials for high-energy lithium-ion batteries become critically important with technological improvements on portable and bendable electronic equipment such as rollup displays, implantable medical devices, active radio-frequency identification tags, and wearable devices. Although various types of bendable electrode materials have been reported, it is very important to fabricate highly flexible electrode materials with reasonable fabrication technique and high electrochemical performance similar to those of conventional high-capacity electrode materials. In this proposed work, we fabricated high-capacity, flexible Si/SiO_2/C nanofiber composite anode materials by simple electrospinning and subsequent heat treatment processes. To further improve the long-term cycling performance, additional nanoscale carbon coating of flexible Si/SiO_2/C nanofibers was performed by CVD technique.

The results of this work are discussed in Chapter 5.

(IV) SiO_2-Confined Silicon/Carbon Nanofiber Composites as Anode for Lithium-Ion Batteries

Because of its ultra-high theoretical capacity (4200 mAh g^{-1}), Si is considered as the most promising anode material candidate for next-generation high-energy lithium-ion batteries. However, the practical use of Si based anodes is constrained by the high volume change (up to 400%) of Si active material during cycling. Intensive volume change of Si causes severe pulverization, loss of electrical contact between Si particles and carbon current collector, and unstable SEI formation on the electrode surface. In this proposed work, we introduce nanoscale silica-coated silicon/carbon (Si@C-SiO_2) nanofiber composites that can maintain their structural stability during repeated cycling. We proposed a feasible method to improve the electrochemical performance of previously reported Si@C nanofiber composite electrodes. The main target of this study is to propose a simple, but effective approach for the confinement of Si nanoparticles inside the Si@C nanofiber composite electrodes. Si@C nanofibers were produced by simple electrospinning and subsequent heat treatment processes. The resultant Si@C nanofibers were coated with nanoscale amorphous SiO_2 layers by using sol-gel TEOS solution to achieve further improvement on the cycling performance of the composite anodes.

The results of this work are discussed in Chapter 6.

3. CARBON-ENHANCED ELECTRODEPOSITED SnO_2/CARBON NANOFIBER COMPOSITES AS ANODE FOR LITHIUM-ION BATTERIES

3.1 Introduction

Among the various existing rechargeable battery technologies, rechargeable lithium-ion batteries are considered as the most preferred rechargeable batteries in recent years because of their superior properties such as high energy density, long cycle life and good power performance [72, 129]. Development of high-capacity electrode materials for lithium-ion batteries is crucial for technological improvements on grid storage, mobile electronic devices and electric vehicle technologies using lithium-ion batteries as the power source [75, 130-132]. Current commercial lithium-ion batteries use graphitic materials in the anode. However, the theoretical capacity (372 mAh g^{-1}) of graphitic anode materials cannot meet the ever-growing capacity requirements of future portable electronics and electric vehicle technologies [67, 69].

Lithium storage capacities of alloy-type anodes (e.g., silicon, tin, germanium, and their oxides) are featured by ultrahigh theoretical capacity comparing to currently-used intercalation-type graphite anode. Among all alloy-type anodes, tin oxides (SnO_x, x = 1 and 2) are considered as one of the most promising candidates for next-generation lithium-ion batteries because of their high capacity, low cost, high abundance, and low toxicity [49, 50]. For SnO_2 based anodes, two principle electrochemical reactions occur during charge-discharge cycling:

$$SnO_2 + 4Li^+ + 4e^- \rightarrow Sn + 2Li_2O \qquad (3.1)$$

$$Sn + xLi^+ + xe^- \leftrightarrow Li_xSn\ (0 \leq x \leq 4.4) \qquad (3.2)$$

The first reaction leads to the reduction of SnO_2 to Sn and is irreversible.

This chapter consists of the article below:

Dirican, M., Yanilmaz, M., Fu, K., Lu, Y., Kizil, H., and Zhang, X. (2014). Carbon-enhanced electrodeposited SnO_2/carbon nanofiber composites as anode for lithium-ion batteries, *Journal of Power Sources, 264*, 240-247.

Formation of a solid electrolyte interface (SEI) at low voltage with this first reaction brings together apparent capacity decrease of the electrode during the initial cycles. In contrast, the second reaction is reversible. During insertion and extraction processes, lithium ions are repeatedly stored and released by the formation of alloyed Li_xSn and de-alloyed Sn, respectively [51, 52]. For the second reaction, the theoretical capacity is reported as 790 mAh g^{-1}, which is more than twice the theoretical capacity of graphite. However, similar to other alloy-type anode materials, insertion of lithium ions into the Sn structure during the second reaction causes high volumetric change (up to 300%), which results in intense pulverization and loss of electrical contact between the active material and carbon conductor [43, 53, 54]. Aforementioned drawbacks cause severe capacity fading of SnO_2 based anodes during lithium insertion and extraction processes. Reducing the size of SnO_2 particles into the nanoscale range and dispersing them into carbon structures are proven to be two effective methods for addressing the volumetric change problem of SnO_2 based anodes. Although using the nanoscaled SnO_2 can reduce the pulverization associated with the volumetric change, the cycling performance is still unsatisfactory because of the severe aggregation of nanoscale SnO_2 particles during the lithidation and de-lithidation processes [57, 58]. Dispersing SnO_2 nanoparticles into carbon structures leads to improved cycling performance [59]. Various carbon nanostructures, such as graphene, mesoporous carbon materials, graphite, carbon nanotubes, and carbon nanofibers etc., have been extensively introduced as host materials for SnO_2/carbon composite anodes [130, 133-135]. In SnO_2/carbon nanocomposite anodes, the carbon matrix serves as a physical buffer to accommodate the volume change of the active material (i.e., cushion effect) during cycling [60, 61]. Nevertheless, carbon has limited lithium storage capacity, leading to reduced ultimate capacity for most SnO_2/carbon nanocomposite anodes [52, 54, 62].

Recently, SnO_2 nanoparticle-loaded electrospun carbon nanofiber (CNF) composites have been introduced as high-capacity anode materials for lithium-ion batteries. Integration of the SnO_2 nanoparticles with CNFs can be achieved by the electrodeposition of SnO_2 nanoparticles directly onto electrospun CNFs [66, 135]. Electrodeposition is a widely-used technique to modify the properties of carbon nanomaterials and it enables the synthesis of metal oxide particles on one-dimensional carbon surfaces [6, 136]. Compared to other surface coating techniques, such as physical vapor deposition, atomic layer deposition, etc., the electrodeposition method is considered to be feasible, scalable, cost-effective, low-temperature, and controllable processing approach. Electrodeposited SnO_2@CNF composites were previously introduced as binder-free anodes for lithium-ion batteries [66]. However, two main drawbacks have been observed for previously reported electrodeposited SnO_2@CNF composite anodes: limited SnO_2 nanoparticle loading and unstable SEI formation on the anode surface. The loading amount of electrodeposited SnO_2 nanoparticles can be enhanced by increasing the surface area of CNFs while stable SEI formation on the anode surface can be achieved by additional nanoscale carbon coating. This leads to novel carbon-coated SnO_2-electrodeposited nonporous and porous carbon nanofibers (PCNFs) for use as high-capacity anodes for Li-ion batteries. Fabrication procedures are schematically presented in Figure 3.1. Electrospun CNFs and PCNFs were first oxidized to create surface functional groups to serve as defect sites during electrodeposition. SnO_2 nanoparticles were then electrodeposited onto the oxidized nanofibers to obtain SnO_2@CNF and SnO_2@PCNF composites.

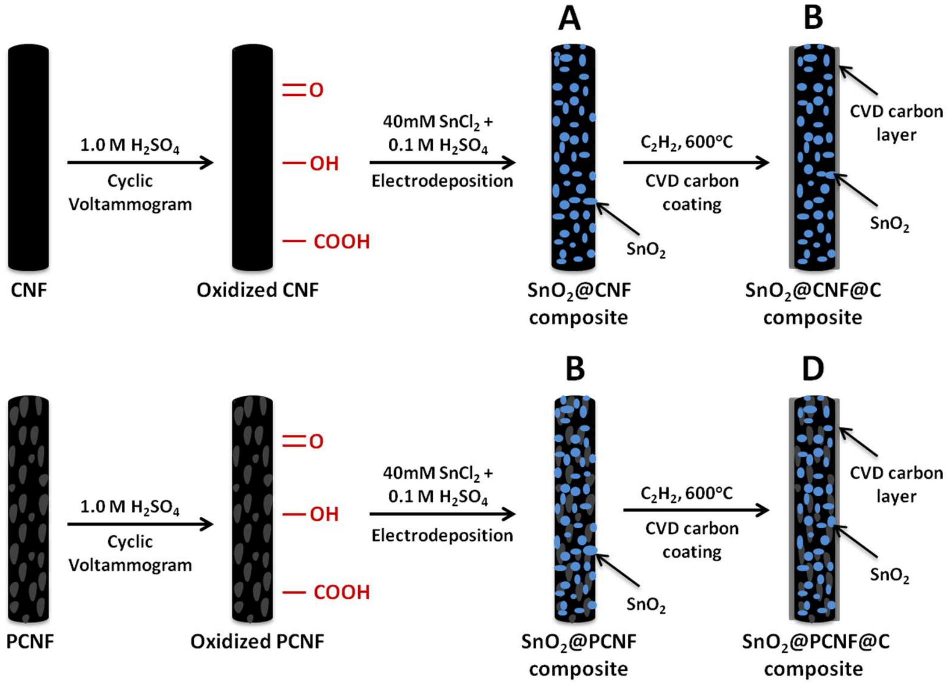

Figure 3.1 : Schematic illustration of the fabrication processes of SnO_2@CNF (A), SnO_2@CNF@C (B), SnO_2@PCNF (C), and SnO_2@PCNF@C (D) composites.

In order to further improve the cycling performance, these nanofiber composites were further coated with nanoscale carbon layers by chemical vapor deposition (CVD) method to form carbon-coated nanofibers, i.e., SnO_2@CNF@C and SnO_2@PCNF@C composites. Electrochemical performance results show that among all nanofiber composites studied, SnO_2@PCNF@C composite has the highest capacity retention of 78% and largest coulombic efficiency of 99.8% even after 100 cycles.

3.2 Experimental

3.2.1 Chemicals and reagents

Polyacrylonitrile (PAN, Pfaltz & Bauer Inc., 150,000 g mol^{-1}), polymethyl methacrylate (PMMA, Aldrich), N,N-dimethylformamide (DMF, Aldrich), tin (II) chloride ($SnCI_2$, Aldrich), and sulfuric acid (H_2SO_4, Aldrich) were used without further purification. Deionized water was used throughout the electrodeposition experiments.

3.2.2 Electrospinning and carbonization of nonporous carbon nanofibers

PAN (8 wt%) was dissolved in DMF and mechanically stirred at 60 ^oC for 24 h. The as-prepared PAN/DMF solution was then electrospun into nanofibers with a flow rate of 0.75 ml/h, a voltage of 16 kV, and a tip-to-collector distance of 20 cm. Electrospun PAN nanofibers were stabilized in air environment at 280 ^oC for 5.5 h with a heating rate of 5 ^oC min^{-1} and then carbonized at 700 ^oC for 2 h in argon atmosphere with a heating rate of 2 ^oC min^{-1}, during which PAN was pyrolyzed to carbon. The resultant CNFs were used as the working electrode in the electrodeposition of SnO_2 nanoparticles.

3.2.3 Electrospinning and carbonization of porous carbon nanofibers

A DMF solution of 8 wt% PAN and PMMA blend (PAN-to-PMMA mass ratio = 9/1) was prepared at 60 ^oC under mechanical stirring for 24 h. The as-prepared PAN/PMMA/DMF solution was then electrospun into nanofibers with a flow rate of 0.75 ml/h, a voltage of 16 kV, and a tip-to-collector distance of 20 cm. Electrospun PAN/PMMA nanofibers were stabilized in air environment at 280 ^oC for 5.5 h with a heating rate of 5 ^oC min^{-1} and then carbonized at 700 ^oC for 2 h in argon atmosphere with a heating rate of 2 ^oC min^{-1}, during which PAN was pyrolyzed to carbon and PMMA was thermally degraded to create a porous structure in the carbon matrix. As-prepared PCNFs were used as the working electrode in the electrodeposition of SnO_2 nanoparticles.

3.2.4 Electrodeposition and CVD coating of nonporous and porous carbon nanofibers

For the electrodeposition process, a three-electrode cell, which composed of a working electrode (CNFs or PCNFs), a counter electrode (Pt wire), and a reference electrode (Ag/AgCl/4.0M KCl), was used. Prior to electrodeposition, CNFs and PCNFs were oxidized in a 1 M H_2SO_4 solution by cyclic voltammetry between -0.7 and 1.2 V at a scan rate of 50 mV s^{-1} for 100 cycles. Electrodeposition of SnO_2 nanoparticles on oxidized CNFs and PCNFs was performed on an AQ4 Gamry Reference 600 electrochemical workstation at room temperature by applying a potential of −0.2V vs. Ag/AgCl/4.0M KCl in a 0.04 M $SnCI_2$ + 0.1 M H_2SO_4 solution for 20 h. Electrodeposited nanofibers were calcinated at 600 ^oC for 1 h in argon atmosphere to obtain SnO_2@CNF and SnO_2@PCNF composites. Electrodeposition experiments were conducted three times for each sample to ensure the reproducibility of the process.

CVD amorphous carbon coating was carried out to obtain SnO_2@CNF@C and SnO_2@PCNF@C composites by using acetylene (C_2H_2) as the carbon precursor gas. Carbon coating of SnO_2@CNF and SnO_2@PCNF composites was accomplished in a horizontal CVD tube furnace (inner tube diameter: around 6.8 cm). The CVD coating process occurred at 600 ^oC for 1 h with 600 sccm flow rate of acetylene while the system was set 20 torr.

3.2.5 Structure characterization

The morphology of composite nanofibers was examined by field emission scanning electron microscope (FE-SEM, JEOL 6400F) and transmission electron microscope (TEM, JEOL JEM-2000FX). The structure of composite nanofibers was investigated by Fourier transform infrared spectroscopy (FTIR, Nicolet Nexus 470), wide angle X-ray diffraction (WAXD, Rigaku Smartlab), and a Renishaw Raman microscope (514 nm).

3.2.6 Electrochemical evaluation

The electrochemical properties of composite nanofibers were tested using CR 2032-type coin cells. These composite nanofibers formed free-standing, conductive nonwoven mats that were used directly as the working electrode without adding polymer binder or conductive agent. Lithium ribbon (99.9%, Aldrich) was used as the counter electrode and Celgard 2400 membrane was used as the separator. The electrolyte consisted of a 1 M solution of $LiPF_6$ dissolved in 1/1 (V/V) ethylene carbonate (EC)/ethylmethyl carbonate (EMC). Coin cells were assembled in a high-purity argon-filled glove box. The electrochemical performance was investigated by carrying out galvanostatic charge-discharge experiments at constant current density of 100 mA g^{-1} (around C/10) with cut-off potentials of 0.01 and 2.00 V using LAND-CT 2001A battery test system. The rate performance was measured using the same instrument at current densities of 100 mA g^{-1}, 200 mA g^{-1}, 400 mA g^{-1}, and 800 mA g^{-1}.

3.3 Results and Discussion

3.3.1 Morphology and structure

As illustrated in Figure 3.1, prior to the electrodeposition process, negatively charged functional groups such as quinoid (=O), hydroxyl (-OH) and carboxyl (–COOH) were created on the surfaces of electrospun CNFs and PCNFs with the oxidation treatment step. These surface functional groups provided defect sites for the deposition of SnO_2 nanoparticles [137]. During the electrodeposition, the SO_4^{2-} ions in the acidic solution were electrochemically reduced on the surfaces of CNFs or PCNFs, leading to the formation of OH^- ions. Further reaction of tin (II) with OH^- ions on the fiber surfaces resulted in the formation of SnO_2 nanoparticles. As-prepared SnO_2@CNF and SnO_2@PCNF composites were then coated with nanoscale amorphous carbon layers by the CVD method.

Figure 3.2 shows the FTIR spectra of CNFs and oxidized CNFs, which confirmed the generated functional groups on fiber surfaces during the oxidation treatment step. For un-oxidized CNFs, two characteristic peaks were indexed at 1280 cm^{-1} and 1590 cm^{-1}, which were attributed to the C–C and C=C stretch bonds, respectively. For oxidized CNFs, broad peaks at 3333 and 2957 cm^{-1} were indexed for the –OH vibration of the –COOH group, and the intense peak at 1162 cm^{-1} was attributed to the –C–O stretching of the –C–OH group. Oxidized CNFs also presented two characteristic bending mode peaks at 1733 cm^{-1} and 1690 cm^{-1}, respectively, corresponding to the –C=O stretch bonds in esters and benzophenones [138].

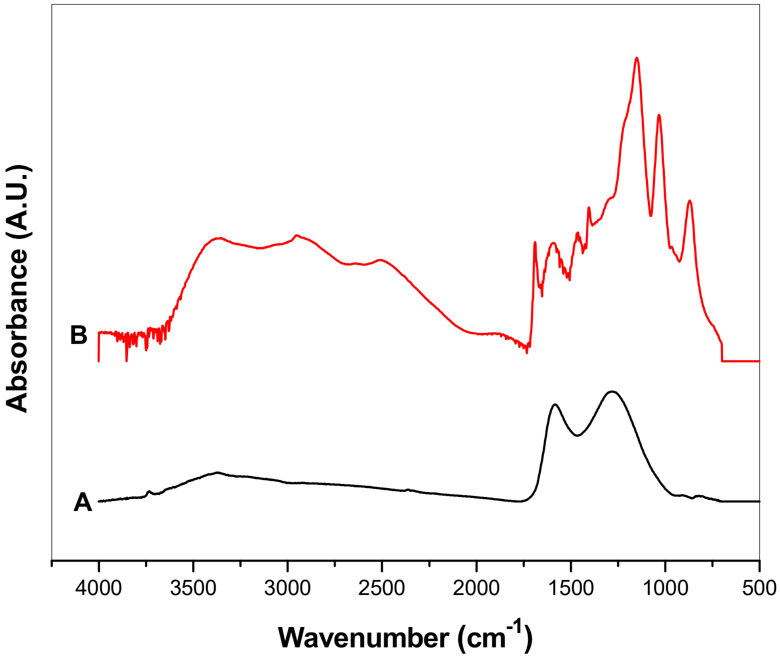

Figure 3.2 : FTIR spectra of CNFs (A) and oxidized CNFs (B).

The successful electrodeposition of SnO_2 on the fiber surfaces was demonstrated by the energy-dispersive X-ray spectroscopy (EDS) analysis (Figure 3.3). The EDS spectrum of SnO_2@PCNF@C composite clearly showed the existence of tin, oxygen, and carbon. The SnO_2 contents in as-prepared nanofiber composites were investigated by the elemental analysis method and the results are shown in Table 3.1. The SnO_2 content is calculated based on the contents of carbon, hydrogen, and nitrogen composition in the SnO2-containing CNF composites. It was seen that SnO_2 contents were 35.7%, 24.1%, 40.8% and 38.5%, respectively, in SnO_2@CNF, SnO_2@CNF@C, SnO_2@PCNF, and SnO_2@PCNF@C composites. The SnO_2 content in SnO_2@PCNF composite was higher than that of SnO_2@CNF composite, indicating that the increased surface area created by the porous structure in PCNFs is beneficial for the electrodeposition of SnO_2 nanoparticles. From Table 3.1, it was also seen that the carbon content increased after CVD carbon coating.

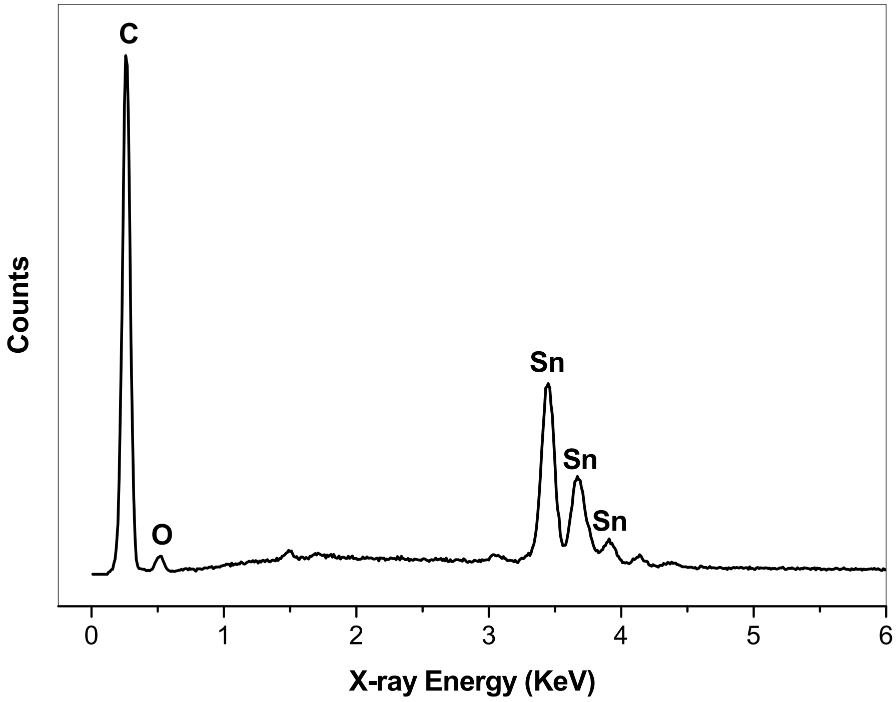

Figure 3.3 : EDS spectrum of SnO_2@PCNF@C composite.

Table 3.1: Compositions of nanofiber composites based on element analysis measurement.

Description of nanofiber composite	**Compositions of nanofiber composites (wt%)**	
	C	**SnO_2**
SnO_2@CNF composite	51.0	35.7
SnO_2@CNF@C composite	62.2	24.1
SnO_2@PCNF composite	47.6	40.8
SnO_2@PCNF@C composite	50.6	38.5

The morphology of SnO_2@CNF, SnO_2@CNF@C, SnO_2@PCNF, and SnO_2@PCNF@C composites was examined by using SEM (Figure 3.4). From the SEM images, it was seen that the surface morphologies of all four nanofiber composites were similar. SnO_2 was electrodeposited uniformly throughout the nanofiber surfaces without forming large aggregations. Although the porous structure and CVD carbon coating cannot be observed from the SEM images due to the limited resolution, TEM characterization was also employed to clearly demonstrate the porous structure and thin CVD carbon coating as discussed below.

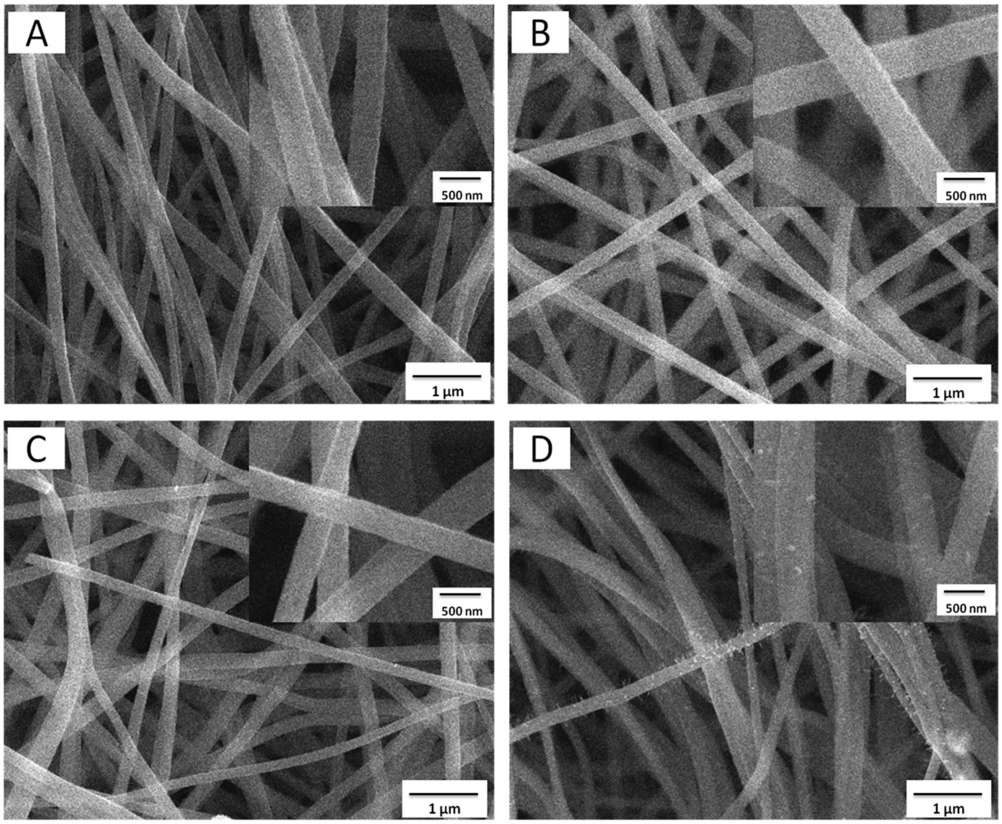

Figure 3.4 : SEM images of SnO_2@CNF (A), SnO_2@CNF@C (B), SnO_2@PCNF (C), and SnO_2@PCNF@C (D) composites.

TEM images of CNFs, SnO_2@CNF, SnO_2@CNF@C, PCNFs, SnO_2@PCNF, and SnO_2@PCNF@C composites were presented in Figure 3.5. Before electrodeposition, the surface of CNFs was smooth (Figure 3.5A) and the porous structure created by the decomposition of PMMA was observable on PCNFs (Figure 3.5D). However, as shown in Fig. 3.5B and E, SnO_2 nanoclusters were formed along the nanofiber surfaces after the electrodeposition. The presence of SnO_2 nanoclusters was more apparent in CVD carbon-coated nanofibers, *i.e.*, SnO_2@CNF@C and SnO_2@PCNF@C composites (Figure 3.5C and F). The CVD carbon coating layers were observable in higher-magnification TEM images, as shown in Figue 3.6. It was seen that the thicknesses of the CVD carbon coating layers on SnO_2@CNF@C and SnO_2@PCNF@C composites were both around 10 nm. These nanoscale carbon coating layers are important for stable SEI formation on the surfaces of active materials during the repetitive electrochemical reactions.

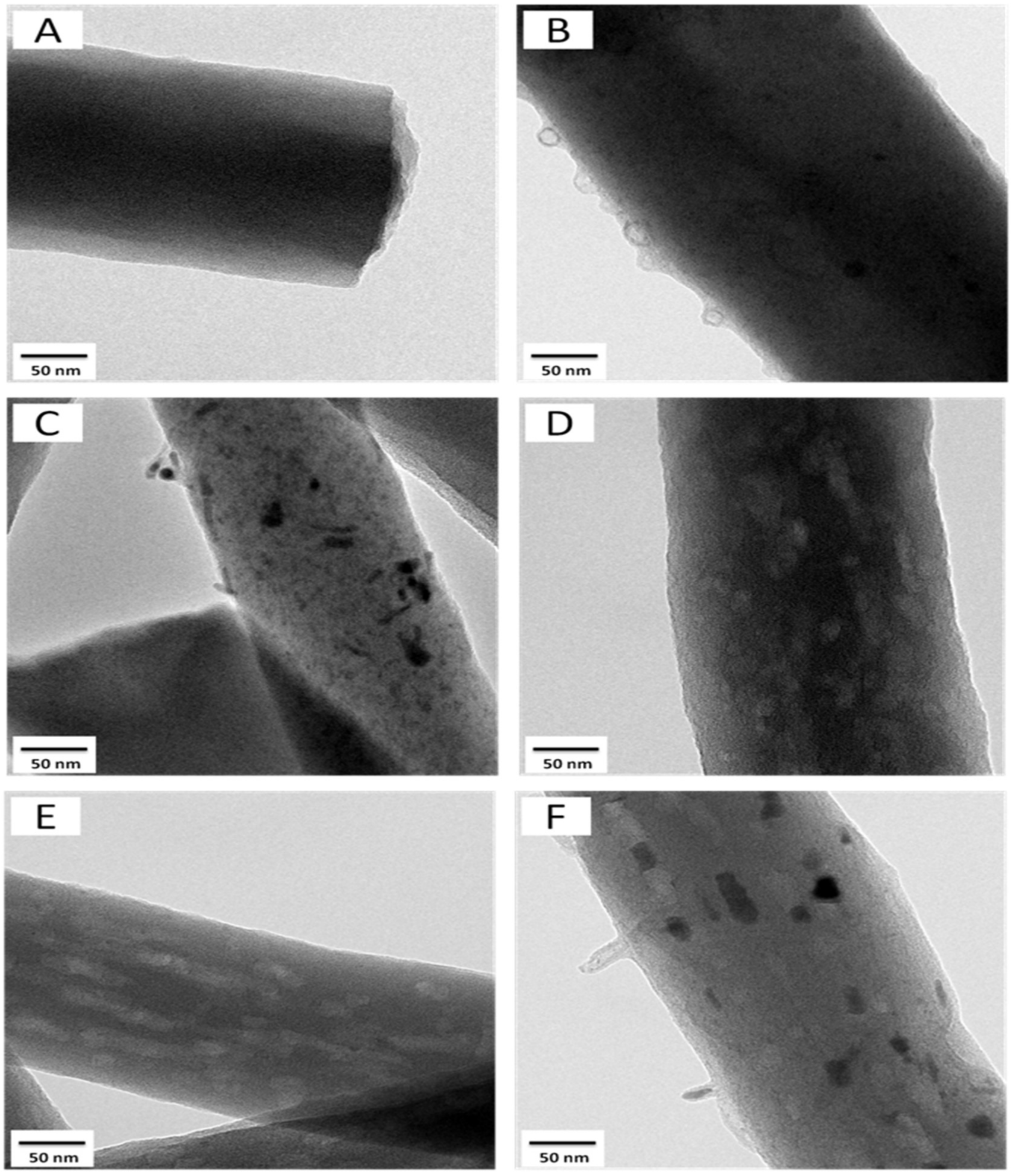

Figure 3.5 : SEM images of SnO_2@CNF (A), SnO_2@CNF@C (B), SnO_2@PCNF (C), and SnO_2@PCNF@C (D) composites.

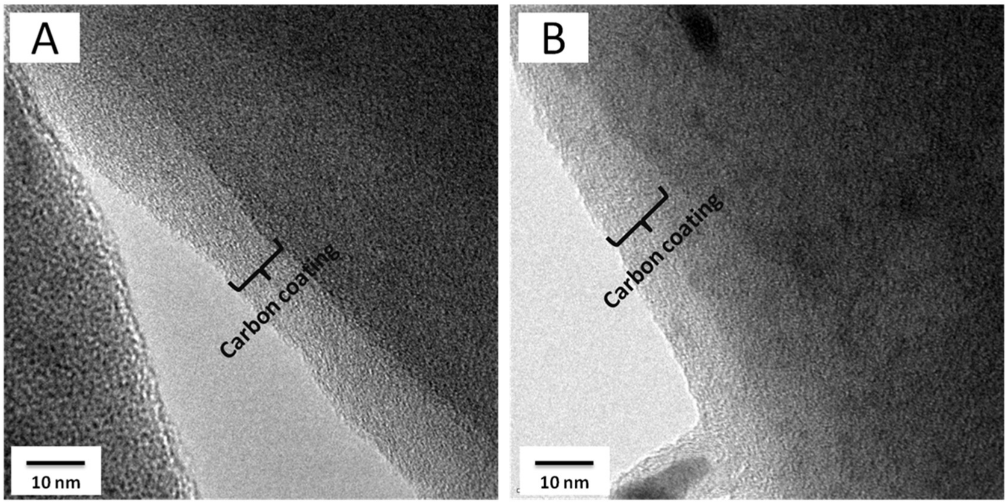

Figure 3.6 : SEM images of SnO_2@CNF (A), SnO_2@CNF@C (B), SnO_2@PCNF (C), and SnO_2@PCNF@C (D) composites.

Figure 3.7 shows X-ray diffraction (XRD) patterns of CNFs, SnO_2@CNF, and SnO_2@CNF@C composites. For comparison, the XRD pattern of un-calcined SnO_2@CNF composite is also shown. Un-calcined SnO_2@CNF composite exhibited diffraction peaks at 2θ of about 27°, 34°, and 52°, which represented the (110), (101), and (211) planes of the SnO_2 phase (JCPDS No. 41-1445), respectively. The intensities of these indexed peaks were relatively low, indicating the small sizes of tetragonal SnO_2 nanocrystals [52, 139]. After calcination, similar peaks were observable for SnO_2@CNF composite, but peak intensities decreased significantly. SnO_2 peak intensities of SnO_2@CNF@C composite were further weakened with the introduction of CVD amorphous carbon coating. In addition, as shown in Figure 3.7, all four nanofiber composites showed a broad and weak diffraction peak at around $2\theta = 25°$, which could be indexed as the (002) planes of disordered carbon structure. This indicates the amorphous nature of both the carbon nanofiber matrix and CVD carbon coating [140].

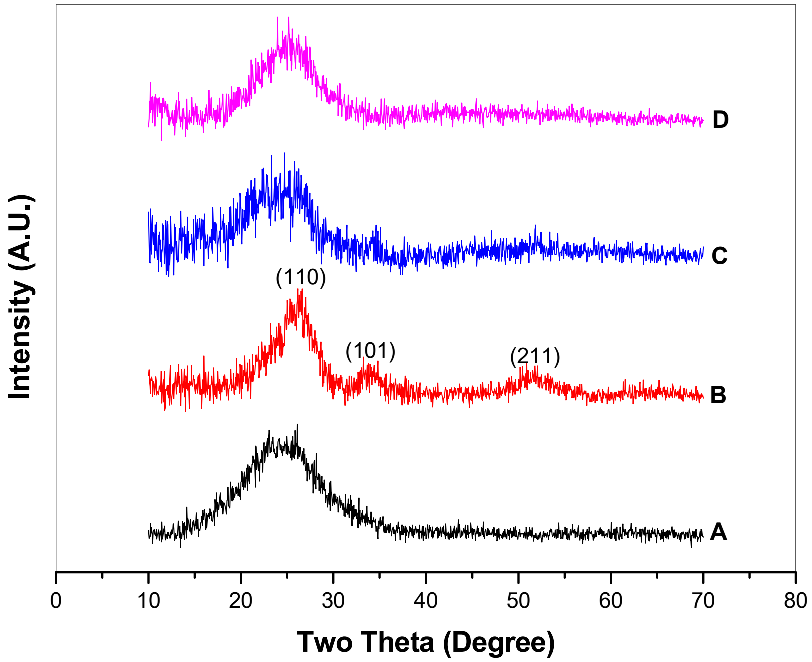

Figure 3.7 : WAXD patterns of CNFs (A), SnO_2@CNF (un-calcined) (B), SnO_2@CNF (C), and SnO_2@CNF@C (D) composites.

3.3.2 Electrochemical performance

In order to evaluate the electrochemical performance of the as-prepared nanofiber composites for use as anodes in lithium-ion batteries, galvanostatic charge-discharge tests were conducted between 0.01 and 2.0 V at a constant current density of 100 mA g^{-1}. From each sample at least twenty cells were assembled and identical capacity results of the assembled cells proved the reproducibility of the prepared anodes. Figure 3.8 shows the galvanostatic charge-discharge profiles for the first, second and fifth cycles of SnO_2@CNF, SnO_2@CNF@C, SnO_2@PCNF, and SnO_2@PCNF@C composites. At the first cycle, the charge capacities were 1167, 1176, 1315, and 1157 mAh g^{-1}, respectively, for SnO_2@CNF, SnO_2@CNF@C, SnO_2@PCNF, and SnO_2@PCNF@C composites. The intention of using PCNF structure was to increase the total surface area and hence the electrodeposition amount of active SnO_2 material. The element analysis has demonstrated that the SnO_2 content in SnO_2@PCNF composite was higher than that in SnO_2@CNF composite (Table 3.1), which was the main reason for SnO_2@PCNF composite to have larger capacity than SnO_2@CNF composite in the first cycle.

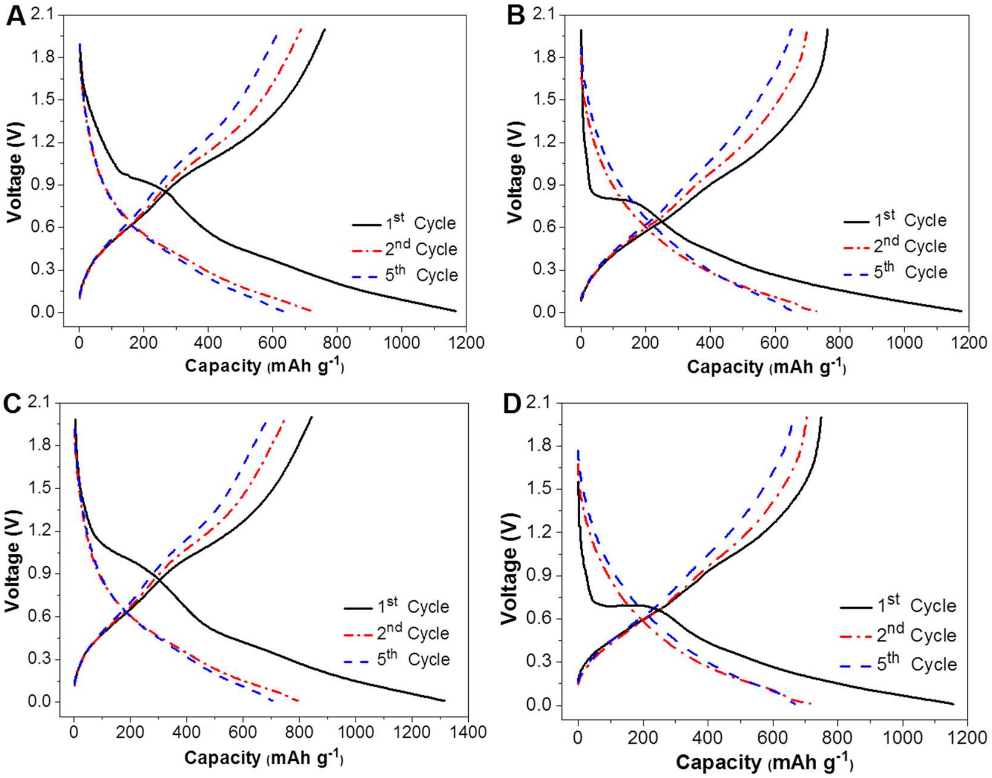

Figure 3.8 : Galvanostatic charge-discharge profiles of (A) CNF@SnO$_2$, (B) CNF@SnO$_2$@C, (C) PCNF@SnO$_2$, and (D) PCNF@SnO$_2$@C composites.

From Figure 3.8, it was also seen the CVD carbon coating reduced the first-cycle charge capacity of SnO$_2$@PCNF@C composite. For all samples, a plateau identified at around 0.8 V at the first charge curve was attributed to the reduction of SnO$_2$ to Sn and Li$_2$O, the decomposition of electrolyte, and the formation of solid electrolyte interface (SEI) layer on the active material surface [141, 142]. In addition, this voltage plateau was extended after CVD carbon coating. Despite the different voltage plateaus of CVD carbon-coated and un-coated nanofiber composites, first-cycle coulombic efficiency values were very similar, i.e., 65.2%, 64.8%, 64.1%, and 64.7% for SnO$_2$@CNF, SnO$_2$@CNF@C, SnO$_2$@PCNF, and SnO$_2$@PCNF@C composites, respectively. The large voltage plateau at ~ 0.8 V at the first cycle is mainly due to the solid-electrolyte-interphase (SEI) formation. It needed to point out that transformation of SnO$_2$ to Li$_x$Sn [142]. As a result, the coulombic efficiencies increased to 94.9%, 95.9%, 94.7%, and 97.5%, respectively, at the second cycle for SnO$_2$@CNF, SnO$_2$@CNF@C, SnO$_2$@PCNF, and SnO$_2$@PCNF@C composites. The coulombic efficiencies of these four nanofiber composites further increased to 98.1%, 98.4%, 98.0%, and 99.1%, respectively, at the fifth cycle. Both at the second and fifth cycles, the coulombic efficiencies of SnO_2@CNF@C and SnO_2@PCNF@C composites were higher than those of SnO_2@CNF and SnO_2@PCNF composites, indicating that the CVD carbon coating was beneficial for the formation of more stable SEI films.

The cycling performance of CNF@SnO_2 and CNF@SnO_2@C composites was evaluated at a constant current density of 100 mA g^{-1} (Figure 3.9). For comparison, the cycling performance of electrospun CNFs is also shown. It was seen that at the 100th cycle, the capacity of electrospun CNFs was around 269 mAh g^{-1} and the corresponding capacity retention was 55.40%. For CNF@SnO_2 composite, the capacity at the 100th cycle was around 469 mAh g^{-1}, which corresponded to increased capacity retention of 61.67%. Based on the CNF@SnO_2 composite composition, the capacity residing with the Sn component at the twentieth cycle was calculated to be 858.9 mAh g^{-1}, which is close to theoretical lithium storage capacity (991 mAh g^{-1}) of pure Sn [50]. The cycling performance was further improved by the introduction of CVD carbon coating. The capacity of CNF@SnO_2@C composite at the 100th cycle was around 528 mAh g^{-1} and the corresponding capacity retention was increased to 69.23%. CNF@SnO_2@C composite also exhibited a high coulombic efficiency of 99.6% at the 100th cycle. This result demonstrated that the nanoscale CVD carbon coating layer supported more stable SEI formation by preventing direct contact of the electrolyte with the active SnO_2 material. Similar effects of nanoscale carbon coating have been observed by Nam, et al., who obtained improved cycling stability for nanoscale carbon-coated spherical SnO_2 nanoparticle anodes [143]. Chen, et al. also demonstrated stable SEI formation on SnO_2 spheres by suitable carbon coating [144].

The cycling performance comparison of PCNFs, PCNF@SnO_2 and PCNF@SnO_2@C composites is demonstrated in Figure 3.10. The capacity of PCNFs, PCNF@SnO_2 and PCNF@SnO_2@C composites at the 100th cycle was 263, 554, and 586 mAh g^{-1}, respectively. Corresponding capacity retentions were 54.90%, 65.67%, and 78.30%, respectively, at the 100th cycle. Therefore, the cycling performance of PCNF@SnO_2 composite was also improved by CVD carbon coating. For the PCNF@SnO_2 composite, the capacity provided by the Sn component at the twentieth cycle was calculated to be 973.5 mAh g^{-1}, which is close to theoretical capacity of Sn. Comparing Figure 3.9 and 3.10, it was seen that the capacity of PCNF@SnO_2@C composite (586 mAh g^{-1}) was higher than that of CNF@SnO_2@C composite (528 mAh g^{-1}) at the 100th cycle. This is probably because of the high SnO_2 content in PCNF@SnO_2@C composite (see Table 1). Among all four different nanofiber composites studied, the highest capacity and capacity retention were achieved by PCNF@SnO_2@C composite. Compared to solid CNFs, porous CNFs could allow more SnO_2 to be deposited on the surface during electrodeposition, leading to higher capacity. In addition, both the porous structure and CVD carbon coating help accommodate the volume change of SnO_2 particles, thereby resulting in improved cycling performance. The CVD carbon coating can also stabilize the SEI formation on the surface, which is beneficial in increasing the coulombic efficiency. Similar design has been used by Wu et al., who prepared CNT@SnO_2@C coaxial nanocables with different carbon thicknesses to improve the cycling performance of CNT@SnO_2 anodes [133]. Their results demonstrated that without the porous structure, the capacity of CNT@SnO_2@C coaxial nanocables decreased to less than 600 mAh g^{-1} after 10 cycles even with a thick carbon coating of 10 nm.

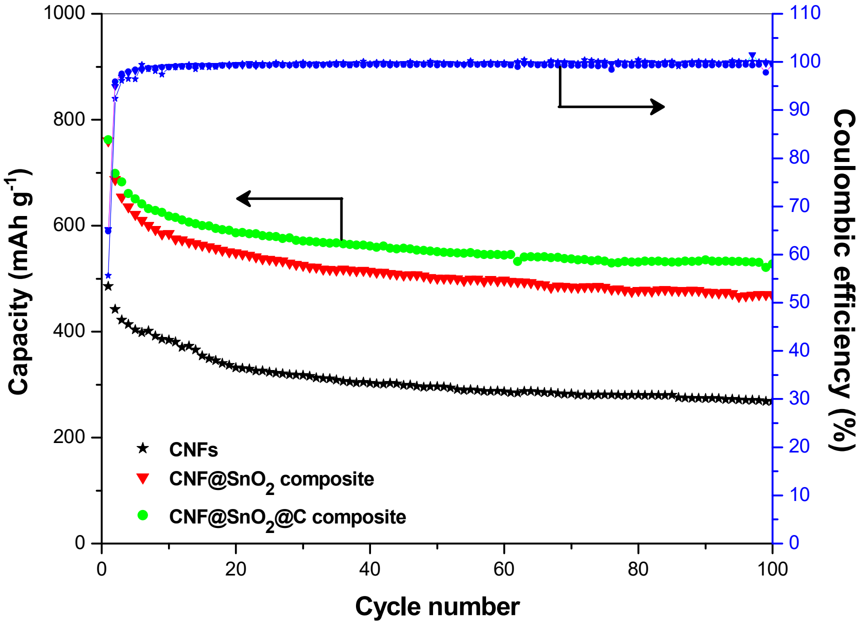

Figure 3.9 : Cycling performance comparison of CNFs, CNF@SnO_2, and CNF@SnO_2@C composites.

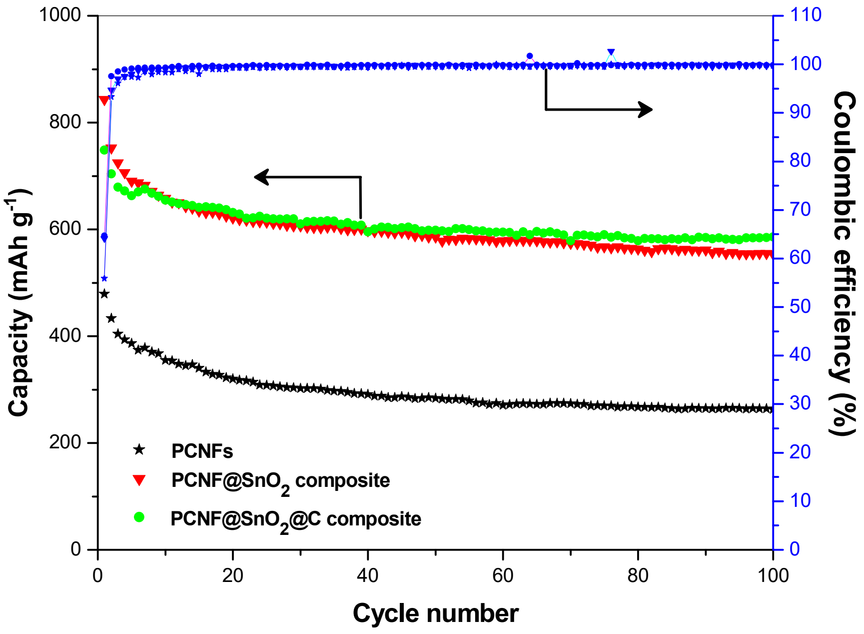

Figure 3.10 : Cycling performance comparison of PCNFs, PCNF@SnO$_2$, and PCNF@SnO$_2$@C composites.

The rate capability of PCNF@SnO$_2$@C composite, which showed the best cycling performance among all studied nanofiber composites, was investigated under different current densities (Figure 3.11). The average charge capacity values of PCNF@SnO$_2$@C composite were around 713, 568, 463, and 398 mAh g^{-1}, respectively, at 100, 200, 400, and 800 mA g^{-1}. The coulombic efficiency did not show apparent change as the current density increased and it was still more than 99% even at the highest current density of 800 mA g^{-1}. The charge capacity value returned to 600 mAh g^{-1} under a reduced current density of 100 mAh g^{-1} after undergoing cycles at higher current densities. This charge capacity (600 mAh g^{-1}) was similar to the initial charge capacities, which also demonstrated the good rate capability of PCNF@SnO$_2$@C composite.

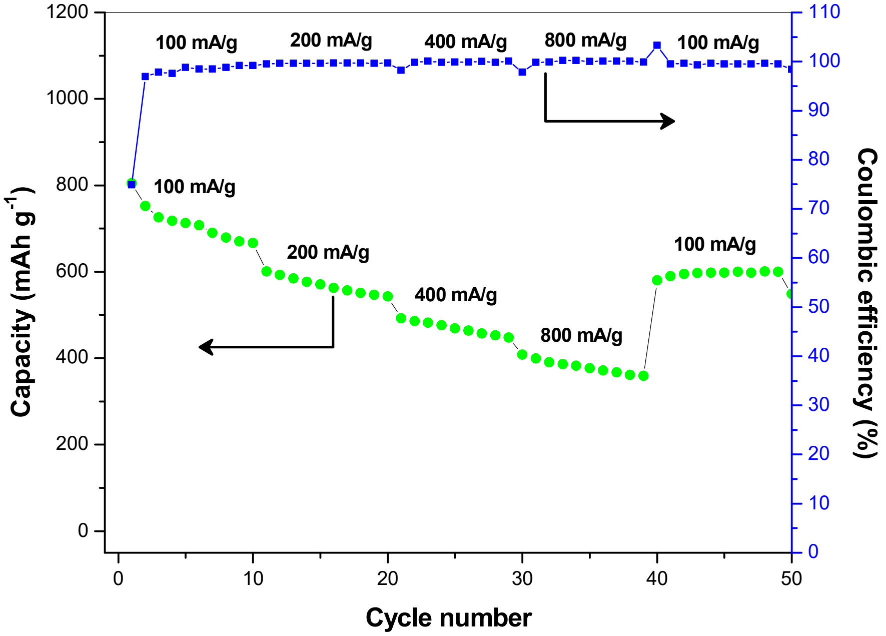

Figure 3.11 : Rate capability of PCNF@SnO_2@C composite cycled at different current densities.

3.4 Conclusions

CNF@SnO_2 and PCNF@SnO_2 composites were developed as binder-free anodes for lithium-ion batteries by the electrodeposition of SnO_2 nanoparticles on electrospun carbon nanofibers. To achieve improved cycling performance, additional CVD amorphous carbon coating was also applied to form CNF@SnO_2@C and PCNF@SnO_2@C composites. It was found that the amount of electrodeposited SnO_2 nanoparticles and corresponding capacity value increased by using the PCNF structure. The capacity of PCNF@SnO_2 composite was measured to be 554 mAh g^{-1} at the 100th cycle, which was higher than that (469 mAh g^{-1}) for CNF@SnO_2 composite. In addition, the long-term cycling performance of both CNF@SnO_2 and PCNF@SnO_2 composites was improved with nanoscale CVD carbon coating on the fiber surfaces. At the 100 cycle, the capacity retentions of the resultant CNF@SnO_2@C and PCNF@SnO_2@C composites were 69.23% and 78.30%, respectively. It was, therefore, demonstrated that among all nanofiber composites studied, PCNF@SnO_2@C composite is the most promising anode material candidate with the largest capacity and best cycling performance.

4. CARBON-CONFINED PVA-DERIVED SILICON/SILICA/CARBON NANOFIBER COMPOSITES AS ANODE FOR LITHIUM-ION BATTERIES

4.1 Introduction

Electrochemical energy storage has been demonstrated as one of the most promising technologies for different applications such as grid storage, electric vehicles, and portable electronic devices [82, 145, 146]. Because of their superior properties, including high energy density, good cycle life and good power performance, lithium-ion batteries are considered as the most preferred rechargeable battery technology in recent years [5, 147, 148]. The development of high-capacity electrode materials for high-energy lithium-ion batteries is critically important for technological improvements on portable electronics and electric vehicles that use lithium-ion batteries as the power source [67, 68].

Current commercial lithium-ion batteries use graphitic materials in the anode. However, graphitic anode materials cannot meet the capacity requirements of future portable electronics because of their low specific capacity of 372 mAh g^{-1} [67, 69, 70]. Lithium storage capacities of alloy-type anodes, such as silicon (Si), tin, germanium, etc., are much higher than that of commercially-used intercalation-type graphite anodes. Among all alloy-type anodes, Si has the highest theoretical capacity of 4200 mAh g^{-1}, making it the best candidate for next-generation high-energy lithium-ion batteries [71, 72, 149]. However, the insertion of lithium ions into Si during cycling induces large volumetric change (up to 400%), which causes intense pulverization of active Si material, loss of electrical contact between Si and carbon conductor, and unstable solid electrolyte interphase (SEI) formation on the Si surface [73-75]. These drawbacks bring together the performance degradation of active Si material during repetitive lithitation and delithitation processes [150, 151].

This chapter consists of the article below:

Dirican, M., Yanilmaz, M., Fu, K., Yildiz, O., Kizil, H., Hu, Y., and Zhang, X. (2014). Carbon-confined PVA-derived silicon/silica/carbon nanofiber composites as anode for lithium-ion batteries, *Journal of The Electrochemical Society, 161*, A2197-A2203.

To eliminate the aforementioned drawbacks, Si-based composite anodes have been widely investigated. Among them, Si/carbon (Si/C) composites have drawn great attention, which can potentially combine the advantageous properties of Si (high capacity) and C (excellent electronic conductivity and structural stability) [152]. Maintaining the structural integrity of the electrode despite the 400% volume expansion of Si and stabilizing the SEI structure during cycling processes are, hence, the most crucial challenges for the development of Si/C based anodes [76, 77]. So far, there are several novel strategies for preserving the structural integrity of Si/C anode materials. One of them is to reduce the size of Si particles into nanoscale range to minimize the cracking and pulverization of these particles [78, 79, 153]. Another strategy is to create open spaces between active Si particles and carbon matrix to accommodate the volume expansions of Si during cycling [80, 81].

In this study, two different Si/C based anodes were synthesized: Si/SiO_2/C nanofiber composite and chemical vapor deposition (CVD) carbon-coated Si/SiO_2/C nanofiber composite. The fabrication approach of these two composites is schematically illustrated in Figure 4.1. Si/SiO_2/polyvinyl alcohol (PVA) nanofiber composites were first produced by electrospinning of a mixture of silicon nanoparticles, sol-gel tetraethyl orthosilicate (TEOS) solution, and aqueous PVA solution. TEOS is a common precursor for making SiO_2 material [154] while PVA is a promising candidate to produce electrospun carbon nanofibers because of its environmentally friendliness feature [122, 147]. After electrospinning, the resultant Si/SiO_2/PVA nanofiber composites were carbonized to obtain Si/SiO_2/C nanofibers, which formed free-standing conductive nonwoven mats and were used directly as binder-free anodes for lithium-ion batteries. Si/SiO_2/C nanofibers were also coated with nanoscale amorphous carbon layer by CVD technique to ensure maintaining of the Si nanoparticles within the carbon nanofiber matrix during repetitive charging and discharging processes. Electrochemical tests showed that among all nanofibers studied, CVD carbon-coated Si/SiO_2/C nanofiber composites exhibited the highest capacity retention of 91% and largest coulombic efficiency of 97.4% at the 50th cycle.

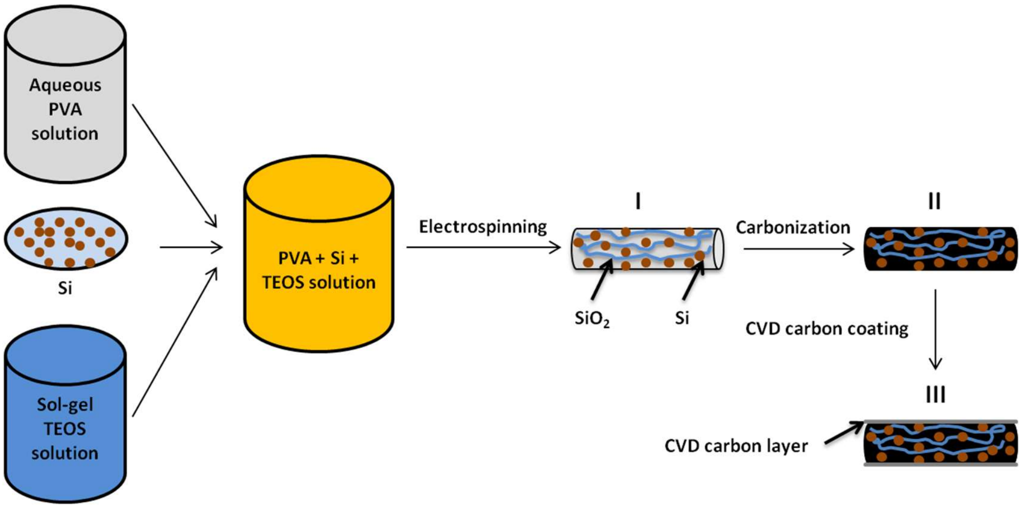

Figure 4.1 : Schematic illustration of the fabrication process of Si/SiO2/PVA nanofibers (I), Si/SiO2/C nanofibers (II), and CVD carbon-coated Si/SiO2/C nanofibers (III).

4.2 Experimental

4.2.1 Nanofiber preparation

TEOS (99%), PVA (MW = 85,000-124,000 g/mol, 88% hydrolized), ethanol, hydrochloric acid (HCl, 37%), and N,N-dimethylformamide (DMF) were supplied from Sigma-Aldrich. Si nanoparticles (diameter: 30-50 nm) were obtained from Nanostructures & Amosrphous Materials, Incorporated. Deionized water was used throughout the experiments. All chemicals were used without further purification.

PVA solution (5 wt%) in deionized water was prepared at 80 ^{o}C and mechanically stirred for 24 h. TEOS solution was prepared by dissolving TEOS in ethanol, followed by adding deionized water and HCl, respectively. The molar ratio of the TEOS solution was TEOS:water:ethanol:HCl = 1:3:8:0.04 [155]. The TEOS solution was stirred at room temperature for 3 h and was then gradually added to the PVA solution, followed by stirring for additional 3 h. Si nanoparticles (17 wt% with respect to PVA) were added into the as-prepared TEOS/PVA solution and stirred at room temperature for 24 h, followed by ultrasonic treatment for 1 h to obtain a homogenous dispersion. The as-prepared Si/SiO_2/PVA dispersion was then electrospun into nanofibers with a flow rate of 0.80 ml/h, a voltage of 18 kV, and a tip-to-collector distance of 25 cm.

Electrospun nanofibers was stabilized in air environment at 280 ^{o}C for 5.5 h with a heating rate of 5 ^{o}C min^{-1} and then carbonized at 700 ^{o}C for 2 h in argon atmosphere with a heating rate of 2 ^{o}C min^{-1}, during which PVA was pyrolyzed to carbon. The

$Si/SiO_2/C$ nanofiber composite was further coated with amorphous carbon by the CVD method using acetylene (C_2H_2) as the carbon precursor gas. CVD carbon coating was applied at 700 °C for 1 h with 600 sccm flow rate of acetylene while the system was settled at 20 torr. For comparison, Si/C nanofibers were also prepared using the same electrospinning and thermal treatment procedures from a Si/PVA solution (17 wt% with respect to PVA) without the addition of TEOS.

4.2.2 Structure characterization

The morphology of composite nanofibers was examined by field emission scanning electron microscope (FE-SEM, JEOL 6400F) and transmission electron microscope (TEM, JEOL JEM-2000FX). The structure of composite nanofibers was investigated by Fourier transform infrared spectroscopy (FTIR, Nicolet Nexus 470), wide angle X-ray diffraction (WAXD, Rigaku Smartlab), and Renishaw Raman microscope.

4.2.3 Electrochemical evaluation

The electrochemical properties of composite nanofibers were tested using CR 2032-type coin cells. These composite nanofibers formed free-standing, conductive nonwoven mats that were used directly as the working electrode without adding polymer binder or conductive agent. Lithium ribbon (99.9%, Aldrich) was used as the counter electrode and Celgard 2400 membrane was used as the separator. The electrolyte consisted of a 1 M solution of LiPF6 dissolved in ethylene carbonate (EC)+dimethyl carbonate (DMC)+diethyl carbonate (DEC) (1:1:1 by volume, MTI Corporation). Coin cells were assembled in a high-purity argon-filled glove box. The electrochemical performance was investigated by carrying out galvanostatic charge-discharge experiments at a constant current density of 100 mA g-1 (around C/10) with cut-off potentials between of 0.01 and 2.00 V on a LAND-CT 2001A battery test system.

4.3 Results and Discussion

4.3.1 Morphology and structure

Figure 4.1 shows schematic illustration of the fabrication process of $Si/SiO_2/PVA$ nanofibers, $Si/SiO_2/C$ nanofibers, and CVD carbon-coated $Si/SiO_2/C$ nanofibers. The fabrication process of nanofiber electrodes consisted of three simple steps: electrospinning of Si/PVA/TEOS solution into $Si/SiO_2/PVA$ nanofibers, carbonization of electrospun nanofibers to obtain $Si/SiO_2/C$ composite nanofiber, and CVD carbon coating of $Si/SiO_2/C$ nanofibers. It was found that without the presence of SiO_2, PVA-derived carbon nanofibers and Si/C nanofibers did not form free-standing mats. On the other hand, after the induction of SiO_2, the resultant SiO_2/C nanofibers and $Si/SiO_2/C$ nanofibers formed free-standing and stable mat structure.

Figure 4.2 shows the FTIR spectra of PVA nanofibers, SiO_2/PVA nanofibers, Si/SiO_2/PVA nanofibers, $Si/SiO_2/C$ nanofibers, and CVD carbon-coated $Si/SiO_2/C$ nanofibers. PVA nanofibers showed the peaks at 3320 cm^{-1}, 2920 cm^{-1}, 1740 cm^{-1} and 1310 cm^{-1}, respectively, corresponding to –OH stretching, –CH stretching, –C=O stretching and scissoring vibration of $–CH_2$. The peaks at 1080 cm^{-1} and 836 cm^{-1} were attributed to the C–O–H stretching movement in aliphatic alcohols and out-of plane vibration of –CH [155]. For SiO_2/PVA nanofibers, the peak at 1060 cm^{-1} was attributed to asymmetric Si–O–Si stretching motion and the band at 930–950 cm^{-1} was attributed to Si-OH. The presence of Si–O–Si in the SiO_2/PVA nanofibers demonstrates the formation of the silica network in the electrospun composite nanofibers. When SiO_2 was formed in the PVA matrix, the –OH stretching peak of PVA at around 3300 cm^{-1} was reduced, which could be explained by the intermolecular interaction between the –OH groups of PVA and silica [155-157]. In addition, the broad Si–O–Si peak around 1100 cm^{-1} contained a shoulder at around 1200 cm^{-1}, which could be attributed to the reaction between –OH groups of PVA and silanol groups of silica. The formation of this new bond and the reduction of –OH bond intensity demonstrated that silica crosslinked with PVA and formed a network structure containing Si–O–PVA–O–Si bridges (Figure 4.3). This network structure helped maintain the structure integrity of the nanofibers during carbonization and led to the formation of free-standing, stable SiO_2/C nanofiber mats. From Figure 4.2, it is also seen that Si/SiO_2/PVA nanofibers also had a characteristic SiO_2 peak at around 1100 cm^{-1}, corresponding to the symmetric stretching, asymmetrical stretching, and bending vibrations in Si-O-Si bonds [155]. The shoulder at around 1200 cm^{-1} indicated that the reaction between –OH groups of PVA and silanol groups of silica was not interrupted by the addition of Si nanoparticles. Therefore, the Si-O-PVA-O-Si containing network structure was also formed in $Si/SiO_2/C$ nanofibers, leading to the formation of free-standing $Si/SiO_2/C$ nanofiber mats after carbonization. In the FTIR spectra of $Si/SiO_2/C$ nanofibers and CVD carbon-coated $Si/SiO_2/C$ nanofibers, the peaks around 1100 cm^{-1} (asymmetry Si-O-Si bond stretching and O-Si-O bond deformation) were attributed to the SiO_2 ingredient in the carbonized nanofibers [156, 157]. The high intensities of observed characteristic SiO_2 peak of Si/SiO_2/C nanofibers and CVD carbon-coated Si/SiO_2/C nanofibers indicated the preserving of the SiO_2 structure during the carbonization and subsequent CVD carbon coating processes.

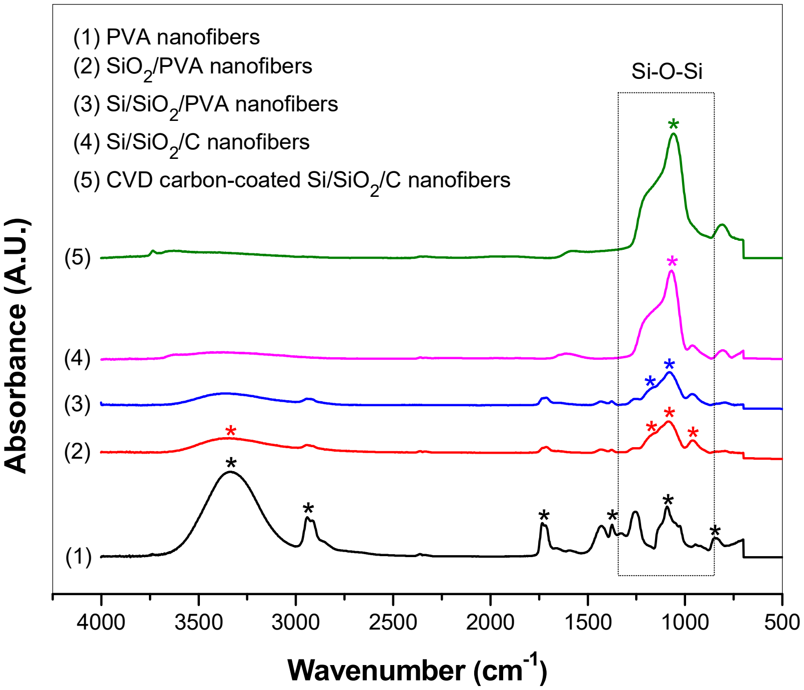

Figure 4.2 : FTIR spectra of PVA nanofibers, SiO_2/PVA nanofibers, Si/SiO_2/PVA nanofibers, Si/SiO_2/C nanofibers, and CVD carbon-coated Si/SiO_2/C nanofibers.

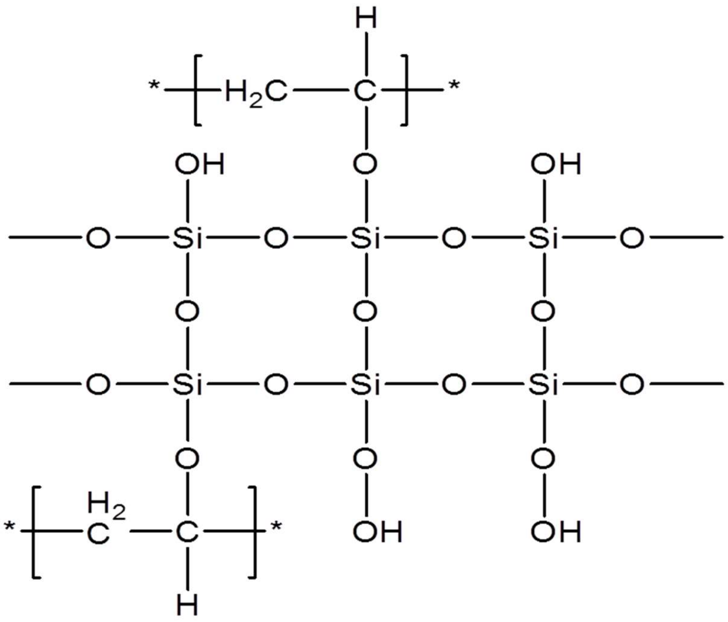

Figure 4.3 : Schematic of SiO_2/PVA network structure.

The morphology of Si/SiO_2/PVA nanofibers, Si/SiO_2/C nanofibers and CVD carbon-coated Si/SiO_2/C nanofibers was examined by SEM, and the results are shown in Figure 4.4. Continuous nanofibers with agglomerated nanoparticles and/or clusters were observed from the SEM image of electrospun Si/SiO_2/PVA nanofibers (Figure 4.4A). From Figures 4.4B and C, it was seen that the surface morphologies of Si/SiO_2/C nanofibers and CVD carbon-coated Si/SiO_2/C nanofibers were similar. Si nanoparticles were agglomerated on the nanofiber surfaces. From the SEM image of CVD carbon-coated Si/SiO_2/C nanofibers, the amorphous CVD carbon coating layers were not apparent. To clearly observe the thin amorphous CVD carbon layers, TEM observation was carried out, as discussed below.

Figure 4.5 shows TEM images of a Si/SiO_2/C nanofiber and a CVD carbon-coated Si/SiO_2/C nanofiber. For comparison, the TEM image of a carbonized SiO_2/C nanofiber without any Si nanoparticles is also shown. From Figure 4.5A, it is seen that SiO_2 clusters were formed along the longitudinal direction of the SiO_2/C nanofiber. The introduction of Si nanoparticles changed the morphology of nanofiber composites. As shown in Figures 4.5B and C, most Si nanoparticles were confined in the nanofiber matrix with some nanoparticles were agglomerated and located on nanofiber surfaces, which agree with the SEM observation in Figure 4.4. High-magnification TEM image is shown in Figure 4.5D to illustrate the CVD amorphous coating layer on a CVD carbon-coated Si/SiO$_2$/C nanofiber. It is seen that the surface of the CVD carbon-coated Si/SiO$_2$/C nanofiber was coated with an amorphous carbon layer of around 15 nm thick. The nanoscale carbon coating layer is important for stable SEI formation on the active material surface during the repetitive electrochemical reactions.

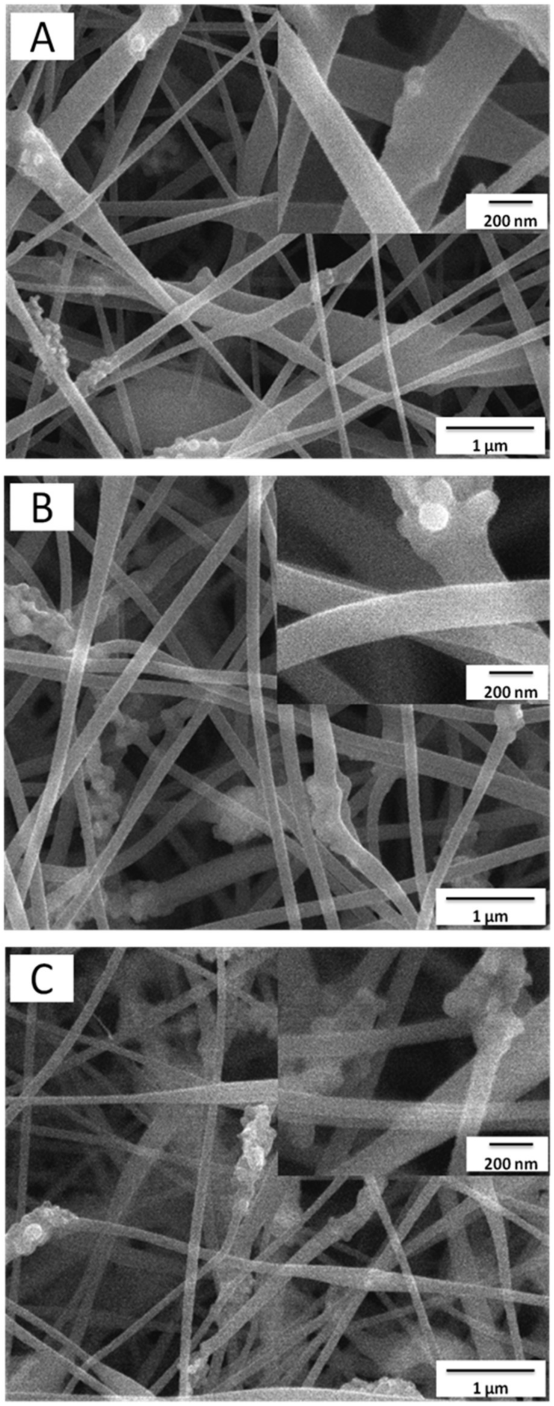

Figure 4.4 : SEM images of Si/SiO$_2$/PVA nanofibers (A), Si/SiO$_2$/C nanofibers (B), and CVD carbon-coated Si/SiO$_2$/C nanofibers (C).

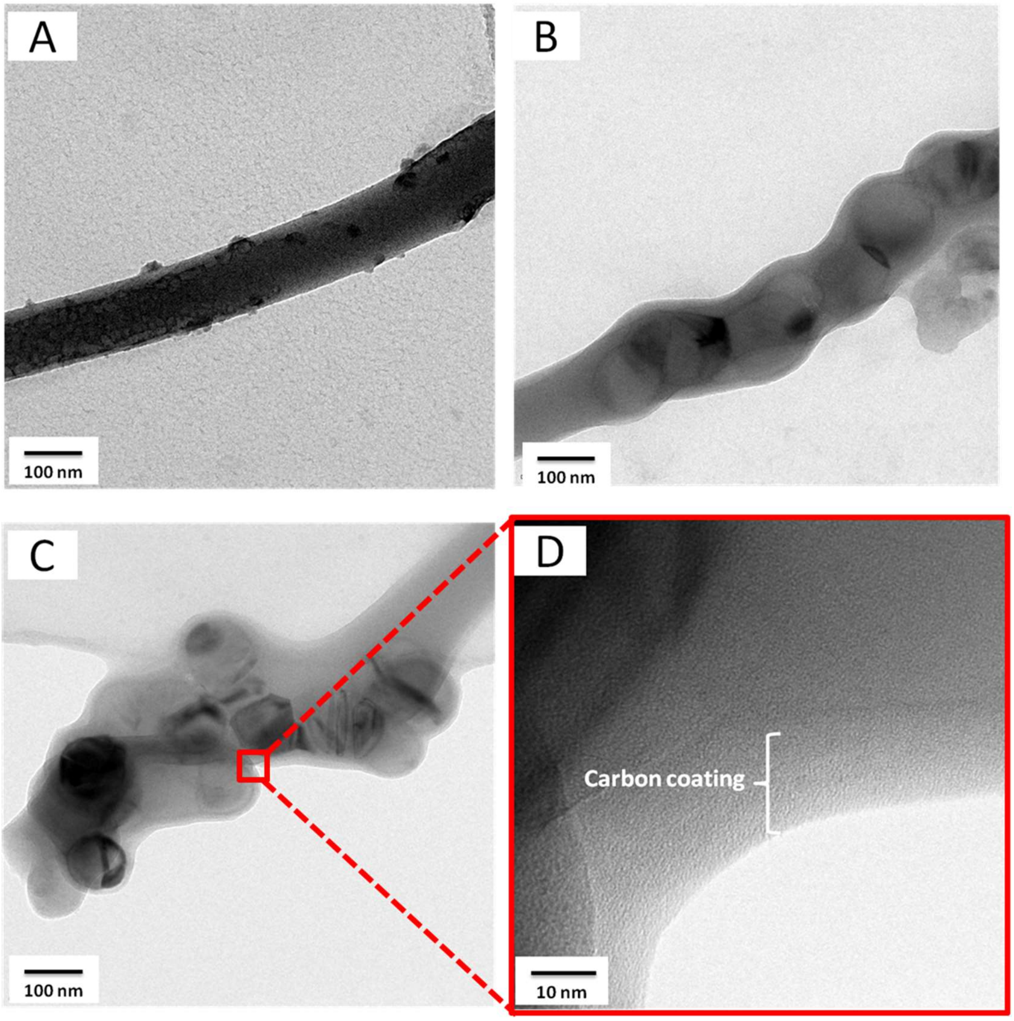

Figure 4.5 : TEM images of SiO_2/C nanofibers (A), Si/SiO_2/C nanofibers (B), CVD carbon-coated Si/SiO_2/C nanofibers (C), and high-magnification TEM image of CVD carbon-coated Si/SiO_2/C nanofibers (D).

The X-ray diffraction (XRD) patterns of Si/SiO_2/C nanofibers and CVD carbon-coated Si/SiO_2/C nanofibers are shown in Figure 4.6. For these nanofiber composites, similar diffraction peaks were indexed. Diffraction peaks at 2θ of about 29°, 47°, 56°, 69°, 76°, and 88° represent the (111), (220), (311), (400), (331), and (422) planes of Si crystals in carbon nanofiber composites, respectively [158, 159]. SiO_2 peaks were not detected by XRD probably due to the amorphous nature of the as-prepared SiO_2 structure. The broad and weak diffraction peak at around $2\theta = 25°$ could be indexed as the (002) planes of disordered carbon structure, indicating the amorphous nature of the carbon nanofiber matrix and CVD carbon coating [140, 160].

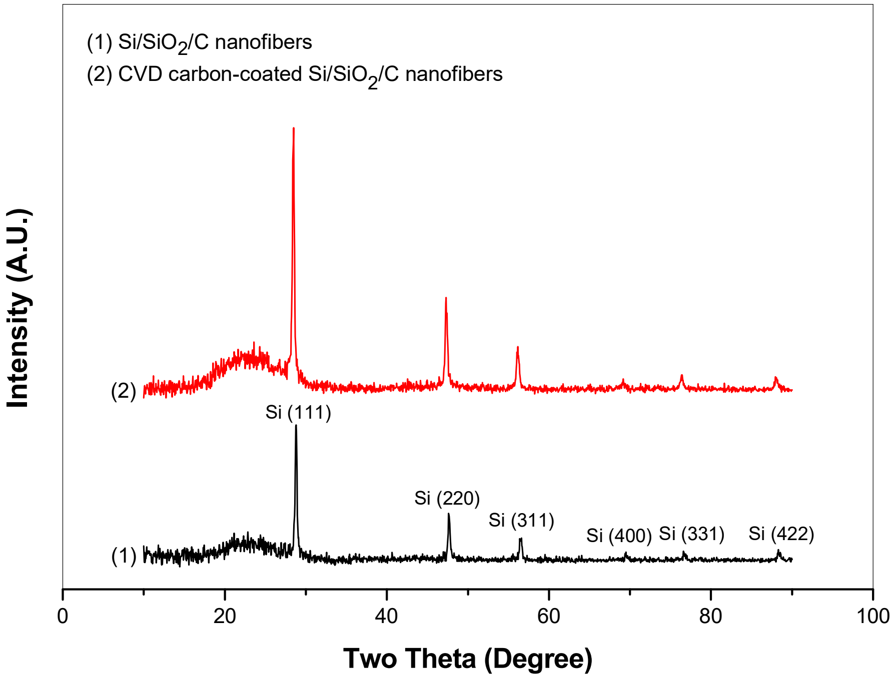

Figure 4.6 : WAXD patterns of $Si/SiO_2/C$ nanofibers and CVD carbon-coated $Si/SiO_2/C$ nanofibers.

The structural evolution of the nanofiber composites was also investigated by Raman spectroscopy. Figure 4.7 shows the Raman spectra of $Si/SiO_2/C$ nanofibers and CVD carbon-coated $Si/SiO_2/C$ nanofibers. For these nanofiber composites, the characteristic carbon peaks of D-band (1360 cm^{-1}), representing the disordered sp^2 phase, and G-band (1582 cm^{-1}), indicating the in-plane stretching vibration mode of E_{2g} graphite, were observed [161, 162]. The relative intensity ratio (i.e., *R*-value) of D-band to G-band represents the degree of disorder in the structure. Typically, a higher *R*-value indicates a higher degree of disorder within the carbon structure [161, 163]. As shown in Figure 4.7, the *R*-values of $Si/SiO_2/C$ nanofibers and CVD carbon-coated $Si/SiO_2/C$ nanofibers were 0.66 and 0.77, respectively. This indicates that the carbon layer coated by CVD method is more disordered than the carbon nanofiber matrix. From Figure 4.7, it is also seen that due to the presence of Si nanoparticles, these nanofiber composites exhibited a Si peak at around 522 cm^{-1}, which is a position for the transverse optical phonon [164]. $Si/SiO_2/C$ and CVD carbon-coated $Si/SiO_2/C$ nanofibers also had a broad and weak peak at around 900 cm^{-1}, representing the SiO_2 component [165].

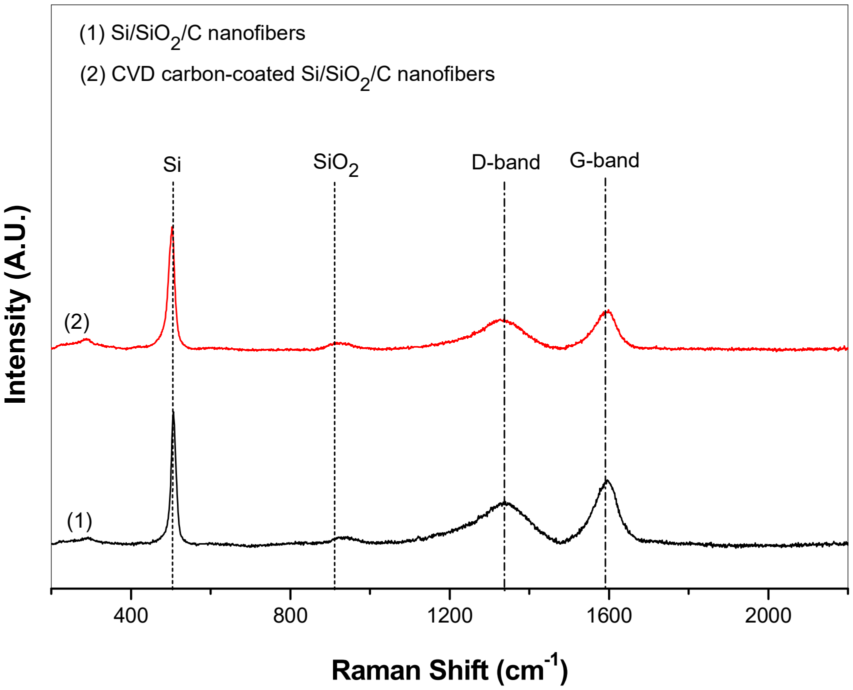

Figure 4.7 : Raman spectra of $Si/SiO_2/C$ nanofibers and CVD carbon-coated $Si/SiO_2/C$ nanofibers.

4.3.2 Electrochemical performance

In order to evaluate the electrochemical performance of the nanofiber composite anodes, galvanostatic charge-discharge tests were conducted between 0.01 and 2.0 V at a constant current density of 100 mA g^{-1}. In this study, the lithiation process is referred to discharge while the de-lithiation process is referred to charge. Figure 4.8 shows the galvanostatic charge-discharge profiles for the first, second and fifth cycles of $Si/SiO_2/C$ nanofibers and CVD carbon-coated $Si/SiO_2/C$ nanofibers. For comparison, the profiles of Si/C nanofibers without the presence of SiO_2 are also shown. At the first cycle, the discharge capacities were 2518, 1275, and 1059 mAh g^{-1}, respectively, for carbonized Si/C nanofibers, $Si/SiO_2/C$ nanofibers, and CVD carbon-coated $Si/SiO_2/C$ nanofibers. Because Si/C nanofibers were composed of only active Si and C without the inactive SiO_2 ingredient, the first cycle discharge capacity of Si/C nanofibers was much higher than those of $Si/SiO_2/C$ nanofibers and CVD carbon-coated $Si/SiO_2/C$ nanofibers. However, the capacity of Si/C nanofibers decreased dramatically (from 2518 mAh g^{-1} to 652 mAh g^{-1}) at the second cycle. On the other hand, $Si/SiO_2/C$ nanofibers and CVD carbon-coated $Si/SiO_2/C$ nanofibers showed much lower capacity losses after the first charging process. From Figure 4.8, it was also seen that at the first cycle, $Si/SiO_2/C$ nanofibers exhibited a long voltage plateau at around 0.2 V; however, this voltage plateau was shortened after CVD carbon coating. The voltage plateau at around 0.2 V could be attributed to the alloying reaction of lithium with silicon particles exposed to the SiO_2/C nanofiber surface. From Figure 4.8, it is also seen that the charge capacities of $Si/SiO_2/C$ nanofibers and CVD carbon-coated $Si/SiO_2/C$ nanofibers increased in the second and fifth cycles.

The cycling performance and coulombic efficiencies of Si/C nanofibers, $Si/SiO_2/C$ nanofibers, and CVD carbon-coated $Si/SiO_2/C$ nanofibers are shown in Figure 4.9. For Si/C nanofibers, the capacity retention and coulombic efficiency at the 50th cycle were around 47% and 98%, respectively. Because of the intense capacity loss after the first discharge process, the capacity of Si/C nanofibers was much lower than those of $Si/SiO_2/C$ nanofibers and CVD carbon-coated $Si/SiO_2/C$ nanofibers. For $Si/SiO_2/C$ nanofibers, relatively stable cycling was achieved without dramatic capacity loss. At the 50th cycle, the capacity retention and coulombic efficiency of $Si/SiO_2/C$ nanofibers were around 80% and 96%, respectively. Introduction of SiO_2 led to improvement in the cycling performance. This result could be attributed to the stable SiO_2/C network structure because the amorphous SiO_2 within the composite nanofiber structure reduced to Li_2O and Li_4SiO_4 in the initial lithiation process, which could help buffer the volume change caused by the alloying of Si nanoparticles with Li, and thereby increasing the cycling stability by minimizing the pulverization of the active Si material and the loss of electrical contact between Si nanoparticles and the carbon nanofiber matrix [157, 166].

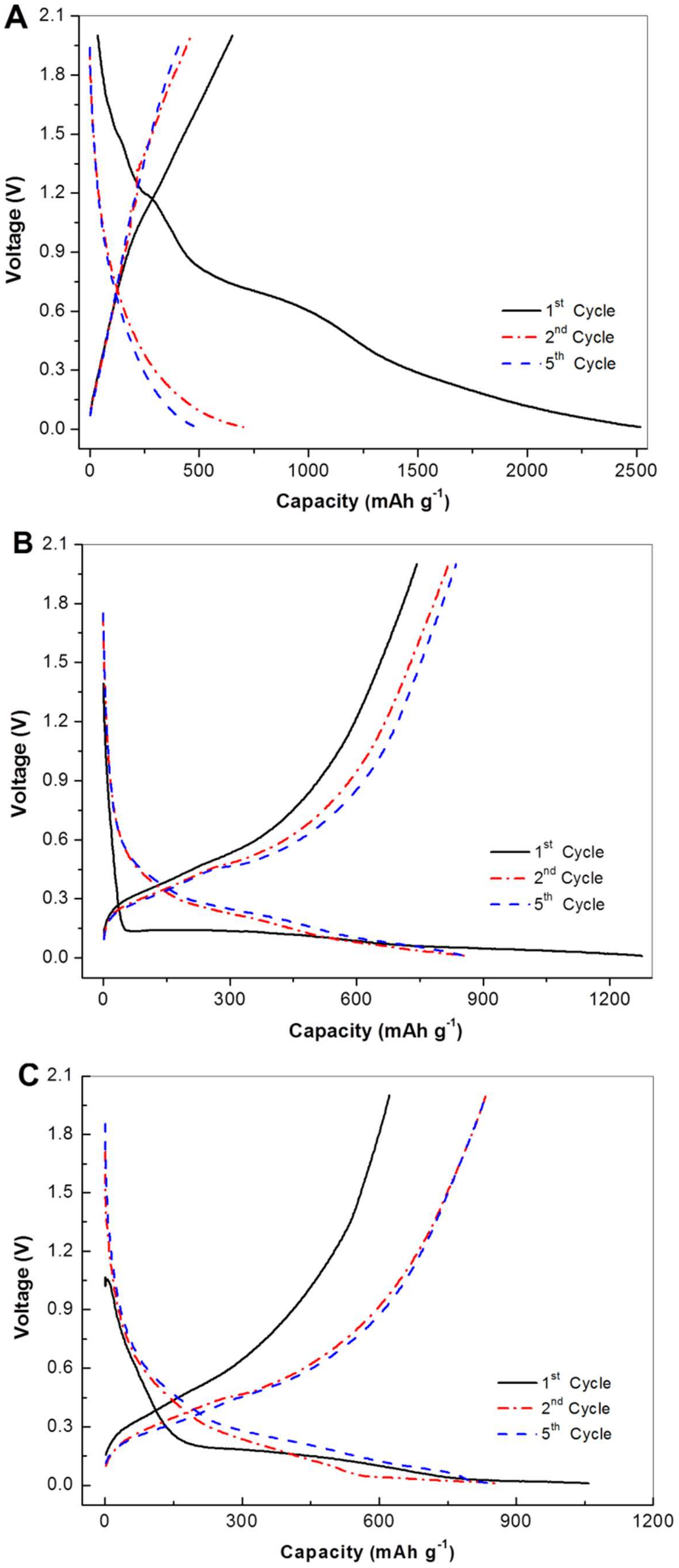

Figure 4.8 : Galvanostatic charge-discharge profiles of Si/C nanofibers (A), Si/SiO_2/C nanofibers (B), and CVD carbon-coated Si/SiO_2/C nanofibers (C).

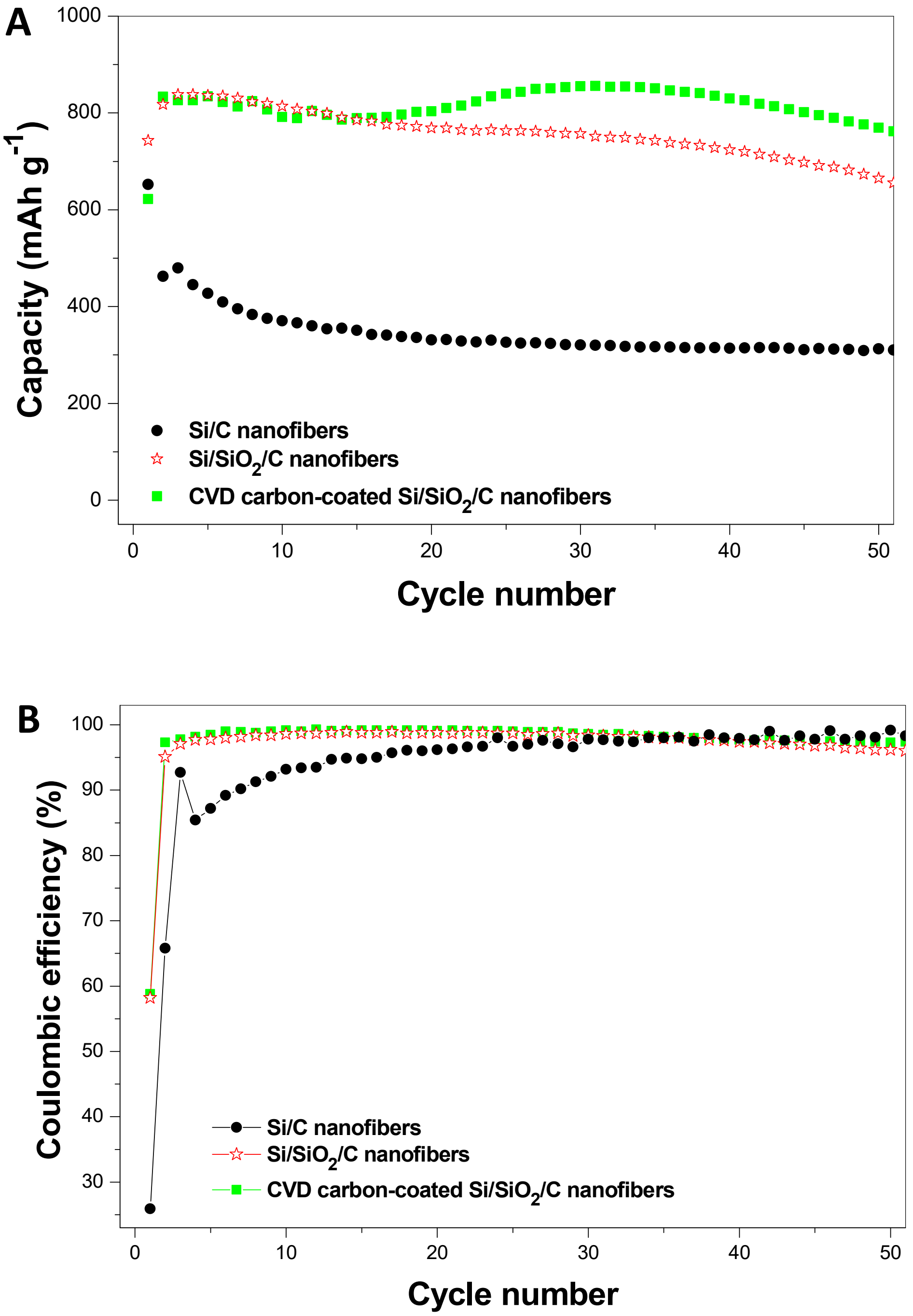

Figure 4.9 : Cycling performance (A) and coulombic efficiencies (B) of Si/C nanofibers, Si/SiO$_2$/C nanofibers, and CVD carbon-coated Si/SiO$_2$/C nanofibers.

From Figure 4.9, it was also seen that the cycling performance of CVD carbon-coated Si/SiO$_2$/C nanofibers was even better than that of Si/SiO$_2$/C nanofibers. The capacity retention and coulombic efficiency of CVD carbon-coated Si/SiO$_2$/C nanofibers was

91% and 97.4%, respectively, at the 50th cycle. The improved cycling performance was caused by the formation of CVD carbon coating, which confined the Si nanoparticles exposed on nanofiber surfaces and helped maintain the structural integrity of the electrode during the cycling process. On the other hand, the capacity of CVD carbon-coated Si/SiO_2/C nanofibers increased initially and then started to decrease. Similar capacity trend has been observed by other researchers for different carbon-confined Si/C structure materials [67, 82, 150], but few of them have pointed out the reason for the capacity increase during cycling. This unique behavior of CVD carbon-coated Si/SiO_2/C nanofibers could be explained by the carbon confinement of the agglomerated Si nanoparticles, which were mostly located on the nanofibers surfaces. Because of the large volume expansion during the lihiation process, Si nanoparticles underwent intense pulverization, but the pulverized Si particles were confined within CVD-carbon. Due to their smaller particle sizes, these pulverized Si particles would provide shorter lithium transfer distance and facilitate more active Si for lithium insertion, leading to increased capacity for CVD carbon-coated Si/SiO_2/C nanofibers. However, more work is needed to confirm this possible mechanism.

Among all three carbonized nanofibers, CVD carbon-coated Si/SiO_2/C nanofibers had the best cycling performance. The rate capability of CVD carbon-coated Si/SiO_2/C nanofibers was examined under different current densities (Figure 4.10). The highest charge capacity values under 100, 200, 400, and 800 mA g^{-1} were around 920, 820, 730, and 580 mAh g^{-1}, respectively. The coulombic efficiency remained relatively constant as the current density increased. After repeated cycles at higher current densities, the charge capacity values returned to 860 mAh g^{-1} when the current density was changed back to 100 mA g^{-1}. This charge capacity (860 mAh g^{-1}) was very close to initial charge capacity, indicating the good rate capability of CVD carbon-coated Si/SiO_2/C nanofibers.

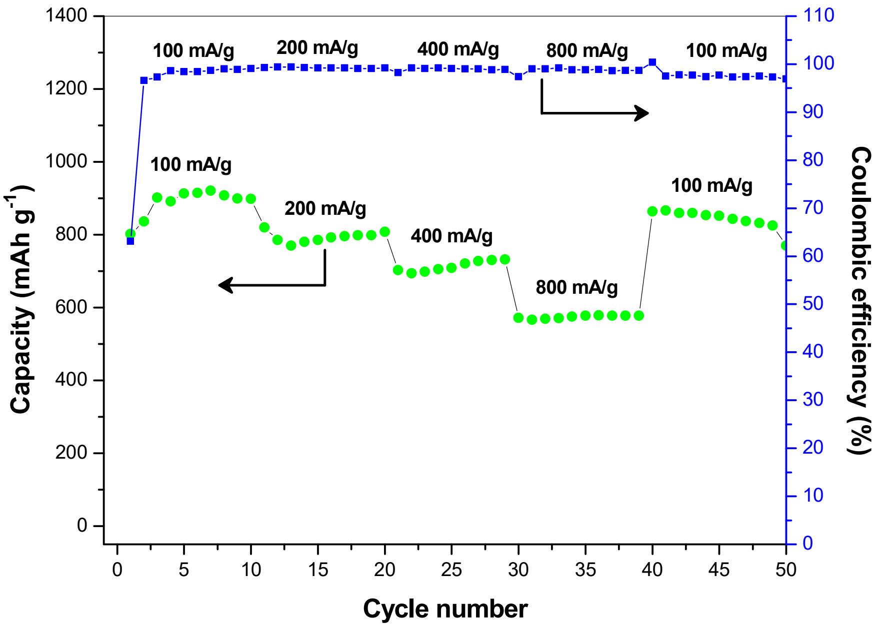

Figure 4.10 : Rate capability of CVD carbon-coated Si/SiO_2/C nanofibers cycled at different current densities.

4.4 Conclusions

Novel Si/SiO_2/C nanofiber composite anode materials were developed for lithium-ion batteries by the combination of Si nanoparticles, sol-gel TEOS solution, and aqueous PVA solution through simple electrospinning and subsequent heat treatment processes. To achieve good cycling performance, CVD amorphous carbon coating was applied onto Si/SiO_2/C nanofibers. It was found that the SiO_2 component of the nanofiber composites provided sufficient buffering function to accommodate the volume expansion of the Si nanoparticles during the repeated charging and discharging cycles. The CVD amorphous carbon coating helped maintain the Si nanoparticles within the nanofiber structure, resulting in improved cycling performance. Electrochemical performance results showed that among the composite anodes studied, CVD carbon-coated Si/SiO_2/C nanofiber composites exhibited the best performance with large capacity retention of 91% and high coulombic efficiency of 97.4% at the 50th cycle. This demonstrated that CVD carbon-coated Si/SiO_2/C nanofiber composites are promising anode material candidate for next-generation, high-energy lithium-ion batteries.

5. FLEXIBLE BINDER-FREE SILICON/SILICA/CARBON NANOFIBER COMPOSITES AS ANODE FOR LITHIUM-ION BATTERIES

5.1 Introduction

With recent improvements in technologies of portable and bendable electronic equipment such as rollup displays, implantable medical devices, active radio-frequency identification tags, and wearable devices, flexible battery technologies become critically important to meet their energy requirements [146, 167, 168]. Flexible batteries are not only crucial for portable devices, but also an important power source for future electric and hybrid electric vehicles [169]. Although different types of flexible batteries have been introduced, it is very important to fabricate highly-flexible energy storage devices with high mechanical strength and reasonable electrochemical performance similar to those of conventional energy storage devices [79, 170, 171]. Compared to other existing battery technologies, lithium-ion battery is considered as one of the most preferred rechargeable batteries in recent years because of its superior properties, including high energy density, durable cycle life and good power performance. The development of flexible, high-capacity electrode materials for high-energy lithium-ion batteries is crucial for technological improvements on portable electronics due to their advantages such as high mechanical strength, long cycle life, and high energy density [5, 147].

Most of the current commercial lithium-ion batteries use graphitic materials in the anode. However, graphitic anode materials cannot meet the ever-growing capacity requirements of future portable electronics because of their low specific capacity of 372 mAh g^{-1} [67, 69, 70]. Lithium storage capacities of alloy-type anodes, such as silicon (Si), tin, germanium, and their oxides etc., are much higher than those of commercially-used intercalation-type graphite anodes.

This chapter consists of the article below:

Dirican, M., Yildiz, O., Lu, Y., Fang, X., Jiang, H., Kizil, H., and Zhang, X. (2015). Flexible binder-free silicon/silica/carbon nanofiber composites as anode for lithium–ion batteries, *Electrochimica Acta, 169*, 52-60.

Among all alloy-type anodes, Si gives the highest theoretical capacity of 4200 mAh g^{-1}, making it the most promising candidate for next-generation high-energy lithium-ion batteries [71, 72]. However, similar to other alloy-type anode materials, the insertion of lithium ions into Si during cycling causes high volumetric change (up to 400%), which results in intense pulverization of active Si material and significant loss of electrical contact between Si and carbon conductor [73-75]. These drawbacks bring together the severe capacity fading of Si-based anodes during repetitive lithitation and delithitation processes [150]. Reducing the size of Si into the nanoscale range and dispersing it into carbon structures are some of the proposed effective methods for alleviating the volumetric change problem of Si-based anodes. Nano-sized Si/carbon (Si/C) composite anodes can potentially combine the advantageous properties of Si (high capacity) and carbon (excellent electronic conductivity and structural stability) [77, 172].

Most of the reported Si/C composite anodes are not suitable to for direct use in flexible lithium-ion batteries without adding electronically inactive materials such as polymer binder, conducting agent, and copper current collector [75]. The addition of these inactive materials considerably reduces the overall energy density of the battery. On the other hand, in a binder-free electrode design, the entire electrode structure is composed of electrochemically active materials, leading to higher useful electrode capacity. In this study, we report a novel binder-free, free-standing, and flexible silicon/silica/carbon ($Si/SiO_2/C$) nanofiber composite anode for lithium-ion batteries by the electrospinning and carbonization of a solution composed of Si nanoparticles, sol-gel tetraethyl orthosilicate (TEOS) solution, and polyacrylonitrile (PAN) polymer in *N,N*-dimethylformamide as the solvent. PAN can be converted to the carbon nanofiber matrix during carbonization while TEOS is the starting material for making SiO_2 structure [150, 154]. To improve the interfacial stability and cycling performance, the resultant $Si/SiO_2/C$ nanofibers can be coated with an amorphous carbon layer by the chemical vapor deposition (CVD) technique. These CVD carbon-coated flexible $Si/SiO_2/C$ nanofiber composite anode are expected to have excellent overall performance including high capacity, good cycling stability, and high coulombic efficiency because nanoscale CVD carbon coating enhances the carbon confinement of Si nanoparticles exposed on nanofiber surfaces and supports more stable SEI formation by preventing direct contact of the electrolyte with the active Si material.

5.2 Experimental

5.2.1 Nanofiber preparation

Tetraethyl orthosilicate (TEOS, 99%), polyacrylonitrile (PAN, M_W = 150,000 g/mol), and *N,N*-dimethylformamide (DMF), hydrochloric acid (HCl, 37%) were purchased from Sigma-Aldrich. Si nanoparticles (diameter: 30-50 nm) were purchased from Nanostructures & Amorphous Materials, Incorporated. All chemicals were used without further purification.

PAN solution (10%) in DMF was prepared at 60 °C and mechanically stirred for 24 h. TEOS solution (20%) was prepared by dissolving TEOS in DMF, followed by adding HCl (37%). In this solution, TEOS was used as silica precursor while HCl was added to catalyze the sol-gel transition process. During that process, sol-gel silica solution was formed by hydrolysis and condensation reactions between TEOS, solvent DMF and catalyst HCl [154, 155]. Because of the precipitation of PAN in ethanol, TEOS solution was prepared with DMF instead of using ethanol, since DMF was already reported as an effective solvent to stimulate the polymerization rate during sol-gel process [173]. The TEOS solution was stirred at room temperature for 3 h and was then gradually added to the PAN solution, followed by stirring for additional 3 h. The molar ratio of the components in the mixed TEOS/PAN solution was TEOS:PAN:DMF:HCl = 1:0.00275:62.14:0.04. Si nanoparticles (20 wt. % with respect to PAN) were added into the as-prepared TEOS/PAN solution and stirred at room temperature for 24 h, followed by ultrasonic treatment for 1 h to obtain a homogenous dispersion. The as-prepared Si/SiO_2/PAN dispersion was then electrospun into nanofibers with a flow rate of 0.75 ml/h, a voltage of 16 kV, and a tip-to-collector distance of 25 cm.

Electrospun Si/SiO_2/PAN nanofibers were stabilized in air environment at 280 °C for 5.5 h with a heating rate of 5 °C min^{-1} and then carbonized at 700 °C for 2 h in argon atmosphere with a heating rate of 2 °C min^{-1}, during which PAN was pyrolyzed to carbon. The resultant Si/SiO_2/C nanofiber composite was coated with amorphous carbon by the CVD method using acetylene (C_2H_2) as the carbon precursor gas. CVD carbon coating was applied at 700 °C for 1 h with 600 sccm flow rate of acetylene while the system was settled at 20 torr. Figure 5.1 illustrates schematically the entire nanofiber fabrication approach.

For comparison, flexible SiO_2/C nanofibers and inflexible Si/C nanofibers were also prepared from TEOS/PAN/DMF solution and Si/PAN/DMF solution, respectively, using the same electrospinning and thermal treatment procedures.

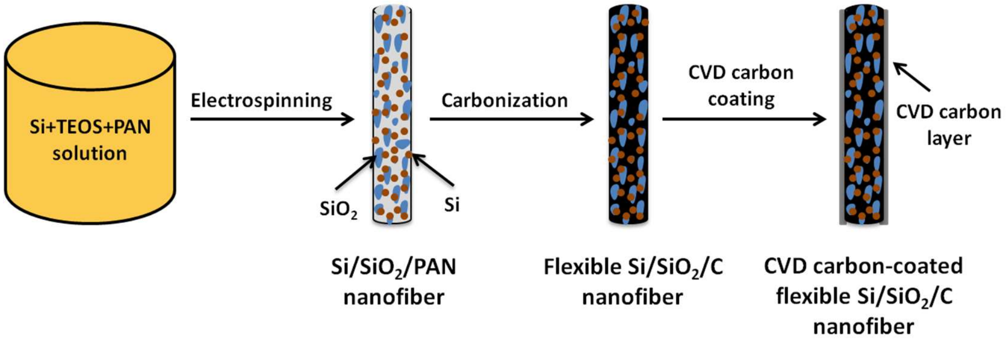

Figure 5.1 : Schematic illustration of the fabrication process of flexible Si/SiO_2/PAN nanofibers, flexible Si/SiO_2/C nanofibers, and CVD carbon-coated flexible Si/SiO_2/C nanofibers.

5.2.2 Structure characterization

The morphology of composite nanofibers was examined by field emission scanning electron microscope (FE-SEM, JEOL 6400F) and transmission electron microscope (TEM, JEOL JEM-2000FX). The structure of composite nanofibers was investigated by Fourier transform infrared spectroscopy (FTIR, Nicolet Nexus 470) and wide angle X-ray diffraction (WAXD, Rigaku Smartlab). Compositions of the flexible nanofiber composites were examined by TGA (Perkin-Elmer Pyris 1) and elemental analysis (Perkin Elmer 2400 Series II CHNS/O Elemental Analyzer).

5.2.3 Mechanical testing

For mechanical property characterization, both tensile and compressive tests were conducted. Tensile testing was operated by using a MTS-30G load frame at a crosshead speed of 2 mm min^{-1} and the gage length was 10 mm. For each sample, 5 specimens were tested and the specimen width was 10 mm. In compression tests, strip-shaped composite mat was clamped at the two ends and compressed using the same instrument and testing parameters as in the tensile tests.

5.2.4 Electrochemical evaluation

The electrochemical properties of composite nanofibers were tested using CR 2032-type coin cells. Flexible composite nanofibers formed free-standing, conductive nonwoven mats that were used directly as the working electrode without adding polymer binder or conductive agent. Before assembling the cells, the flexible composite nanofiber mats were folded back and forth and rolled up on a tweezers several times to examine the effect of the folding process on their electrochemical performances. Lithium ribbon (99.9%, Aldrich) was used as the counter electrode and Celgard 2400 membrane was used as the separator. The electrolyte consisted of a 1 M solution of $LiPF_6$ dissolved in ethylene carbonate (EC) + dimethyl carbonate (DMC) + diethyl carbonate (DEC) (1:1:1 by volume, MTI Corporation). Coin cells were assembled in a high-purity argon-filled glove box. The electrochemical performance was investigated by galvanostatic charge-discharge experiments at a constant current density of 100 mA g^{-1} (around C/10) with cut-off potentials between of 0.01 and 2.00 V on a LAND-CT 2001A battery test system.

5.3 Results and Discussion

5.3.1 Morphology and structure

Figure 5.1 shows schematically the fabrication approach of flexible Si/SiO_2/PAN nanofibers, flexible Si/SiO_2/C nanofibers, and CVD carbon-coated flexible Si/SiO_2/C nanofibers. Fabrication process of nanofiber electrodes composed of three steps: electrospinning of Si/TEOS/PAN solution into flexible Si/SiO_2/PAN nanofibers, carbonization of electrospun nanofibers to obtain flexible Si/SiO_2/C composite nanofibers, and CVD carbon coating of flexible Si/SiO_2/C nanofibers. Compositions of the flexible nanofiber composites were calculated based on the elemental analysis and TGA data (Figure 5.2). Results revealed that flexible Si/SiO_2/C nanofibers contained 19.8% Si, 27.1% SiO_2, and 53.1% C while CVD carbon-coated flexible Si/SiO_2/C nanofibers had 16.1% Si, 22.6% SiO_2, and 61.3% C. On the other hand, flexible SiO_2/C nanofibers was composed of 34.1% SiO_2 and 65.9% C. The carbon yield of PAN after the carbonization process was around 40%.

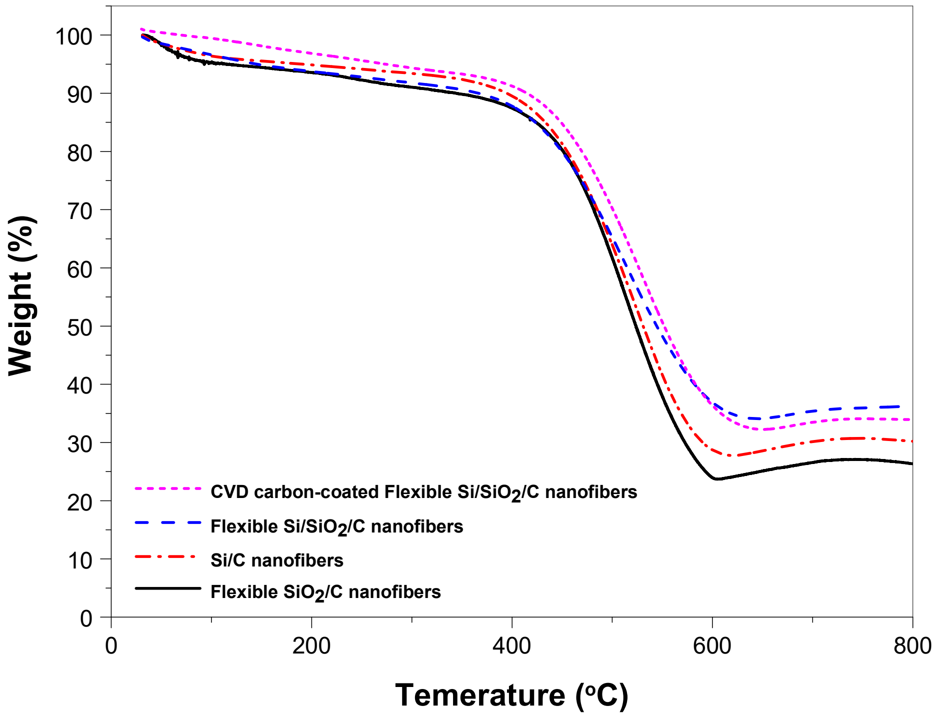

Figure 5.2 : Thermogravimetric analysis curves of flexible SiO_2/C nanofibers, inflexible Si/C nanofibers, flexible Si/SiO_2/C nanofibers, and CVD carbon-coated flexible Si/SiO_2/C nanofibers.

Photographs of an as-prepared flexible Si/SiO_2/C nanofiber mat in bended and folded forms are shown in Figure 5.3 to demonstrate its flexible feature. Composite nanofibers were bended and rolled up on a tweezers several times and it is seen that the free-standing Si/SiO_2/C nanofiber mat could endure repetitive cycles of bending and folding without any fracture and structural damage. For comparison, Si/C nanofibers, SiO_2/C nanofibers and CVD carbon-coated Si/SiO_2/C nanofibers were also examined in bended and folded forms. Si/C nanofibers were not flexible and were broken during the bending test. However, SiO_2/C nanofibers, Si/SiO_2/C nanofibers and CVD carbon-coated Si/SiO_2/C nanofibers were flexible. The introduction of SiO_2 throughout the carbon matrix significantly improved the flexibility of the composite nanofibers. The flexibility of SiO_2-containing nanofibers may be related to the phase separation between PAN polymer and the SiO_2 phase formed from the sol-gel TEOS solution [156, 166, 174]. The phase separation between PAN and SiO_2 might lead to the formation of free volume spaces, which could help absorb the bending force and contribute to the flexible nature of SiO_2-containing nanofibers. On the other hand, for Si/C nanofibers, Si nanoparticles were embedded into the carbon nanofiber matrix without the formation of adequate free volume spaces between carbon and Si nanoparticles. As a result, Si/C nanofibers were easily broken during the bending tests since the carbon matrix was highly brittle without the presence of adequate free volume spaces. This is a possible explanation of the flexible nature of composite nanofibers after the introduction of SiO_2, however, more work is still needed to fully understand the flexible nature of these composite nanofibers.

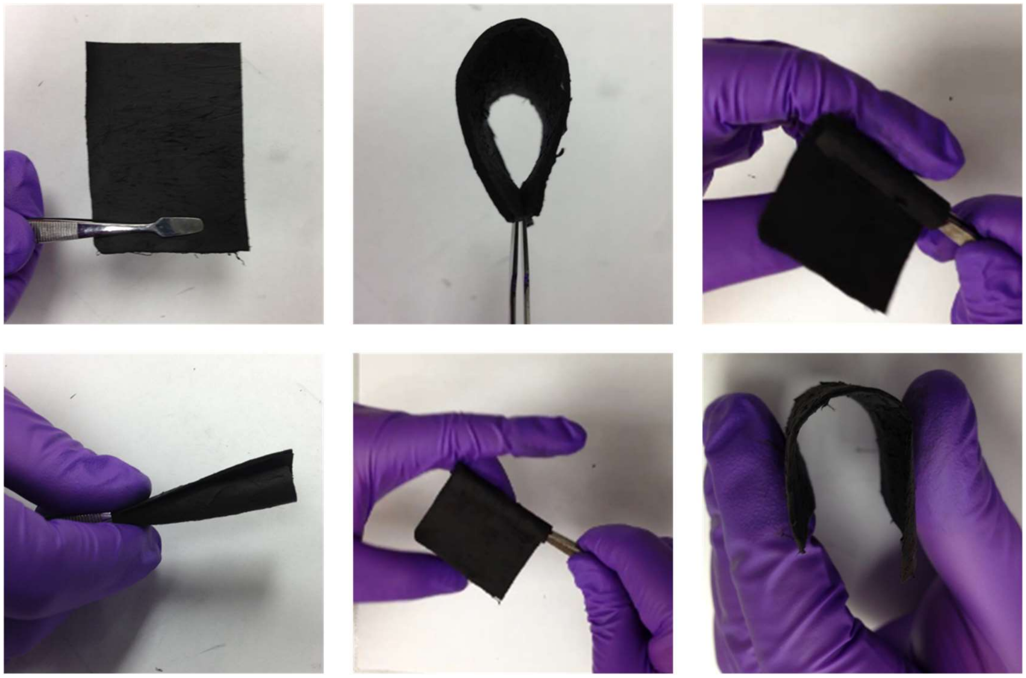

Figure 5.3 : Photographs of a flexible Si/SiO_2/C nanofiber mat. Free-standing, flexible Si/SiO_2/C nanofibers can be folded without any structural damage.

The morphology of SiO_2/C nanofibers, Si/C nanofibers, Si/SiO_2/C nanofibers, and CVD carbon-coated Si/SiO_2/C nanofibers was examined by using SEM, as shown in Figure 5.4. Continuous nanofibers were observed from the SEM image of flexible SiO_2/C nanofibers (Figure 5.4A). From Figures 5.4B, C and D, it is seen that the surface morphologies of flexible Si/SiO_2/C nanofibers, CVD carbon-coated flexible Si/SiO_2/C nanofibers, and inflexible Si/C nanofibers were similar. Si nanoparticles were dispersed throughout the carbon nanofiber matrices with some particles agglomerated on the nanofiber surfaces.

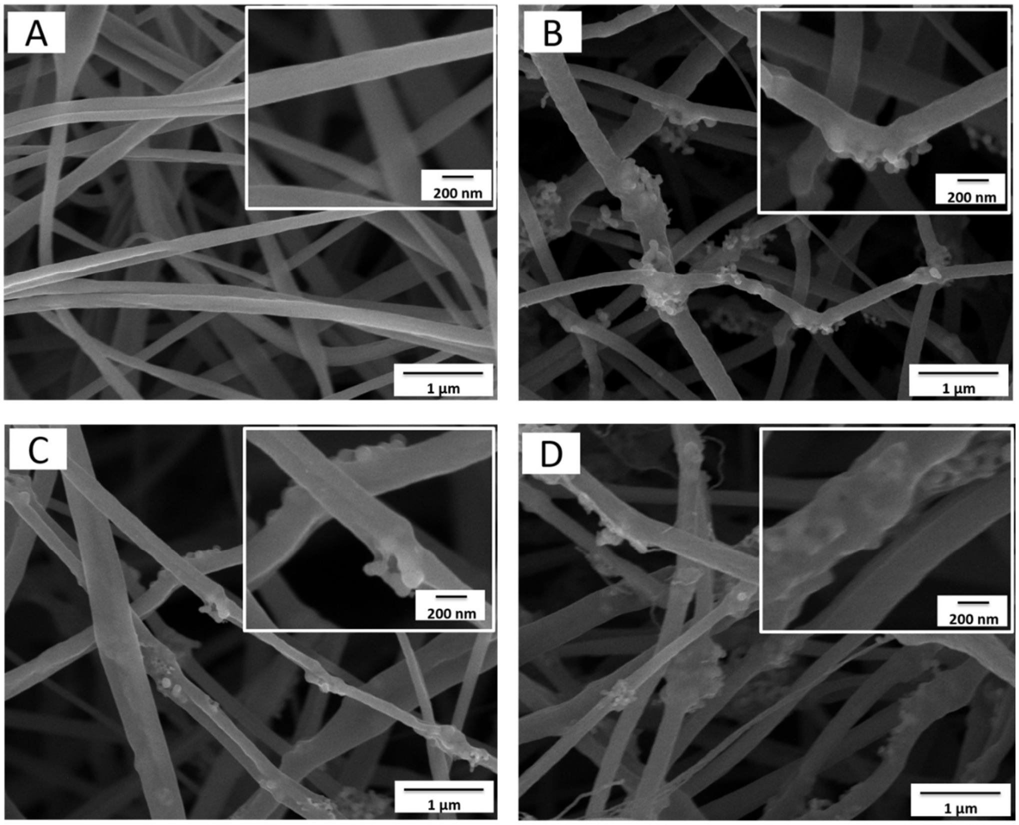

Figure 5.4 : SEM images of flexible SiO_2/C nanofibers (A), inflexible Si/C nanofibers (B), flexible Si/SiO_2/C nanofibers (C), and CVD carbon-coated flexible Si/SiO_2/C nanofibers (D).

Figure 5.5 shows TEM images of SiO_2/C nanofibers, Si/C nanofibers, Si/SiO_2/C nanofibers, and CVD carbon-coated Si/SiO_2/C nanofibers. From the TEM image of flexible SiO_2/C nanofibers (Figure 5.5A), it was observed that there were some darker areas along the fiber longitudinal direction, which were attributed to formed SiO_2 clusters. Similar SiO_2 clusters were observed from flexible Si/SiO_2/C nanofibers and CVD carbon-coated flexible Si/SiO_2/C nanofibers as well (Figures 5.5C and D). The introduction of Si nanoparticles changed the morphology of nanofiber composites. As shown in Figures 5.5B, C and D, the Si nanoparticles were not completely confined in the nanofiber matrix and some nanoparticles were agglomerated and located on nanofiber surfaces, which agreed with the SEM observation in Figure 5.4.

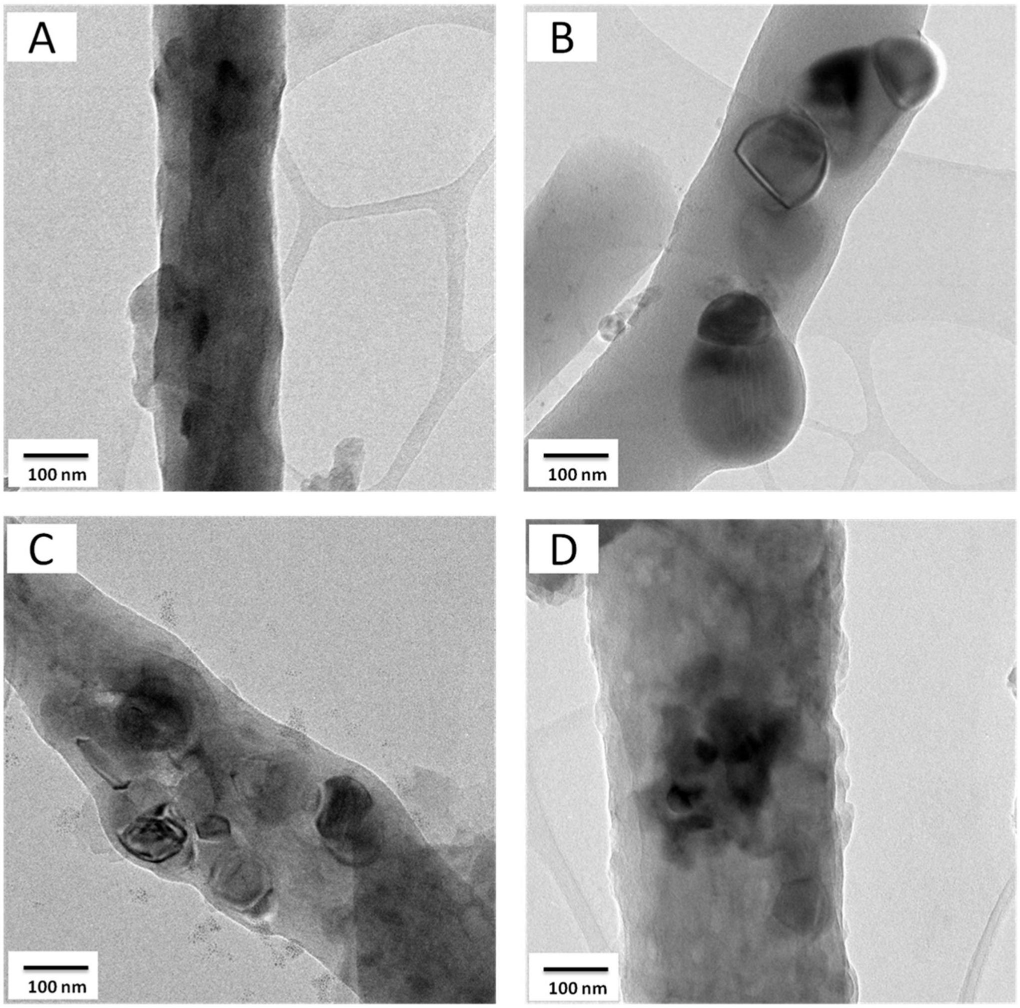

Figure 5.5 : TEM images of flexible SiO_2/C nanofibers (A), inflexible Si/C nanofibers (B), flexible Si/SiO_2/C nanofibers (C), and CVD carbon-coated flexible Si/SiO_2/C nanofibers (D).

High-magnification TEM image of a CVD carbon-coated flexible Si/SiO_2/C nanofiber (Figure 5.6) demonstrated the CVD amorphous carbon coating layer. It was observed that the surface of the flexible Si/SiO_2/C nanofiber was coated with an amorphous carbon layer of around 10 nm thick. This nanoscale carbon layer was very important for stable SEI formation on the surface of the active materials during the repetitive electrochemical reactions, especially for the Si nanoparticles agglomerated on the carbon nanofiber surface.

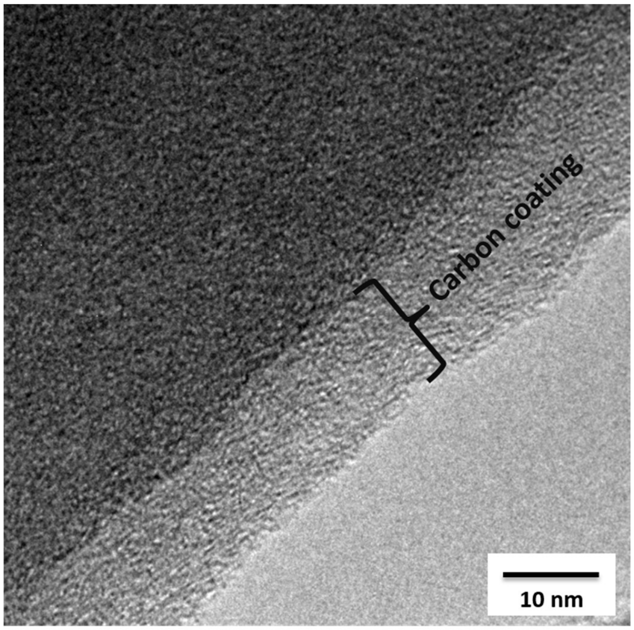

Figure 5.6 : High-magnification TEM image of a CVD carbon-coated flexible $Si/SiO_2/C$ nanofiber.

From the FTIR spectra of flexible $Si/SiO_2/PAN$ nanofibers, Si/C nanofibers, flexible SiO_2/C nanofibers, flexible $Si/SiO_2/C$ nanofibers, and CVD carbon-coated flexible $Si/SiO_2/C$ nanofibers (Figure 5.7) two characteristic peaks were indexed at around 1280 cm^{-1} and 1590 cm^{-1} for all carbonized nanofibers, which were attributed to the C–C and C=C stretch bonds, respectively [138]. These two peaks were not observed for flexible $Si/SiO_2/PAN$ nanofibers. After carbonization, the peaks indexed at around 1590 cm^{-1} for the flexible nanofibers (i.e., flexible SiO_2/C nanofibers, flexible $Si/SiO_2/C$ nanofibers, and CVD carbon-coated flexible $Si/SiO_2/C$ nanofibers) were weaker than that of inflexible Si/C nanofibers due to the relatively lower carbon content of those SiO_2-containing nanofibers. The peak intensities of carbonized composite nanofibers indexed at around 1280 cm^{-1} (C=C stretch bonds) were somewhat equal to those indexed at around 1590 cm^{-1} (C–C bonds) for the same nanofiber. FTIR spectra of all SiO_2 containing composite nanofibers (flexible $Si/SiO_2/PAN$ nanofibers, flexible SiO_2/C nanofibers, flexible $Si/SiO_2/C$ nanofibers, and CVD carbon-coated flexible $Si/SiO_2/C$ nanofibers) showed a characteristic SiO_2 peak at around 1100 cm^{-1}, corresponding to the symmetric stretching, asymmetrical stretching, and bending vibrations in Si-O-Si bonds [155]. Typical Si-O-Si peaks in the flexible SiO_2/C nanofibers, flexible $Si/SiO_2/C$ nanofibers, and CVD carbon-coated flexible $Si/SiO_2/C$ nanofibers confirmed the presence of silica even after the carbonization process. Since the inflexible Si/C nanofibers do not contain SiO_2, the peak at around 1100 cm^{-1} was not observed.

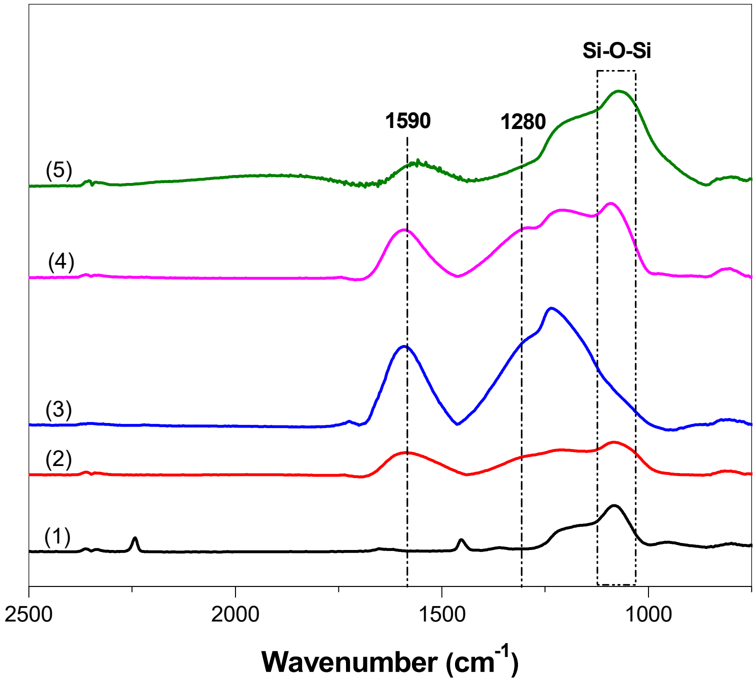

Figure 5.7 : FTIR spectra of flexible Si/SiO_2/PAN nanofibers (1), flexible SiO_2/C nanofibers (2), inflexible Si/C nanofibers (3), flexible Si/SiO_2/C nanofibers (4), and CVD carbon-coated flexible Si/SiO_2/C nanofibers (5).

The X-ray diffraction (XRD) patterns of inflexible Si/C nanofibers, flexible Si/SiO_2/C nanofibers, and CVD carbon-coated flexible Si/SiO_2/C nanofibers are shown in Figure 5.8. For all three nanofiber composites, similar diffraction peaks were indexed. Diffraction peaks at 2θ of about 29°, 47°, 56°, 69°, 76°, and 88° represent the (111), (220), (311), (400), (331), and (422) planes of Si crystals in nanofiber composites, respectively [158, 159]. In addition, as shown in Figure 5.8, all three nanofiber composites showed a broad and weak diffraction peak at around $2\theta = 25°$, which could be indexed as the (002) planes of disordered carbon structure, indicating the amorphous nature of the carbon nanofiber matrix [140, 160]. The carbon peak intensity of CVD carbon-coated flexible Si/SiO_2/C nanofibers was lower than those of inflexible Si/C nanofibers and flexible Si/SiO_2/C nanofibers probably because the carbon coating in the CVD carbon-coated flexible Si/SiO_2/C nanofibers is largely amorphous.

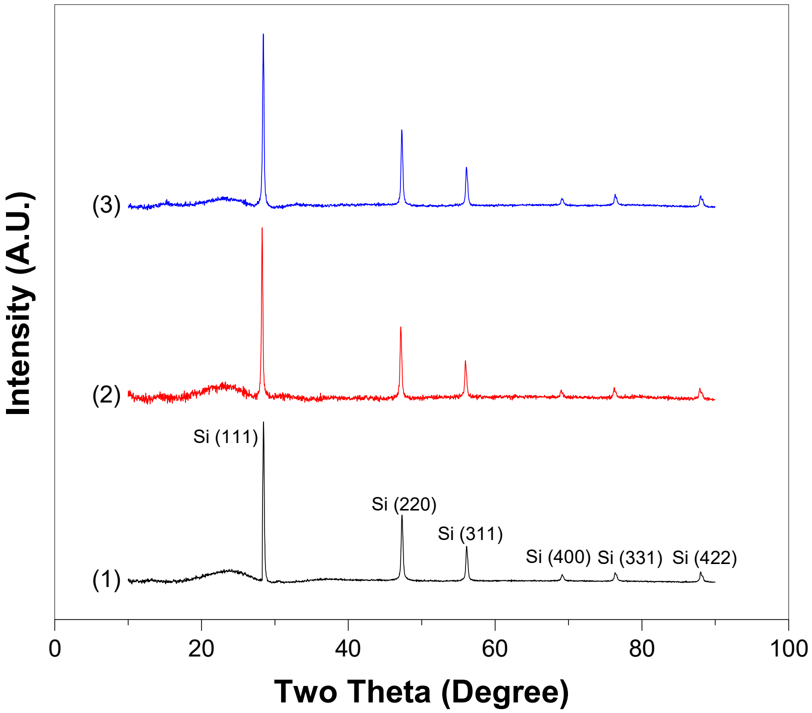

Figure 5.8 : WAXD patterns of inflexible Si/C nanofibers (1), flexible Si/SiO_2/C nanofibers (2), and CVD carbon-coated flexible Si/SiO_2/C nanofibers (3).

5.3.2 Mechanical properties

To further demonstrate the flexible nature of Si/SiO_2/C nanofibers, their mechanical properties were examined. Figure 5.9A compares the typical tensile stress-strain curves of flexible Si/SiO_2/C nanofibers and inflexible Si/C nanofibers. Firstly, the strain-at-break for the Si/C nanofibers (about 2.5%) was significantly less than that of flexible Si/SiO_2/C nanofibers (about 4.4%). While observing the fracture behavior of the inflexible Si/C nanofibers during tensile testing, it was noticed that a tiny crack appeared first and then propagated quickly, causing catastrophic fracture. By contrast, the crack on flexible Si/SiO_2/C nanofibers spread gradually which was able to effectively avoid the sudden breaking of the entire specimen. From Figure 5.9A, it is also seen that flexible Si/SiO_2/C nanofibers exhibited larger breaking strength than inflexible Si/C nanofibers (0.54 MPa vs. 0.43 MPa). Moreover, the Young's modulus of inflexible Si/C nanofibers (about 8 MPa) was obviously higher than that of the flexible Si/SiO_2/C nanofibers (about 5.5 MPa).

In compression tests, the strain-at-break was recording by simply observing the first visible crack on the sample and noting the strain magnitude simultaneously. For inflexible Si/C nanofibers, the first visible crack occurred at the strain magnitude of 16%, as shown in Figure 5.9B. In comparison, there was no crack observed on the flexible Si/SiO$_2$/C nanofiber sample even under a significantly higher strain of 80% (Figure 5.9C). After recovering from 80% strain, there was no obvious folding trace observed on the flexible Si/SiO$_2$/C nanofiber sample. These results demonstrated that Si/SiO$_2$/C nanofibers were mechanically durable and highly flexible.

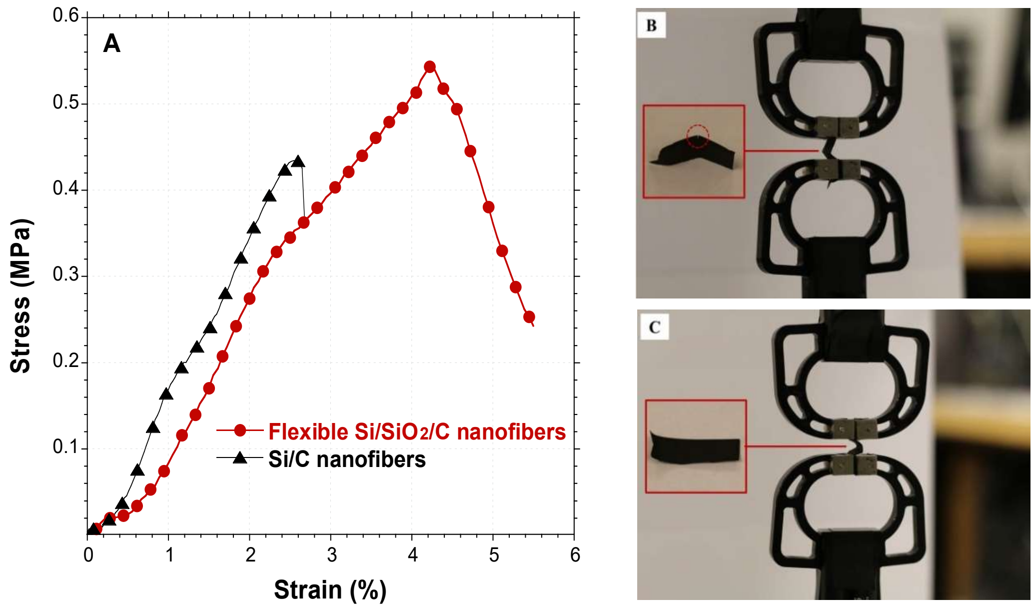

Figure 5.9 : Mechanical properties. (A) typical tensile stress-strain curves of flexible Si/SiO$_2$/C nanofibers and inflexible Si/C nanofibers; (B) photograph of inflexible Si/C nanofibers during compression test, inset shows the visible crack on the tested sample; (C) photograph of flexible Si/SiO$_2$/C nanofibers sample while compression test, inset shows undamaged sample after testing.

5.3.3 Electrochemical performance

Galvanostatic charge-discharge tests were conducted between 0.01 and 2.0 V at a constant current density of 100 mA g^{-1} to evaluate the electrochemical performance of the nanofiber composite anodes. The specific capacities of all electrodes were calculated based on the total mass of nanofiber composites by including Si, CNF, and carbon coating if any. Figure 5.10 shows the first, second, fifth and fiftieth cycle of the galvanostatic charge-discharge profiles of flexible Si/SiO$_2$/C nanofibers and CVD carbon-coated flexible Si/SiO$_2$/C nanofibers composites. For comparison, the profiles of inflexible Si/C nanofibers without the presence of SiO$_2$ are also shown. The first-cycle discharge capacities were 1327, 1206, and 1145 mAh g^{-1}, respectively, for inflexible Si/C nanofibers, flexible Si/SiO$_2$/C nanofibers, and CVD carbon-coated flexible Si/SiO_2/C nanofibers (Figure 5.10A). Because inflexible Si/C nanofibers were composed of only active Si and C without the inactive SiO_2 ingredient, the first-cycle discharge capacity of Si/C nanofibers was slightly higher than those of flexible Si/SiO_2/C nanofibers and CVD carbon-coated flexible Si/SiO_2/C nanofibers. For the inflexible Si/C nanofibers, the initial discharge and charge capacities reached 1327 and 944 mAh g^{-1}, respectively, with a coulombic efficiency of 71.1%. At the 5th cycle, the charge capacity reduced to 855 mAh g^{-1} with a capacity loss of 9.4% (Figure 5.10C). On the other hand, flexible Si/SiO_2/C nanofibers showed discharge and charge capacities of 1206 and 883 mAh g^{-1}, respectively, with a coulombic efficiency of 73.2% for the first cycle. The charge capacity of flexible Si/SiO_2/C nanofibers decreased to 815 mAh g^{-1} with a 7.7% capacity loss at the 5th cycle. Initial discharge and charge capacities of CVD carbon-coated flexible Si/SiO_2/C nanofibers were 1145 and 818 mAh g^{-1}, respectively, with a coulombic efficiency of 71.4%. At the 5th cycle, the charge capacity of CVD carbon-coated flexible Si/SiO_2/C nanofibers decreased to 778 mAh g^{-1} with a 4.9% capacity loss, which was the smallest capacity loss among all electrodes studied. At the 50th cycle, discharge capacities of inflexible Si/C nanofibers, flexible Si/SiO_2/C nanofibers, and CVD carbon-coated flexible Si/SiO_2/C nanofibers decreased to 600, 673, and 733 mAh g^{-1}, respectively (Figure 5.10D). As compared to the inflexible Si/C nanofibers, which does not contain SiO_2 in the structure, the voltage plateau under the curve of the electrolyte reduction/degradation stage (-0.7 V) was shortened for flexible Si/SiO_2/C nanofibers and CVD carbon-coated flexible Si/SiO_2/C nanofibers, indicating that less electrolyte participated in the formation of SEI due to the presence of SiO_2 in their structure [140]. From Figure 5.10, it is also seen that the overpotentials for SiO_2 containing composites (i.e., flexible Si/SiO_2/C nanofibers and CVD carbon-coated flexible Si/SiO_2/C nanofibers) at the initial cycles were higher than that of inflexible Si/C nanofibers. However, the overpotential for Si/C nanofibers increased significantly during cycling while those for SiO_2 containing composites did not exhibit apparent increase. As a result, the overpotentials of SiO_2 containing composites were smaller than that of inflexible Si/C nanofibers. Comparing the two SiO_2 containing composites, CVD carbon-coated flexible Si/SiO_2/C nanofibers had smaller overpotential than flexible Si/SiO_2/C nanofibers after 50 cycles, indicating that CVD coating further lowered overpotential growth with prolonged cycling, which could be associated with stable SEI growth.

This explains also a better capacity retention after 50 cycle and well correlates with improved coulombic efficiency.

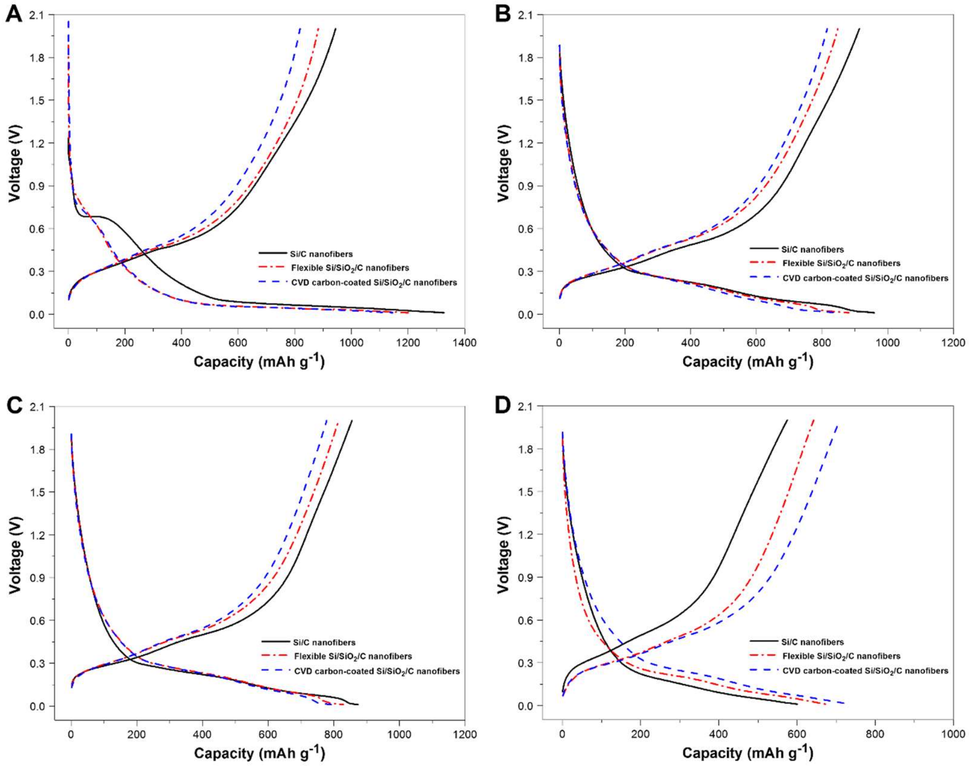

Figure 5.10 : Galvanostatic charge-discharge profiles of inflexible Si/C nanofibers, flexible Si/SiO_2/C nanofibers, and CVD carbon-coated flexible Si/SiO_2/C nanofibers for first (A), second (B), fifth (C), and fiftieth (D) cycles.

The cycling performance of inflexible Si/C nanofibers, flexible Si/SiO_2/C nanofibers, and CVD carbon-coated flexible Si/SiO_2/C nanofibers was compared in Figure 5.11. For comparison, the cycling performance of flexible SiO_2/C nanofibers is also shown in Figure 5.11 since it gives an estimate on how much of the capacity comes from carbon ingredients of the composite nanofibers. It is seen that at the 50th cycle, the capacity of flexible SiO_2/C nanofibers was around 222 mAh g^{-1}. Capacity retention and coulombic efficiency of inflexible Si/C nanofibers at the 50th cycle were around 60.9% and 95.7%, respectively. On the other hand, for flexible Si/SiO_2/C nanofibers, relatively stable cycling performance was achieved. At the 50th cycle, the capacity retention and coulombic efficiency of flexible Si/SiO_2/C nanofibers were around 72.8% and 95.4%, respectively. Compared to flexible Si/SiO_2/C nanofibers, inflexible Si/C nanofibers showed faster capacity decay in 50 cycles. Results demonstrated that the introduction of SiO_2 led to apparent improvement in the cycling performance for flexible $Si/SiO_2/C$ nanofibers. During the initial lithiation process, the amorphous SiO_2 structure might be reduced to Li_2O and Li_4SiO_4, which could help accommodate the volume expansion caused by the alloying of Si nanoparticles with Li, and thereby increased the cycling stability by minimizing the pulverization of the active Si material and the loss of electrical contact between Si nanoparticles and the carbon nanofiber matrix [157, 166]. From Figure 5.11, it is also seen that the cycling performance of flexible $Si/SiO_2/C$ nanofibers was further improved by CVD carbon-coating. The capacity retention and coulombic efficiency of CVD carbon-coated flexible $Si/SiO_2/C$ nanofibers was around 86.7% and 96.7%, respectively, at the 50th cycle. This result demonstrated that the nanoscale CVD carbon coating enhanced the carbon confinement of Si nanoparticles exposed on nanofiber surfaces and helped maintain the structural integrity of the electrode during the cycling process. The CVD carbon-coating layer also supported more stable SEI growth by preventing direct contact of the electrolyte with the active Si material. Similar effects of nanoscale carbon coating have been observed by Fu, et al., who obtained improved cycling stability for nanoscale CVD carbon-coated electrospun Si/C nanofiber composite anodes [150]. As discussed in the previous paragraph, the stable SEI growth on CVD carbon-coated flexible $Si/SiO_2/C$ nanofibers also resulted in lower overpotential growth with prolonged cycling.

The CVD carbon-coated flexible $Si/SiO_2/C$ nanofibers showed the best cycling performance among all the studied nanofiber composites. Therefore, this composite was further investigated for its rate capability under various current densities, as shown in Figure 5.12. It was observed that the charge capacities were around 893, 784, 599, and 436 mAh g^{-1}, respectively, at current densities of 100, 200, 400, and 800 mA g^{-1}. The coulombic efficiency remained relatively constant as the current density increased. The charge capacity reached 860 mAh g^{-1} when the current density returned to 100 mA g^{-1} after ongoing cycles at higher current densities. This charge capacity (860 mAh g^{-1}) was very close to initial charge capacity (893 mAh g^{-1}), demonstrating the good rate capability of CVD carbon-coated flexible $Si/SiO_2/C$ nanofibers.

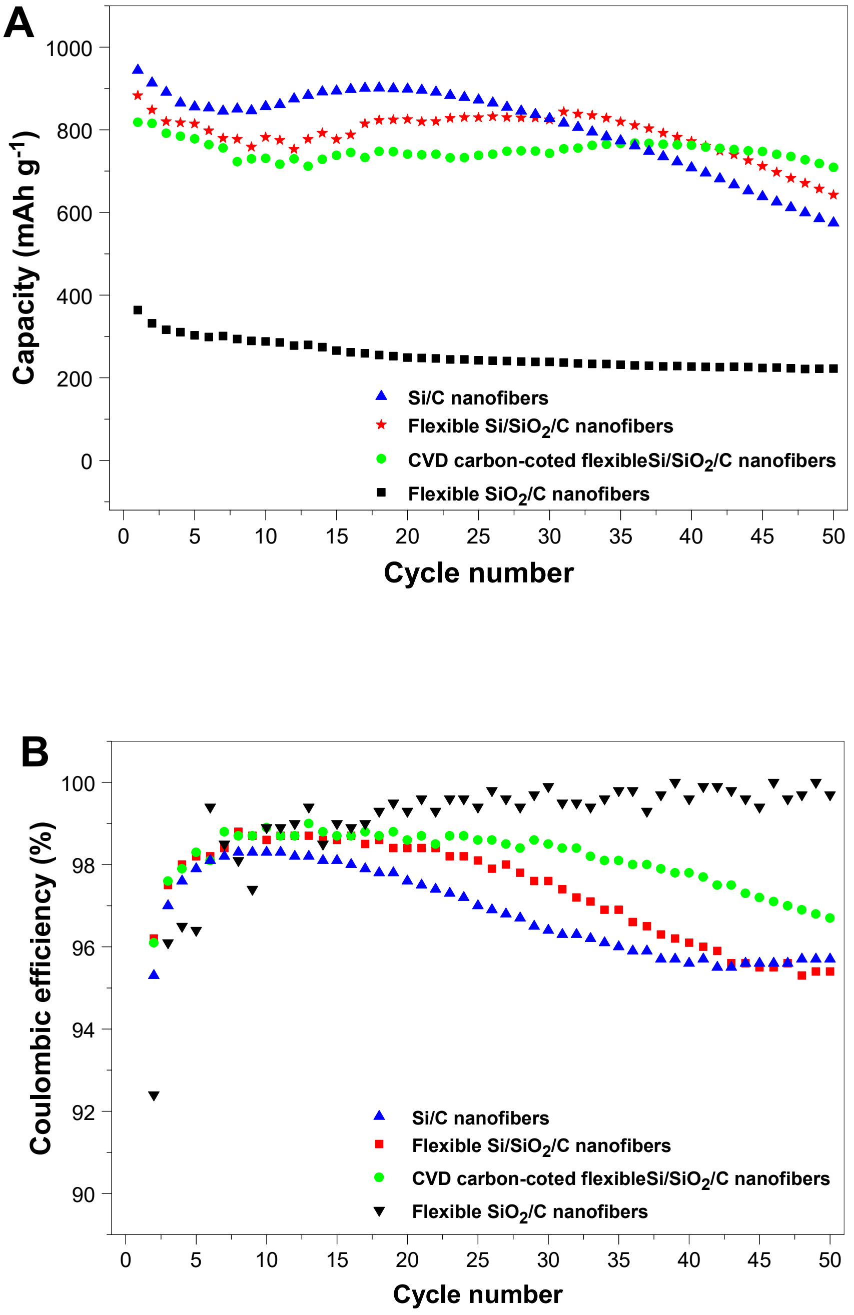

Figure 5.11 : Cycling performance (A) and coulombic efficiencies (B) of inflexible Si/C nanofibers, flexible Si/SiO$_2$/C nanofibers, CVD carbon-coated flexible Si/SiO$_2$/C nanofibers, and flexible SiO$_2$/C nanofibers.

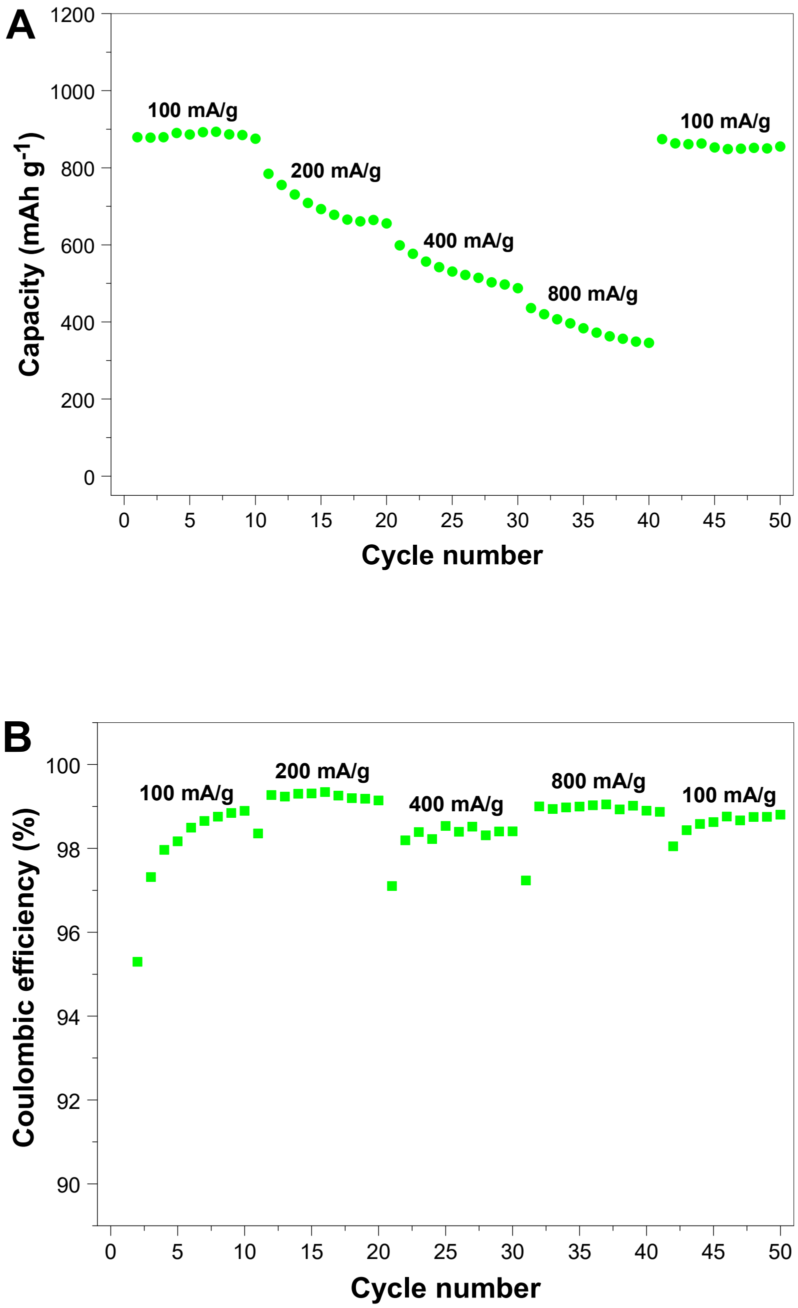

Figure 5.12 : Rate capability (A) and coulombic efficiency (B) of CVD carbon-coated flexible Si/SiO_2/C nanofibers cycled at different current densities.

5.4 Conclusions

Binder-free, flexible Si/SiO_2/C nanofiber composite anode materials were introduced by the combination of Si nanoparticles, sol-gel TEOS solution, and PAN/DMF solution through simple electrospinning and subsequent heat treatment processes.

Generating of the nanoscale SiO_2 structure throughout the carbon matrices led to a highly flexible composite nanofiber mat for using as binder-free anode material. Electrochemical results showed that, the SiO_2 component of the nanofiber composites provided sufficient buffering function to accommodate the volume expansion of the Si nanoparticles during the repeated charging and discharging cycles. To improve the long-term cycling performance, additional nanoscale carbon-coating of flexible $Si/SiO_2/C$ nanofibers was performed by CVD technique. CVD carbon coating helped maintain the Si nanoparticles within the nanofiber structure, resulting in further improved cycling performance. CVD coating also lowered the overpotential growth during prolonged cycling, which could be ascribed to stable SEI growth on CVD carbon-coated flexible $Si/SiO_2/C$ nanofibers. Electrochemical performance results showed that CVD carbon-coated flexible $Si/SiO_2/C$ nanofiber composites exhibited high capacity retention of 86.7% and high coulombic efficiency of 96.7%% at the 50th cycle. It is, therefore, demonstrated that CVD carbon-coated flexible $Si/SiO_2/C$ nanofiber composites are promising anode material candidate for next-generation flexible and high-energy lithium-ion batteries.

6. SiO_2-CONFINED SILICON/CARBON NANOFIBER COMPOSITES AS ANODE FOR LITHIUM-ION BATTERIES

6.1 Introduction

Among existing rechargeable battery technologies, lithium-ion batteries draw great attention in recent years because of their superior properties, including high energy density, durable cycle life and good power performance [67, 72]. With recent improvements in technologies of electric vehicles and portable electronic devices, development of high-capacity electrode materials for high-energy lithium-ion batteries becomes critically important to meet their energy requirements [146, 167, 168]. For most current commercial lithium-ion batteries, graphitic materials are used in the anode because of their low cost and long cycling performance. However, graphitic anode materials are not capable of meeting the ever-growing capacity requirements of future portable electronics and electric vehicles because of their low specific capacity of 372 mAh g^{-1} [70, 175]. On the other hand, lithium storage capacities of alloy-type anodes (e.g., silicon, tin, germanium, and their oxides) are much higher than those of commercially-used intercalation-type graphite anodes.

Among all alloy-type anodes, Si provides the highest theoretical specific capacity of 4200 mAh g^{-1}. Because of its ultra-high theoretical capacity, Si is considered as the most promising candidate for next-generation high-energy lithium-ion batteries.[71, 73] However, similar to other alloy-type anode materials, the insertion of lithium ions into Si during charge and discharge causes high volumetric change (up to 400%), which results in intense pulverization of active Si material and significant loss of electrical contact between Si particles and carbon conductor. In addition, high volume expansion and intense pulverization of active Si particles triggers extra electrolyte consumption on the fresh surface of Si, leading to unstable solid-electrolyte-interphase (SEI) film formation [74, 75].

This chapter consists of the article below:

Dirican, M., Lu, Y., Fu, K., Kizil, H., and Zhang, X. (2015). SiO_2-confined silicon/carbon nanofiber composites as an anode for lithium-ion batteries, *RSC Advances, 5*, 3744-3751.

Aforementioned drawbacks result in the severe capacity fading of Si-based anodes during repetitive lithiation and delithiation processes [150]. Reducing the size of Si particles into the nanoscale range and embedding them into carbon structures are some of the accepted effective methods for minimizing the volume expansion problem of Si-based anodes. Nano-sized Si/carbon (Si/C) composite anodes combine the advantageous properties of Si (high capacity) and carbon (excellent electronic conductivity and structural stability) [77, 172].

Carbon nanofibers are one of the best options for hosting active Si due to their high electronic conductivity, large surface area, and good electrochemical stability [140]. However, electrochemical performance results of the reported Si/C nanofiber composites are well below the expected performance due to direct exposure of Si nanoparticles with the electrolyte on the fiber surfaces which leads to heavy SEI formation [160, 176]. The exposed Si nanoparticles could also be detached from the nanofiber surfaces during the repetitive cycling processes. To eliminate the aforementioned problems, Fu, et al., and Dirican, et al., introduced an additional nanoscale disordered carbon layer onto the surface of Si@C nanofibers by chemical vapor deposition (CVD) technique to prevent direct exposure of the Si nanoparticles with the electrolyte solution and increase the mechanical bonding strength between the Si nanoparticles and carbon nanofiber matrix [140, 177]. With the additional protective layer, not only stable SEI is formed but also the detachment of Si nanoparticles from the nanofiber surfaces can be prevented. Confinement of the Si nanoparticles can also be ensured by using an easy and low-cost sol-gel method to form nanoscale amorphous SiO_2 coating on Si@C nanofibers. Similar to nanoscale carbon coating, nanoscale SiO_2 coating can lead to stable SEI formation on coated nanofiber surfaces and increased mechanical bonding between Si nanoparticles and carbon nanofiber matrix.

In this study, we report nanoscale SiO_2 coated Si@C (Si@C-SiO_2) nanofiber composites as high-energy anodes for lithium-ion batteries. We introduced a feasible method to improve the electrochemical performance of previously reported Si@C nanofiber composite electrodes. The main target of this study is to propose a simple, but effective approach for the confinement of Si nanoparticles inside the Si@C nanofiber composite electrodes. Si@C nanofibers were produced by simple electrospinning and subsequent heat treatment processes. The resultant Si@C nanofibers were coated with thin amorphous SiO_2 layers by using sol-gel TEOS solution to achieve further improvement on the cycling performance of the composite anodes. Nanoscale SiO_2 coating helped maintain the Si nanoparticles within the nanofiber structure and stabilize the SEI formation, resulting in improved cycling performance. Electrochemical performance results show that Si@C-SiO_2 nanofiber composite anodes exhibit capacity retention of 89.8% and coulombic efficiency of 97.2% after 50th cycles. Although better electrochemical performance (e.g., higher capacity retention or higher coulombic efficiency) has been reported in the literature,[77, 178] this work does present an easy and versatile approach for improving the electrochemical performance of previously reported Si@C nanofiber composite electrodes. Nevertheless, future study can be conducted to refine the structure of Si@C-SiO_2 nanofiber composite and further improve their electrochemical performance. In addition, the method used in this work can be applied to most of the previously reported Si/C based composite anodes to improve their performance.

6.2 Experimental

6.2.1 Nanofiber preparation

Tetraethyl orthosilicate (TEOS, 99%), polyacrylonitrile (PAN, M_W= 150,000 g/mol), *N,N*-dimethylformamide (DMF), ammonium hydroxide solution (NH_4OH, 28-30%), and ethanol were purchased from Sigma-Aldrich. Si nanoparticles (diameter: 30-50 nm) were purchased from Nanostructures & Amorphous Materials, Incorporated. All chemicals were used without further purification.

Figure 6.1 schematically illustrates the entire fabrication approach of electrospun Si@PAN nanofibers, Si@C nanofibers, and Si@C-SiO_2 nanofibers. For the preparation of Si@PAN nanofibers, PAN (8 wt%) was first dissolved in DMF at 60 ^{o}C and mechanically stirred for 24 h. Si nanoparticles (20 wt% with respect to PAN) were then added into the as-prepared PAN/DMF solution and stirred at room temperature for 24 h, followed by ultrasonic treatment for 1 h to obtain a homogenous dispersion. The as-prepared Si/PAN dispersion was then electrospun into Si@PAN nanofibers with a flow rate of 0.75 ml/h, a voltage of 16 kV, and a tip-to-collector distance of 25 cm. Si@C nanofiber composites were prepared from Si@PAN nanofibers through stabilization in air environment at 280 ^{o}C for 5.5 h with a heating rate of 5 °C min^{-1}, followed by carbonization at 700 °C for 2 h in argon atmosphere with a heating rate of 2 °C min^{-1}, during which PAN was pyrolyzed to carbon.

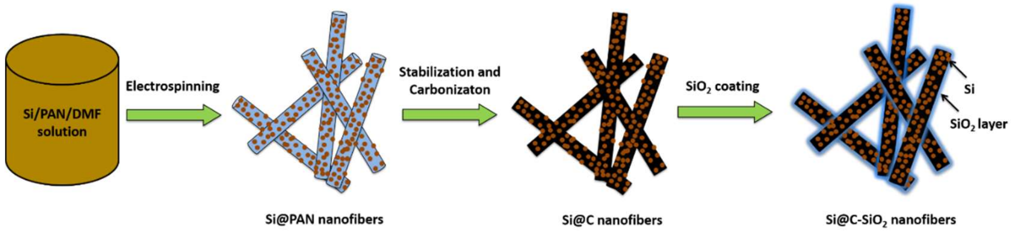

Figure 6.1 : Schematic illustration of the fabrication process of electrospun Si@PAN nanofibers, Si@C nanofibers, and Si@C-SiO$_2$ nanofibers.

For the preparation of Si@C-SiO$_2$ nanofiber composites, the as-prepared Si@C nanofibers were coated with nanoscale SiO$_2$ by using a sol-gel TEOS solution. The sol-gel TEOS solution was prepared by adding 3 ml ammonium hydroxide into a mixture of 125 ml ethanol and 30 ml water, followed by the addition of 2.4 g TEOS dropwise under vigorous stirring. The reaction was left at room temperature under vigorous stirring for 30 minutes. During the synthesis of Si@C-SiO$_2$ nanofiber composites, 100 mg Si@C nanofibers were immersed into the as-prepared sol-gel TEOS solution and treated for different duration times. Solution treatment time was varied from 0.5 h, 1 h to 2 h to investigate its effect on electrochemical performance. After solution treatment, the Si@C-SiO$_2$ nanofiber composites were first dried in vacuum oven and later washed with deionized water for three times.

6.2.2 Structure characterization

The morphology of nanofiber composites was examined by field emission scanning electron microscope (FE-SEM, FEI Verios 460 L) and scanning transmission electron microscope (STEM, JEOL 2000FX). The structure of composite nanofibers was investigated by Fourier transform infrared spectroscopy (FTIR, Nicolet Nexus 470), wide angle X-ray diffraction (WAXD, Rigaku Smartlab), and Renishaw Raman microscope. Compositions of the nanofiber composites were examined by elemental analysis (Perkin Elmer 2400 Series II CHNS/O Elemental Analyzer).

6.2.3 Electrochemical evaluation

The electrochemical properties of Si@C-SiO$_2$ nanofiber composites were tested using CR 2032-type coin cells. The working electrodes were prepared by mixing 70 wt% grounded nanofiber composites with 20 wt% carbon black and 10 wt% sodium alginate binder. The slurry of each sample was coated on copper foil substrates and vacuum-dried for 12 h at 80 °C. The average mass loading of the electrodes used in this study was 1.2 mg cm^{-2}. Lithium ribbon (99.9%, Aldrich) was used as the counter electrode and Celgard 2400 membrane was used as the separator. The electrolyte consisted of a 1 M solution of $LiPF_6$ dissolved in ethylene carbonate (EC) + dimethyl carbonate (DMC) + diethyl carbonate (DEC) (1:1:1 by volume, MTI Corporation). Coin cells were assembled in a high-purity argon-filled glove box. The electrochemical performance was investigated by galvanostatic charge-discharge experiments at a constant current density of 100 mA g^{-1} (around C/10) with cut-off potentials between of 0.01 and 2.00 V on a LAND-CT 2001A battery test system.

6.3 Results and Discussion

6.3.1 Morphology and structure

Figure 6.1 shows schematically the fabrication approach of Si@PAN nanofibers, Si@C nanofibers, and Si@C-SiO_2 nanofibers. Fabrication process of these nanofiber composites composed of three steps: electrospinning of Si/PAN solution into Si@PAN nanofibers, stabilization and carbonization of electrospun nanofibers to obtain Si@C nanofibers, and SiO_2 coating of Si@C nanofibers to form Si@C-SiO_2 nanofibers. Compositions of the nanofiber composites were calculated based on the elemental analysis data. Elemental analysis results revealed that Si@C nanofibers contained 24.05% Si, 10.30% SiO_2, and 65.65% C. The SiO_2 component of Si@C nanofibers might come from the surface oxidation of Si nanoparticles. The Si@C-SiO_2 nanofiber composite with 0.5 h coating time had 22.80% Si, 14.94% SiO_2, and 62.26% C. Here, the SiO_2 content was the sum of SiO_2 coating layer on the fiber surface and the oxidized SiO_2 on Si nanoparticles. With increase in coating time, the SiO_2 content increased. The Si@C-SiO_2 nanofiber composite with 1 h coating time was composed of 22.40% Si, 16.45% SiO_2, and 61.15% C, and the Si@C-SiO_2 nanofiber composite with 2 h coating time contained 21.98% Si, 17.97% SiO_2, and 60.05% C.

The morphology of Si@C nanofibers and Si@C-SiO_2 nanofibers with different coating times was examined by using SEM, as shown in Figure 6.2. Continuous nanofibers were observed from the SEM image of Si@C nanofibers (Figure 6.2A). From Figures 6.2B, C and D, it is seen that the surface morphologies of Si@C-SiO_2 nanofibers were similar to that of Si@C nanofibers. Si nanoparticles were dispersed throughout the carbon nanofiber matrices with some particles agglomerated on the nanofiber surfaces. From the SEM images of Si@C-SiO_2 nanofibers, the presence of SiO_2 coating layers was not apparent due to limited image resolution. To clearly observe the thin SiO_2 layers, TEM observation was carried out, as discussed below.

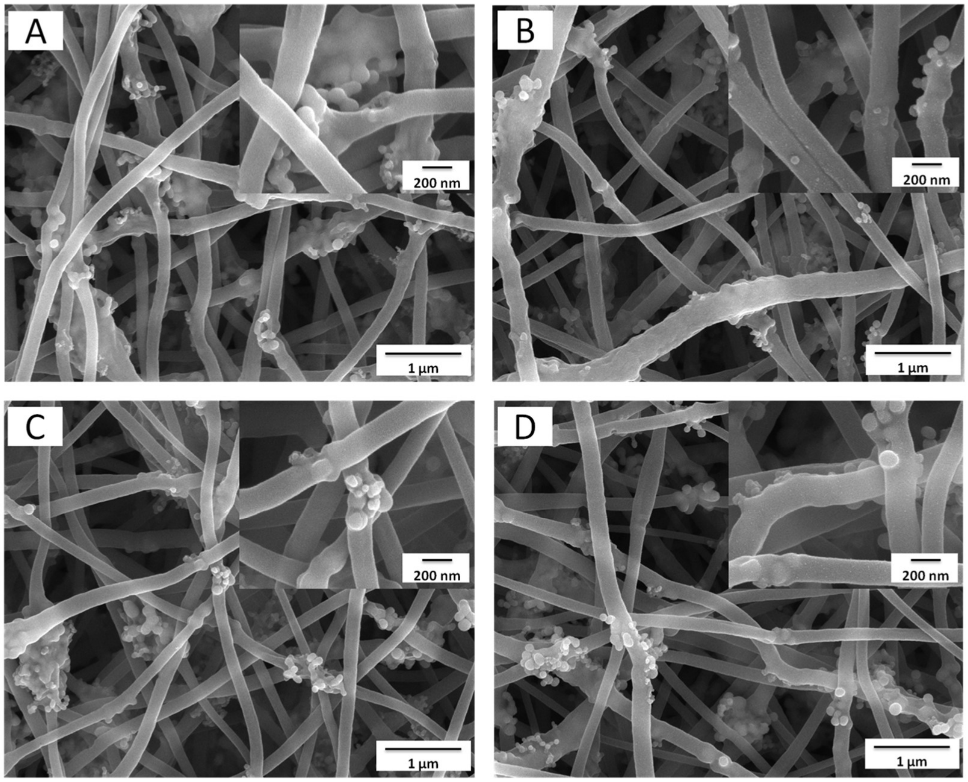

Figure 6.2 : SEM images of Si@C nanofiber composite (A) and Si@C-SiO_2 nanofiber composites with different coating times: (B) 0.5 h, (C) 1 h, and (D) 2h.

Figure 6.3 shows TEM images of Si/C and Si@C-SiO_2 nanofibers. TEM images show that for all four nanofiber composites, the Si nanoparticles were not completely confined in the nanofiber matrices and some nanoparticles were agglomerated and located on nanofiber surfaces, which agreed with the SEM observation in Figure 6.2. For the pristine Si@C nanofibers, no SiO_2 coating was observed on the exposed Si nanoparticles (Figure 6.3A). On the other hand, Si@C-SiO_2 nanofibers prepared with 0.5 h, 1 h, and 2 h SiO_2 coating times exhibited amorphous SiO_2 coatings on the Si nanoparticle surfaces (Figures 6.3B, C, and D).

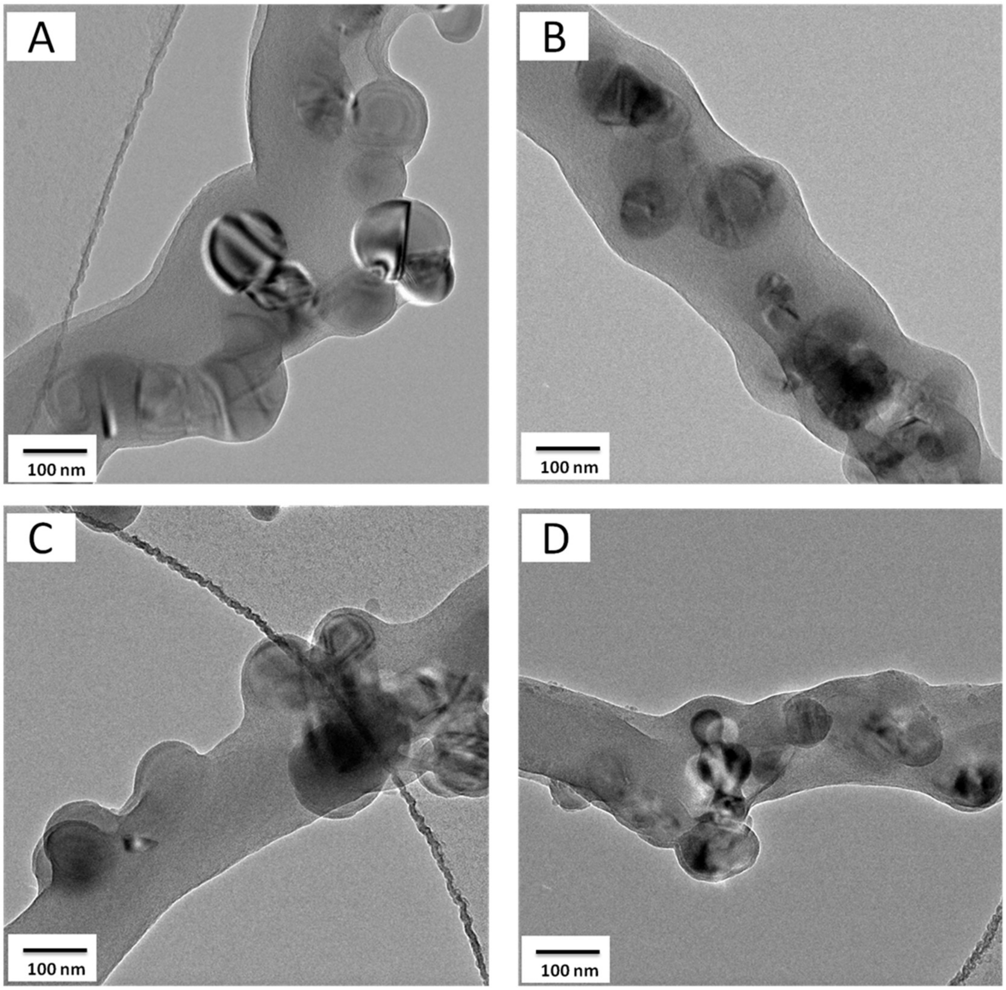

Figure 6.3 : TEM images of Si@C nanofiber composite (A) and Si@C-SiO_2 nanofiber composites with different coating times: (B) 0.5 h, (C) 1 h, and (D) 2h.

High-magnification TEM images of nanofiber composites are presented in Figure 6.4 to further illustrate the amorphous SiO_2 coating layers on the Si@C-SiO_2 nanofiber composites. For the pristine Si@C nanofiber composite, no SiO_2 coating was observed on the nanofiber surface (Figure 6.4A). However, nanoscale amorphous SiO_2 layers were clearly shown on the surfaces of Si@C-SiO_2 nanofiber composites. The thickness of the SiO_2 coating layers increased, on average, from 7 nm, 10 nm, to 13 nm, respectively, when the SiO_2 coating time increased from 0.5 h, 1 h, to 2 h. These nanoscale SiO_2 layers were important for stable SEI formation on the active materials during the repetitive electrode reactions, especially for the Si nanoparticles exposed on the carbon nanofiber surfaces.

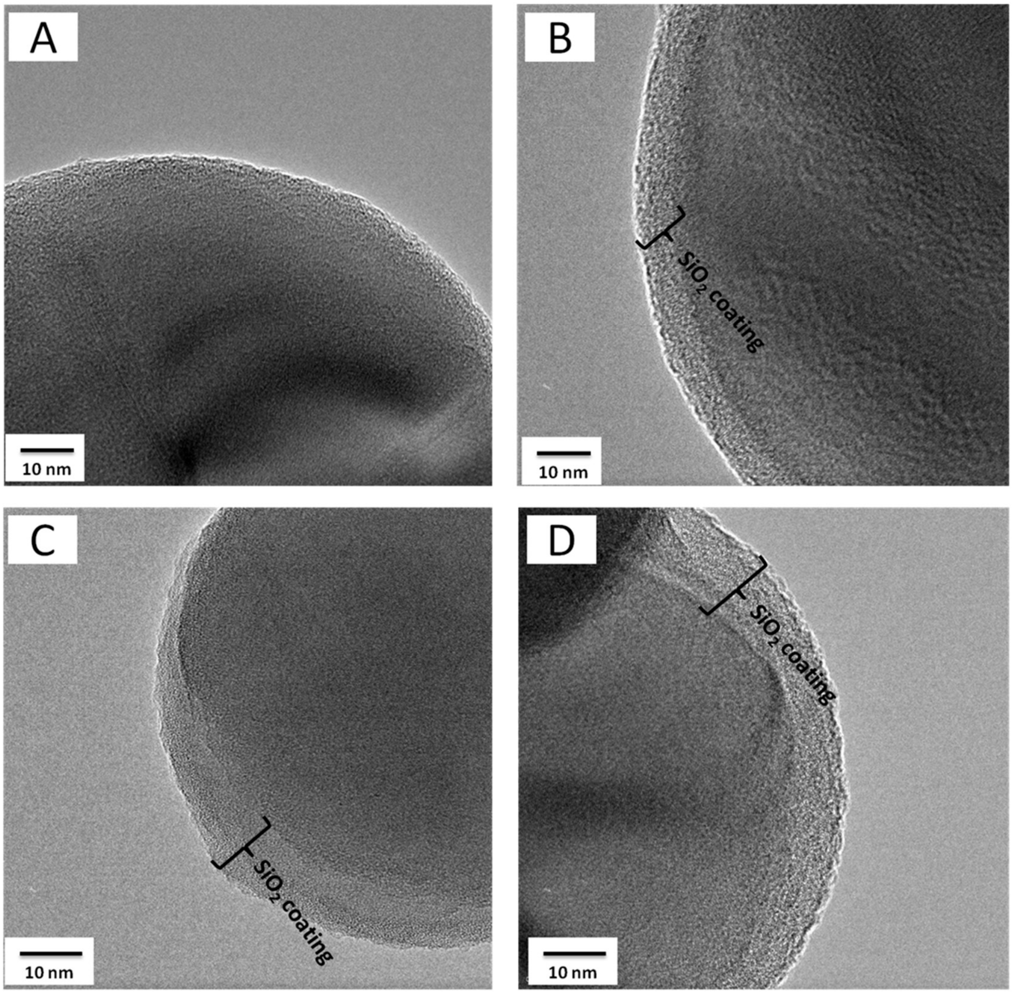

Figure 6.4 : High-magnification TEM images of Si@C nanofiber composite (A) and Si@C-SiO_2 nanofiber composites with different coating times: (B) 0.5 h, (C) 1 h, and (D) 2h.

Figure 6.5 shows the FTIR spectra of Si@C and Si@C-SiO_2 nanofiber composites. For all nanofiber composites, two characteristic peaks were indexed at around 1280 cm^{-1} and 1590 cm^{-1}, which were attributed to the C–C and C=C stretch bonds, respectively [138]. FTIR spectra of Si@C and Si@C-SiO_2 nanofiber composites also showed a characteristic SiO_2 side peak at around 1100 cm^{-1}, corresponding to the symmetric stretching, asymmetrical stretching, and bending vibrations in Si-O-Si bonds [155]. Since the pristine Si@C nanofiber composite do not have SiO_2 coating, the observed side peak at around 1100 cm^{-1} was weaker than those of Si@C-SiO_2 nanofiber composites. The presence of side peak at around 1100 cm^{-1} for Si@C nanofibers may be ascribed to the partial oxidation of Si nanoparticles.

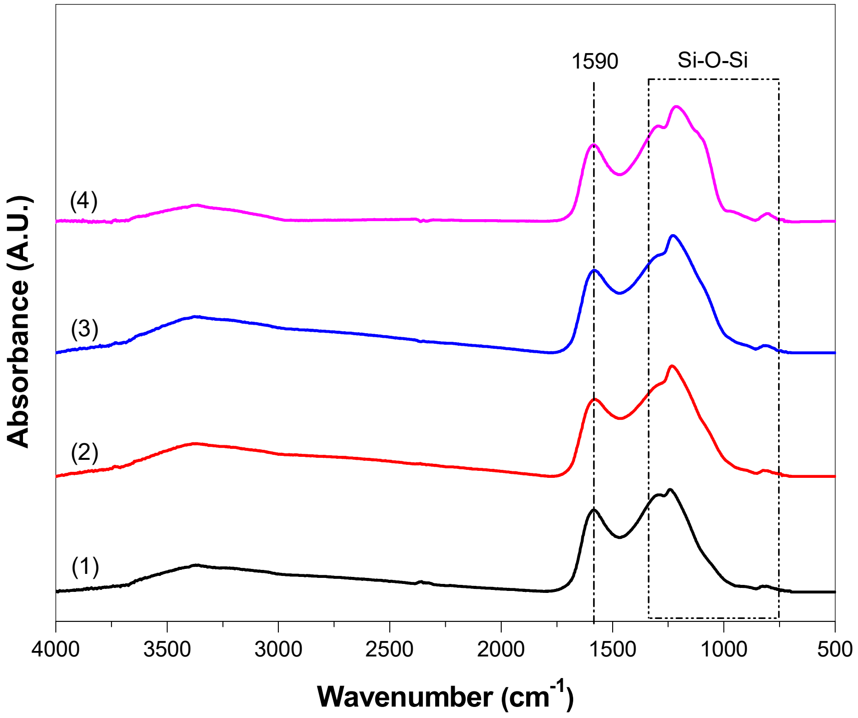

Figure 6.5 : TEM images of Si@C nanofiber composite (A) and Si@C-SiO$_2$ nanofiber composites with different coating times: (B) 0.5 h, (C) 1 h, and (D) 2h.

The X-ray diffraction (XRD) patterns of Si@C and Si@C-SiO$_2$ nanofiber composites are shown in Figure 6.6. For all nanofiber composites, similar diffraction peaks were indexed. Diffraction peaks at 2θ of about 29°, 47°, 56°, 69°, 76°, and 88° represented the (111), (220), (311), (400), (331), and (422) planes of Si crystals in carbon nanofiber composites, respectively [158, 159]. In addition, as shown in Figure 6.6, all nanofiber composites showed a broad and weak diffraction peak at around $2\theta = 25°$, which could be indexed as the (002) planes of disordered carbon structure, indicating the amorphous nature of the carbon nanofiber matrix [140, 160].

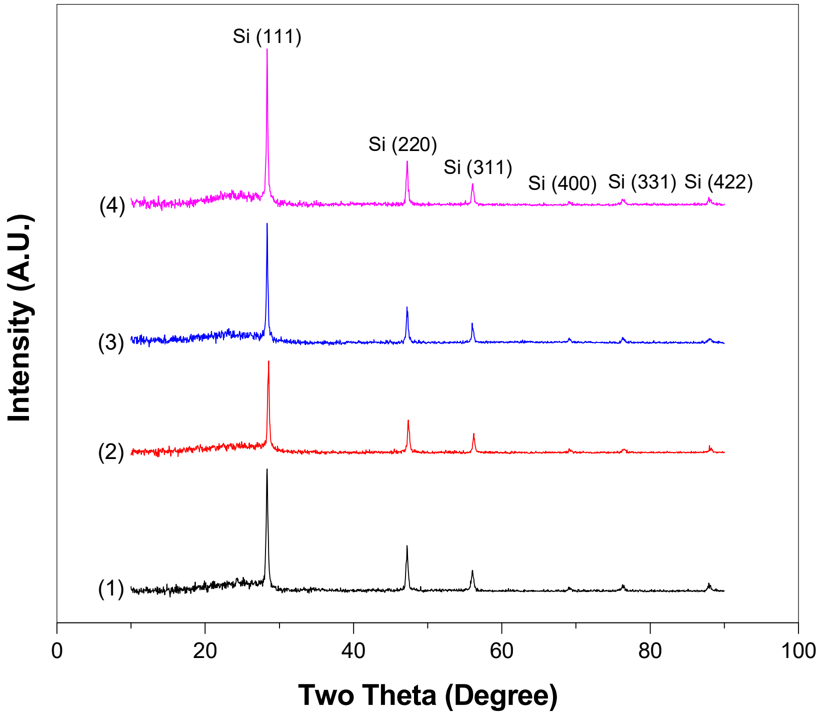

Figure 6.6 : WAXD patterns of Si@C nanofiber composite (1) and Si@C-SiO_2 nanofiber composites with different coating times: (2) 0.5 h, (3) 1 h, and (4) 2h.

The structural evolution of the nanofiber composites was also investigated by Raman spectroscopy. Figure 6.7 shows the Raman spectra of Si@C and Si@C-SiO_2 nanofiber composites. For all nanofiber composites, the characteristic carbon peaks of D-band (1360 cm^{-1}), indicating the disordered sp^2 phase, and G-band (1582 cm^{-1}), representing the in-plane stretching vibration mode of E_{2g} graphite, were indexed [81, 161]. From Figure 6.7, it was also seen that due to the presence of Si nanoparticles, these nanofiber composites exhibited a Si peak at around 522 cm^{-1}, which is a position for the transverse optical phonon [164]. In addition, Si@C-SiO_2 nanofiber composites with different SiO_2 coating times had a broad and weak peak at around 900 cm^{-1}, representing the SiO_2 component of the Si@C-SiO_2 nanofiber composites [165].

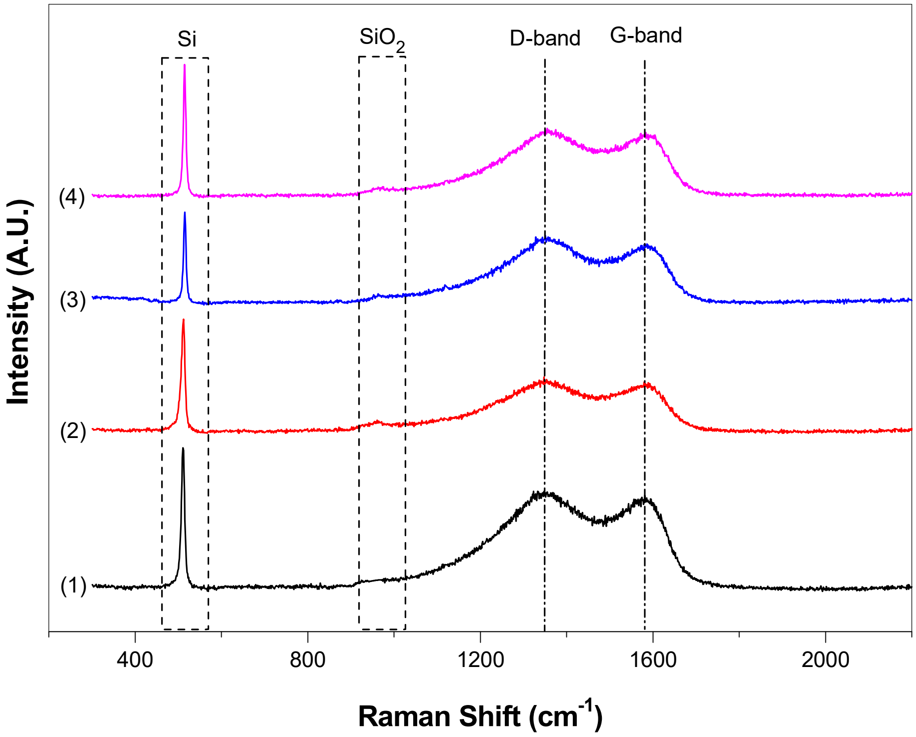

Figure 6.7 : Raman spectra of Si@C nanofiber composite (1) and Si@C-SiO_2 nanofiber composites with different coating times: (2) 0.5 h, (3) 1 h, and (4) 2h.

6.3.2 Electrochemical performance

Galvanostatic charge-discharge tests were conducted between 0.01 and 2.0 V at a constant current density of 100 mA g^{-1} to evaluate the electrochemical performance of the nanofiber composite anodes. The specific capacities of all nanofiber composite electrodes were calculated based on the total mass of nanofiber composites by including Si, C, and SiO_2 coating if any. Figure 6.8 represents the first, second and tenth cycle of the galvanostatic charge-discharge profiles of Si@C and Si@C-SiO_2 nanofiber composites. The first-cycle discharge capacities were 1506, 1570, 1567, and 1481 mAh g^{-1}, respectively, for Si@C nanofiber composite and Si@C-SiO_2 nanofiber composites with different coating times: 0.5 h, 1 h, and 2h. For the Si@C nanofiber composite, the initial discharge and charge capacities reached 1506 and 1138 mAh g^{-1}, respectively, with a coulombic efficiency of 75.6%. At the 10th cycle, the discharge and charge capacities changed to 1193 mAh g^{-1} and 1168 mAh g^{-1}, with a coulombic efficiency of 97.9% (Figure 6.8A). On the other hand, the initial discharge and charge capacities of Si@C-SiO_2 nanofiber composite with 0.5 h coating time were 1570 and 1222 mAh g^{-1}, respectively, with a coulombic efficiency of 77.8%. At the 10th cycle, the discharge and charge capacities of Si@C-SiO_2 nanofiber composite with 0.5 h coating time reduced to 1181 mAh g^{-1} and 1157 mAh g^{-1}, with a coulombic efficiency of 98.0% (Figure 6.8B). Initial charge and discharge capacities of Si@C-SiO_2 nanofiber composite with 1 h coating time were 1567 and 1215 mAh g^{-1}, respectively, with a coulombic efficiency of 77.5%. At the 10th cycle, the discharge and charge capacities of Si@C-SiO_2 nanofiber composite with 1 h coating time reduced to 1078 mAh g^{-1} and 1058 mAh g^{-1}, with a coulombic efficiency of 98.2% (Figure 6.8C). For the Si@C-SiO_2 nanofiber composite with 2 h coating time, the initial discharge and charge capacities reached 1481 and 1183 mAh g^{-1}, respectively, with a coulombic efficiency of 79.8%. At the 10th cycle, the discharge and charge capacities reduced to 993 mAh g^{-1} and 957 mAh g^{-1}, with a coulombic efficiency of 96.3% (Figure 6.8D). These results show that for both first and tenth cycles, the coulombic efficiencies of Si@C-SiO_2 nanofiber composites with 0.5 and 1 h coating times were better than those of Si@C nanofiber composite.

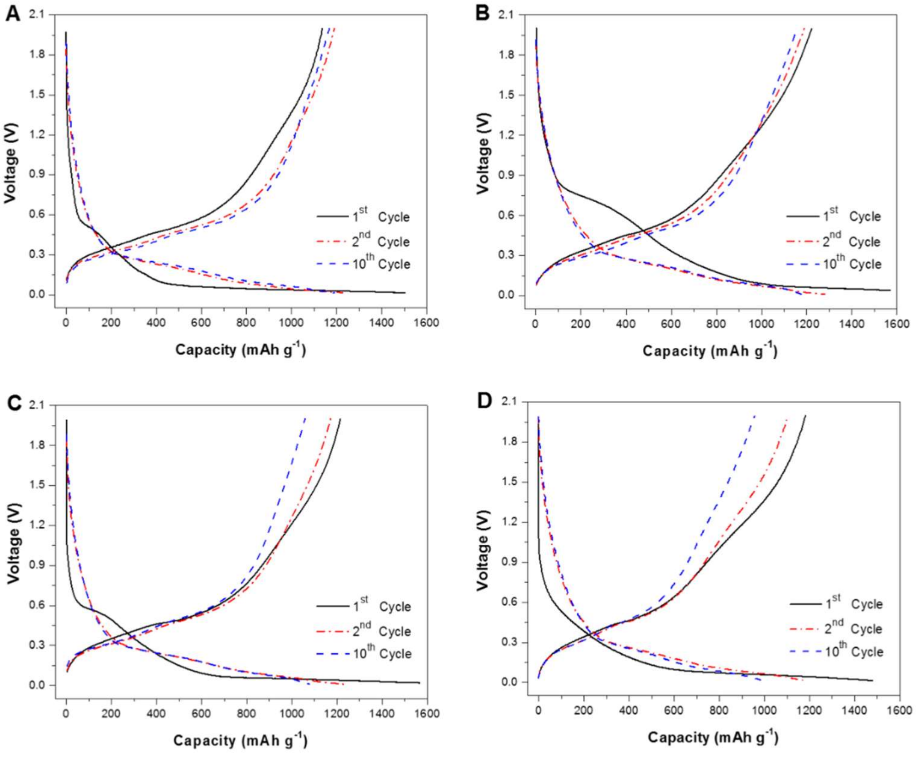

Figure 6.8 : Galvanostatic charge-discharge profiles of Si@C nanofiber composite (A) and Si@C-SiO_2 nanofiber composites with different coating times: (B) 0.5 h, (C) 1 h, and (D) 2h.

From Figure 6.8, it is also seen that there are two voltage plateaus, indexed at 0.7 V and 0.2 V, respectively, in the first-cycle discharge curve of Si@C-SiO_2 nanofiber composites. The plateau at 0.7 V was associated with the electrolyte decomposition and SEI formation while the plateau at 0.2 V was ascribed to electrochemical reactions between lithium ions and the SiO_2 ingredient of the composite nanofibers. During the initial lithiation process, SiO_2 might be reduced to electrochemically inactive Li_2O and Li_4SiO_4 [157, 166]. On the other hand, without the presence of SiO_2, the Si@C nanofiber composite did not exhibit the plateau at 0.2 V. When comparing the charge-discharge profiles of Si@C-SiO_2 composites with different coating times, it can be found that the voltage plateau under the curve of the electrolyte reduction/degradation stage at 0.7 V was shortened with increasing SiO_2 coating time, indicating that less electrolyte participated in the formation of SEI due to the presence of SiO_2 coating on the nanofiber surface [140].

The cycling performance of Si@C and Si@C-SiO_2 nanofiber composites was compared in Figure 6.9. Capacity retention and coulombic efficiency of the Si/C nanofiber composite at the 50th cycle were around 42.5% and 95.9%, respectively, indicating unstable cycling behavior. On the other hand, relatively stable cycling performance was achieved for the Si@C-SiO_2 nanofiber composite with 0.5 h coating time. At the 50th cycle, the capacity retention and coulombic efficiency of Si@C-SiO_2 nanofiber composite with 0.5 h coating time were around 89.8% and 97.2%, respectively. Compared to Si@C nanofiber composite, Si@C-SiO_2 nanofiber composite with 0.5 h coating time showed much slower capacity decay in 50 cycles. This result demonstrated that the nanoscale SiO_2 coating enhanced the confinement of Si nanoparticles on nanofiber surfaces and helped maintain the structural integrity of the electrode during the cycling process. Furthermore, during the initial lithiation process, the amorphous SiO_2 structure might be reduced to Li_2O and Li_4SiO_4, which could help accommodate the volume expansion caused by the alloying of Si nanoparticles with Li, and thereby increased the cycling stability by minimizing the pulverization of the active Si material and the loss of electrical contact between Si nanoparticles and the carbon nanofiber matrix [157, 166]. SiO_2 coating layer also supported more stable SEI formation by preventing direct contact of the electrolyte with the active Si material. Similar effects of nanoscale SiO_2 coating have been reported by Wu, et al., who obtained improved cycling stability for ion-permeable nanoscale SiO_2 surrounded silicon nanotube anodes [84].

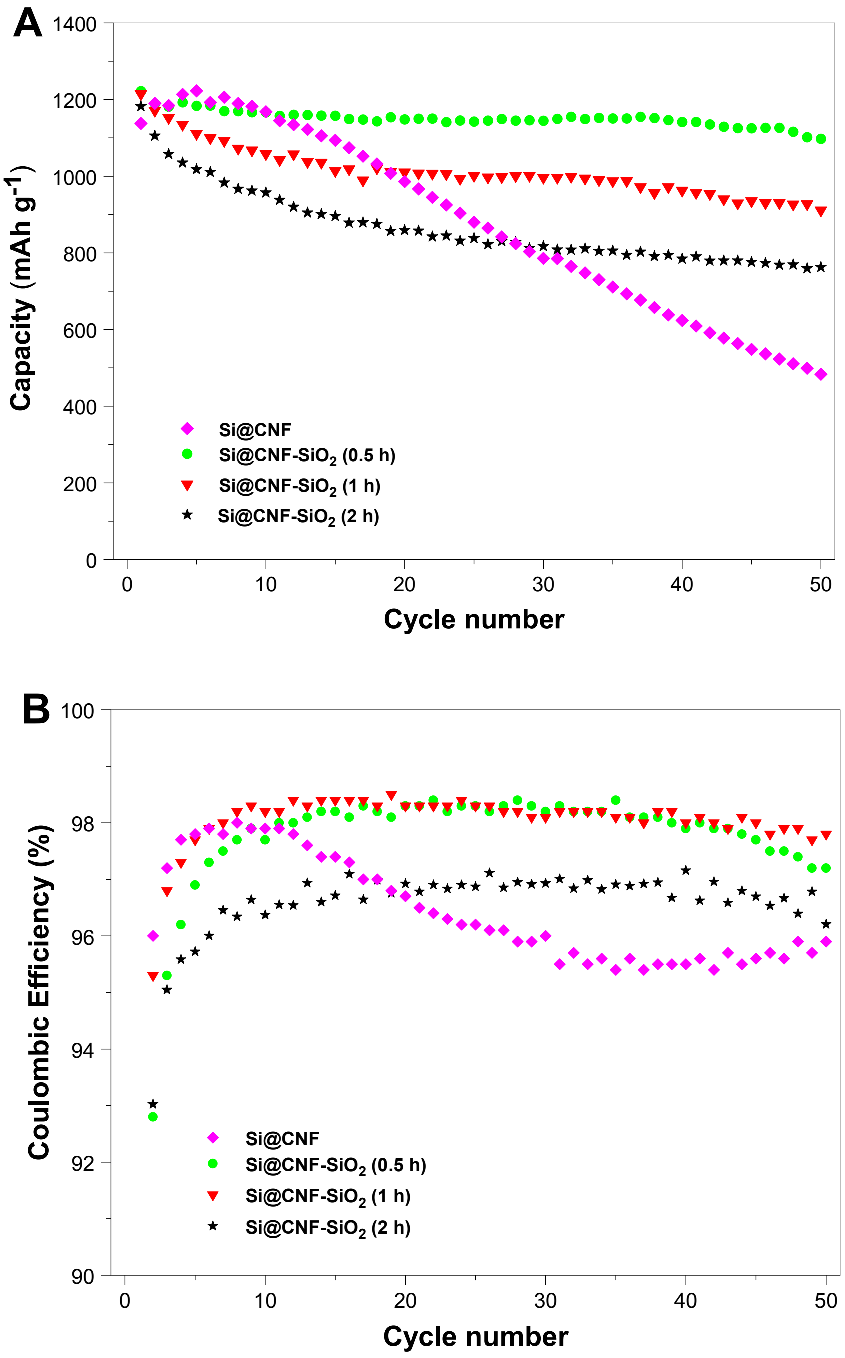

Figure 6.9 : Cycling performance (A) and coulombic efficiencies (B) of Si@C nanofiber composite and Si@C-SiO_2 nanofiber composites with different coating times: 0.5 h, 1 h, and 2h.

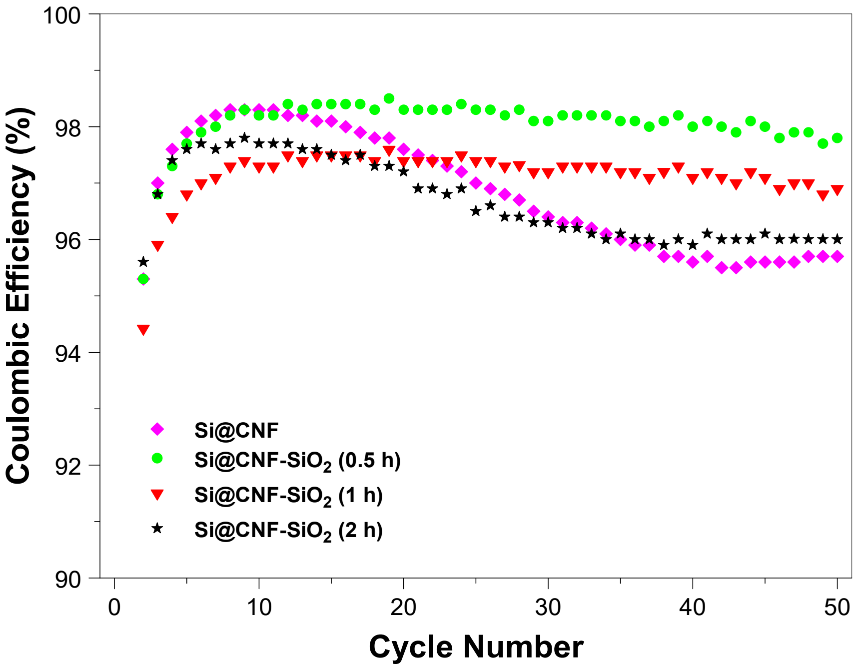

Figure 6.10 : Coulombic efficiencies of Si@C nanofiber composite and Si@C-SiO$_2$ nanofiber composites with different coating times: 0.5 h, 1 h, and 2h with a cutoff voltage window of 0.01 and 1.0 V.

From Figure 6.9, it is also seen that the cycling performance of Si@C-SiO$_2$ nanofiber composites was worsened while increasing SiO$_2$ coating time to 1 h or 2 h. The capacity retention and coulombic efficiency of Si@C-SiO$_2$ nanofiber composite with 1 h coating time was around 75.0% and 97.8%, respectively, at the 50th cycle. For the Si@C-SiO$_2$ nanofiber composite with 2 h coating time, the capacity retention and coulombic efficiency were only around 64.5% and 96.2%, respectively, at the 50th cycle. Therefore, to achieve the enhanced cycling performance, it is very crucial to select an appropriate SiO$_2$ coating thickness for Si@C-SiO$_2$ nanofiber composites. The cycling performance was affected by the easiness of Li-ion diffusion through the SiO$_2$ and SEI layer formed on the nanofiber surface. The fast capacity fading of Si@C-SiO$_2$ nanofiber composites with 1 and 2 h coating times might be caused by the hindered Li-ion insertion/deinsertion during cycling due to their relatively thick SiO$_2$ coating layers. Similar results were reported for nano Si powder electrodes with different oxide layer thicknesses by Yu, et al [179]. In many reported studies, Si based anodes were evaluated with a cutoff voltage window of 0.01 and 1.0 V. To put our results into perspective, we tested our electrodes between 0.01 and 1.0 V at a constant current density of 100 mA g^{-1}, and the measured coulombic efficiencies are shown in Figure 6.10. Results revealed that the coulombic efficiencies of the nanofiber composites in a cutoff voltage window of 0.01 and 1.0 V were quite similar to those tested with a cutoff voltage window of 0.01 and 2.0 V.

The Si@C-SiO$_2$ nanofiber composite with 0.5 h coating time showed the best cycling performance among all the studied nanofiber composites. Therefore, this composite was further investigated for its rate capability under various current densities, as shown in Figure 6.11. It was observed that the charge capacities were around 1177, 1028, 873, and 683 mAh g^{-1}, respectively, at current densities of 100, 200, 400, and 800 mA g^{-1}. The coulombic efficiency remained relatively constant as the current density increased. In addition, the charge capacity reached 1052 mAh g^{-1} when the current density returned to 100 mA g^{-1} after ongoing cycles at higher current densities. This charge capacity (1052 mAh g^{-1}) was very close to initial charge capacity (1177 mAh g^{-1}), demonstrating the good rate capability of the Si@C-SiO$_2$ nanofiber composite.

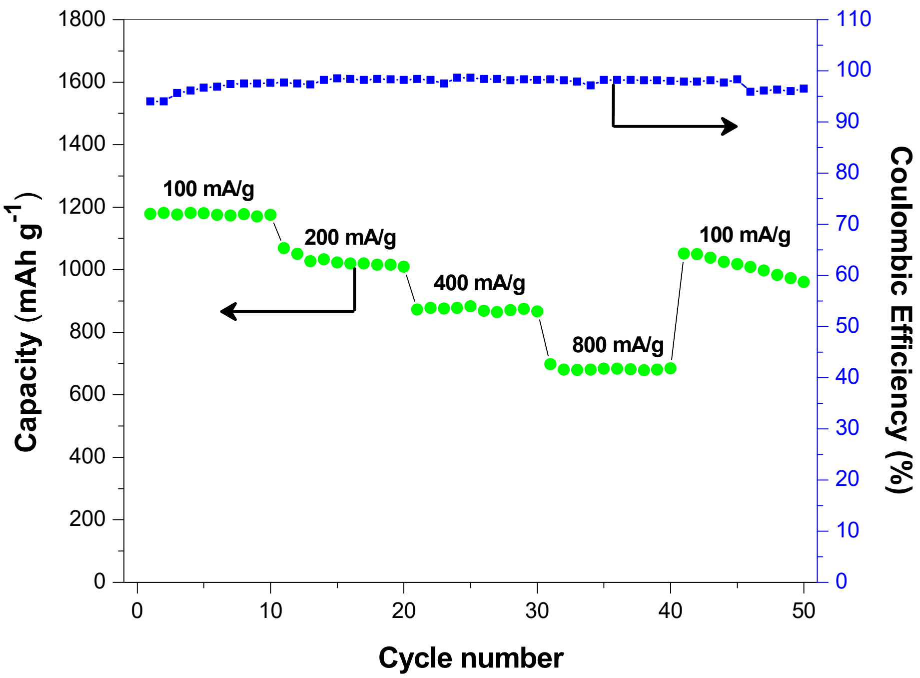

Figure 6.11 : Rate capability of Si@C-SiO$_2$ nanofiber composite with 0.5 h coating time cycled at different current densities.

Electrochemically tested cells were disassembled after 50 cycles to analyze the surface morphology change of Si@C and Si@C-SiO_2 nanofiber composites using TEM (Figure 6.12). Before TEM observation, the cycled electrodes were washed by HCl to remove SEI. Due to the repeated large volume expansion and contraction of Si nanoparticles, the Si@C nanofiber composite suffered major structural deterioration during the cycling and Si nanoparticles fell off from the carbon matrix, causing irreversible structure damage (Figure 6.12A). On the other hand, in Si@C-SiO_2 nanofiber composites, most of the Si nanoparticles were maintained and encapsulated inside the nanofiber matrix after cycling, without catastrophic structural damage to the nanofiber surfaces (Figures 6.12B, C, and D). Results demonstrated that the SiO_2 coating helped restrict Si nanoparticles in carbon matrix during the repetitive cycles.

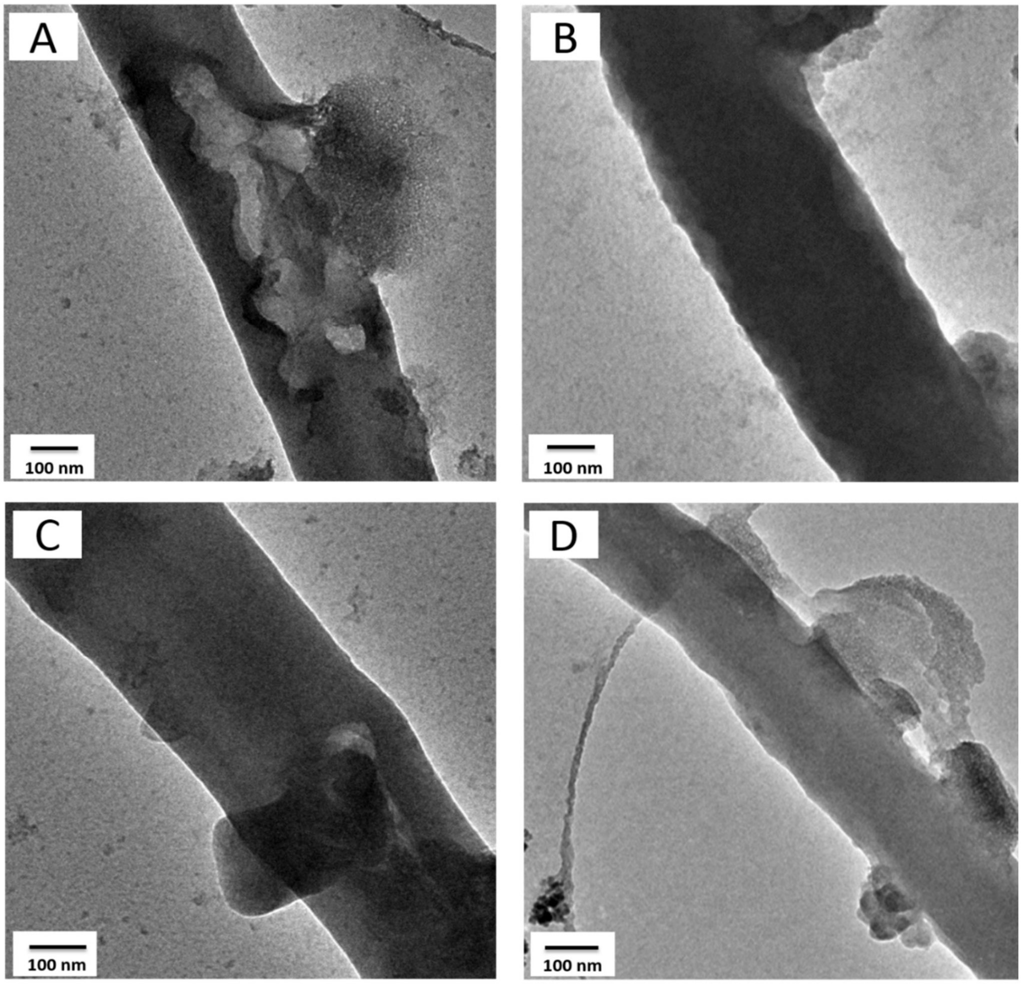

Figure 6.12 : TEM images of cycled Si@C nanofiber composite (A) and Si@C-SiO_2 nanofiber composites with different coating times: (B) 0.5 h, (C) 1 h, and (D) 2h after 50 cycles.

6.4 Conclusions

Nanoscale SiO_2 coating of Si@C nanofiber composites were performed to prevent direct exposure of the Si nanoparticles with the electrolyte solution and increase the mechanical bonding strength between the Si nanoparticles and carbon nanofiber matrix. Results demonstrated that nanoscale SiO_2 coating of Si@C nanofibers helped maintain the Si nanoparticles within the nanofiber structure and stabilize the SEI formation on the electrode surface, resulting in improved cycling performance. Electrochemical performance results showed that the Si@C-SiO_2 nanofiber composite anode with 0.5 h coating time exhibited good capacity retention of 89.8% and high coulombic efficiency of 97.2% at the 50th cycle. It is, therefore, demonstrated that Si@C-SiO_2 nanofiber composites are promising anode material candidate for next-generation high-energy lithium-ion batteries.

7. CONCLUSIONS AND RECOMMENDATIONS

7.1 Conclusions

Electrochemical energy storage have been considered as one of the most crucial technologies for different applications such as portable electronic devices, electric vehicles, and grid storage. Among the various existing energy storage and conversion systems, high-performance rechargeable lithium-ion batteries appear as one of the most promising energy storage devices due to their superior properties such as high energy density, long cycle life, good power performance, and flexible design. The demand for high-performance lithium-ion batteries in terms of high power, high capacity and high rate capability is ever growing due to ongoing technological improvements on electric vehicles and portable electronic devices. Current commercial lithium-ion batteries use graphitic materials in the anode but the theoretical capacity (372 mAh g^{-1}) of graphitic anode materials cannot meet the ever-growing capacity requirements of future portable electronics and electric vehicle technologies. To address these requirements, it is very crucial to introduce new electrode materials to replace the currently used limited-capacity electrodes. Recently, researchers give particular attention to the design and synthesis of high-capacity alternative nanostructured anode materials because nanostructured novel anodes have proven to be crucial to next-generation lithium-ion batteries. Lithium storage capacities of alloy-type anodes (e.g., silicon, tin, germanium, and their oxides) are much higher than that of currently-used intercalation-type graphite anode. Among different alloy-type anodes, Si and tin dioxide (SnO_2) are the most promising candidates for next-generation lithium-ion batteries because of their high gravimetric and volumetric capacities. In our work, we focused on fabricating novel composite nanofibers and discovering their potential applications as anode materials for new-generation high-performance rechargeable lithium-ion batteries. For this purpose we have designed and fabricated novel SnO_2/C and Si/C composite nanofiber structures to combine the advantages of carbon (long cycle life) and lithium active (high storage capacity) materials and improve the electrochemical performance of the introduced composite nanofibers as anode materials for high-performance rechargeable lithium-ion batteries.

A summary of the research outcomes is listed below:

(I) Carbon-Enhanced Electrodeposited SnO_2/Carbon Nanofiber Composites as Anode for Lithium-Ion Batteries

Because of their distinctive properties, such as high capacity, low cost, high abundance, and low toxicity, tin oxides (SnO_2) are thought as promising anode material candidate for next-generation lithium-ion batteries. However, the practical application of SnO_2 anodes is currently limited because of their large volume changes during cycling. Severe volume changes of SnO_2 anodes during the cycling lead to intense pulverization and loss of electrical contact between the active material and carbon conductor. In this work, SnO_2-electrodeposited carbon nanofibers (CNF@SnO_2) and SnO_2-electrodeposited porous carbon nanofibers (PCNF@SnO_2) composites were developed as binder-free anodes for lithium-ion batteries by the electrodeposition of SnO_2 nanoparticles on electrospun carbon. Both CNF@SnO_2 and PCNF@SnO_2 composites were also coated with amorphous carbon layers by chemical vapor deposition (CVD) method to further improve the structural stability and electrochemical performance. Results indicated that the amount of the electrodeposited SnO_2 nanoparticles and the capacity of the resultant composites were successfully increased by using a porous nanofiber structure. Electrochemical performance results showed that the combination of porous nanofiber structure and CVD amorphous carbon coating led to a novel carbon-coated PCNF@SnO_2 composite anode with high capacity retention and large coulombic efficiency.

(II) Carbon-Confined PVA-Derived Silicon/Silica/Carbon Nanofiber Composites as Anode for Lithium-Ion Batteries

Among all alloy-type anodes, Si provides the highest theoretical capacity of 4200 mAh g^{-1}, making it the best candidate for next-generation high-energy lithium-ion batteries In recent years, Si/carbon (Si/C) composite anodes have drawn great attention, which can potentially combine the advantageous properties of Si (high capacity) and C (excellent electronic conductivity and structural stability). However, maintaining the structural integrity of the electrode despite the 400% volume expansion of Si and stabilizing the SEI structure during cycling processes are the most crucial challenges for the development of Si/C based anodes. In this work, new electrode design has been introduced to overcome the aforementioned problems of Si/C based anodes. For this purpose two different Si/C based anodes were synthesized: Si/SiO_2/C nanofiber composite and chemical vapor deposition (CVD) carbon-coated Si/SiO_2/C nanofiber composite. Novel silicon/silica/carbon (Si/SiO_2/C) composite nanofibers were synthesized by electrospinning and subsequent heat treatment of a mixture of Si nanoparticles, sol-gel tetraethyl orthosilicate solution, and aqueous polyvinyl alcohol solution. Si/SiO_2/C nanofibers were also coated with nanoscale amorphous carbon layer by CVD technique to ensure maintaining of the Si nanoparticles within the carbon nanofiber matrix during repetitive charging and discharging processes. Results showed that the SiO_2 component of the composite anodes provided sufficient buffer function to accommodate the volume expansion of the Si nanoparticles and the CVD amorphous carbon coating helped maintain the Si nanoparticles within the carbon nanofiber matrix during repetitive charging and discharging processes.

(III) Flexible Binder-Free Silicon/Silica/Carbon Nanofiber Composites as Anode for Lithium-Ion Batteries

Development of high-capacity flexible electrode materials for high-energy lithium-ion batteries become critically important with technological improvements on portable and bendable electronic equipment such as rollup displays, implantable medical devices, active radio-frequency identification tags, and wearable devices. Although various types of bendable electrode materials have been reported, it is very important to fabricate highly flexible electrode materials with reasonable fabrication technique and high electrochemical performance similar to those of conventional high-capacity electrode materials. In this work, binder-free, flexible Si/SiO_2/C nanofiber composite anode materials were introduced by the combination of Si nanoparticles, sol-gel TEOS solution, and PAN/DMF solution through simple electrospinning and subsequent heat treatment processes. Generating of the nanoscale SiO_2 structure throughout the carbon matrices led to a highly flexible composite nanofiber mat for using as binder-free anode material. To further improve the long-term cycling performance, additional nanoscale carbon coating of flexible Si/SiO_2/C nanofibers was performed by CVD technique. Results demonstrated that, the SiO_2 component of the nanofiber composites provided sufficient buffering function to accommodate the volume expansion of the Si nanoparticles during the repeated charging and discharging cycles. Electrochemical performance results indicated that, CVD carbon-coated flexible $Si/SiO_2/C$ nanofiber composite anode have excellent overall electrochemical performance including high capacity, good cycling stability, and high coulombic efficiency. It is, therefore, demonstrated that CVD carbon-coated flexible $Si/SiO_2/C$ nanofiber composites are promising anode material candidate for next-generation flexible and high-energy lithium-ion batteries.

(IV) SiO_2-Confined Silicon/Carbon Nanofiber Composites as Anode for Lithium-Ion Batteries

Si is considered as the most promising anode material candidate for next-generation high-energy lithium-ion batteries due to its ultra-high theoretical capacity (4200 mAh g^{-1}). However, the practical use of Si based anodes is constrained by the high volume expansion (up to 400%) of Si active material during cycling. Intensive volume change of Si results in severe pulverization, loss of electrical contact between Si particles and carbon current collector, and unstable SEI formation on the electrode surface. These drawbacks result in the severe capacity fading of Si-based anodes during repetitive lithiation and delithiation processes. In this work, we introduced nanoscale silica-coated silicon/carbon (Si@C-SiO_2) nanofiber composites that can maintain their structural stability during repeated cycling. We proposed a feasible method to improve the electrochemical performance of previously reported Si@C nanofiber composite electrodes. The main target of this study is to propose a simple, but effective approach for the confinement of Si nanoparticles inside the Si@C nanofiber composite electrodes. Si@C nanofibers were produced by simple electrospinning and subsequent heat treatment processes. The resultant Si@C nanofibers were coated with nanoscale amorphous SiO_2 layers by using sol-gel TEOS solution to achieve further improvement on the cycling performance of the composite anodes. Results showed that nanoscale SiO_2 coating of Si@C nanofibers helped preserve the Si particles within the nanofiber structure, resulting in stable solid electrolyte interphase formation and improved cycling performance. Electrochemical performance results indicated that Si@C-SiO_2 nanofiber composite anodes had good capacity retention and high coulombic efficiency after 50 cycles. It is, therefore, indicated that nanoscale SiO_2 coating is an effective method to improve the electrochemical performance of Si@C nanofiber composite anodes.

7.2 Recommendation for Future Work

The recommended future work can include but not limited to:

(I) Prepare carbon-enhanced atomic layer deposited SnO_2/carbon nanofiber composite anodes and evaluate their electrochemical performance in lithium-ion batteries

For the nanostructured anode materials produced by a deposition technique, particle agglomerations are considered as one of the most critical issues since it causes high irreversible capacities and short cycle life. Atomic layer deposition (ALD) is a versatile technique for nanoscale thin film coating and can be used for fabrication of the SnO_2/carbon nanofiber composite anodes. In this method, electrospun carbon nanofiber matrix can serve as the substrate and nanoscale SnO_2 active material can be deposited onto the carbon nanofibers substrate by ALD method. In this way, a uniform distribution of the SnO_2 nanoparticles on carbon nanofiber matrix can be obtained. As produced SnO_2/carbon nanofiber composites can also be coated with nanoscale amorphous carbon layer by CVD technique to ensure maintaining of the SnO_2 coating within the carbon nanofiber matrix during repetitive charging and discharging processes. Therefore, an improved overall electrochemical performance can be expected for the introduced composite nanofibers, especially in terms of the cycle life.

(II) Carry out in-situ TEM to identify the detailed mechanism of CVD carbon coated composite nanofiber anodes

According to electrochemical test results, nanoscale CVD carbon coating helps maintain the structural integrity of the composite nanofiber anode during the cycling process and stabilize the solid electrolyte interface (SEI) formation on the anode surface. However, the detailed mechanism of CVD carbon coating is still unknown and needs to be proven using in-situ characterization methods. Hence, the in-situ high-resolution transmission electron microscopy could be performed during the cycling process to understand the roles played by the CVD carbon coating.

(III) Fabricate flexible lithium-ion batteries from flexible binder-free nanofiber composite anodes and cathodes and evaluate their electrochemical performance

With ongoing improvements in technologies of bendable electronic equipment such as rollup displays, implantable medical devices, and wearable devices, flexible batteries become crucially important to meet their energy requirements. As shown in Chapter 5 a novel binder-free, free-standing, and flexible silicon/silica/carbon ($Si/SiO_2/C$) nanofiber composite anodes were successfully fabricated by simple electrospinning and carbonization of a solution composed of Si nanoparticles, sol-gel tetraethyl orthosilicate (TEOS) solution, and polyacrylonitrile (PAN) polymer in *N,N*-dimethylformamide as the solvent. Similar fabrication method can be used for fabrication of flexible lithium iron phosphate/silica/carbon ($LiFePO_4/SiO_2/C$) composite nanofiber cathodes. For such a purpose, $LiFePO_4$ precursor materials should be added into the electrospinning solution instead of Si nanoparticles. Flexible lithium-ion batteries could be fabricated by using flexible $Si/SiO_2/C$ nanofiber composite as anode and $LiFePO_4/SiO_2/C$ nanofiber composite as cathode materials.

REFERENCES

[1] **Manthiram, A., Murugan, A. V., Sarkar, A., and Muraliganth, T.** (2008). Nanostructured electrode materials for electrochemical energy storage and conversion, *Energy & Environmental Science, 1,* 621-638.

[2] **Dirican, M., Yanilmaz, M., and Zhang, X.** (2014). Free-standing polyaniline-porous carbon nanofiber electrodes for symmetric and asymmetric supercapacitors, *RSC Advances, 4*, 59427-59435.

[3] **Winter, M., and Brodd, R. J.** (2004). What are batteries, fuel cells, and supercapacitors?, *Chemical Reviews, 104*, 4245-4270.

[4] **Tarascon, J. M., and Armand, M.** (2001). Issues and challenges facing rechargeable lithium batteries, *Nature, 414*, 359-367.

[5] **Cui, L. F., Hu, L., Choi, J. W., and Cui, Y.** (2010). Light-weight free-standing carbon nanotube-silicon films for anodes of lithium ion batteries, *Acs Nano, 4*, 3671-3678.

[6] **Lin, Z., Ji, L., Woodroof, M. D., and Zhang, X.** (2010). Electrodeposited MnOx/carbon nanofiber composites for use as anode materials in rechargeable lithium-ion batteries, *Journal of Power Sources, 195*, 5025-5031.

[7] **Winter, M., Besenhard, J. O., Spahr, M. E., and Novak, P.** (1998). Insertion electrode materials for rechargeable lithium batteries, *Advanced Materials, 10*, 725-763.

[8] **Wu, H., and Cui, Y.** (2012). Designing nanostructured Si anodes for high energy lithium ion batteries, *Nano Today*, *7,* 414-429.

[9] **De Las Casas, C., and Li, W.** (2012). A review of application of carbon nanotubes for lithium ion battery anode material, *Journal of Power Sources, 208*, 74-85.

[10] **Choi, N. S., Chen, Z., Freunberger, S. A., Ji, X., Sun, Y. K., Amine, K., Yushin, G., Nazar, L. F., Cho, J., and Bruce, P. G.** (2012). Challenges facing lithium batteries and electrical double-layer capacitors, *Angewandte Chemie International Edition, 51*, 9994-10024.

[11] **Padhi, A. K., Nanjundaswamy, K., and Goodenough, J.** (1997). Phospho-olivines as positive- electrode materials for rechargeable lithium batteries, *Journal of The Electrochemical Society, 144*, 1188-1194.

[12] **Fergus, J. W.** (2010). Recent developments in cathode materials for lithium ion batteries, *Journal of Power Sources, 195*, 939-954.

[13] **Shukla, A., and Prem Kumar, T.** (2008). Materials for next-generation lithium batteries, *Current Science, 94*, 314-331.

[14] **Chen, Z., and Amine, K.** (2006). Capacity fade of Li_{1+x} $Mn_{2-x}O_4$-based lithium-ion cells, *Journal of The Electrochemical Society, 153*, A316-A320.

[15] **Song, J. W., Nguyen, C. C., Choi, H., Lee, K. H., Han, K. H., Kim, Y. J., Choy, S., and Song, S. W.** (2011). Impacts of surface Mn valence on cycling performance and surface chemistry of Li-and Al-substituted spinel battery cathodes, *Journal of The Electrochemical Society, 158*, A458-A464.

[16] **Yamada, A., Hosoya, M., Chung, S. C., Kudo, Y., Hinokuma, K., Liu, K. Y., and Nishi, Y.** (2003). Olivine-type cathodes: achievements and problems, *Journal of Power Sources, 119*, 232-238.

[17] **Chung, S. Y., Bloking, J. T., and Chiang, Y. M.** (2002). Electronically conductive phospho-olivines as lithium storage electrodes, *Nature Materials, 1*, 123-128.

[18] **Kang, B., and Ceder, G.** (2009). Battery materials for ultrafast charging and discharging, *Nature, 458*, 190-193.

[19] **Delmas, C., Maccario, M., Croguennec, L., Le Cras, F., and Weill, F.** (2008). Lithium deintercalation in $LiFePO_4$ nanoparticles via a domino-cascade model, *Nature Materials, 7*, 665-671.

[20] **Wang, Y., Wang, Y., Hosono, E., Wang, K., and Zhou, H.** (2008). The design of a $LiFePO_4$/carbon nanocomposite with a core-shell structure and its synthesis by an in situ polymerization restriction method, *Angewandte Chemie International Edition, 47*, 7461-7465.

[21] **Wu, X. L., Jiang, L. Y., Cao, F. F., Guo, Y. G., and Wan, L. J.** (2009). $LiFePO_4$ nanoparticles embedded in a nanoporous carbon matrix: superior cathode material for electrochemical energy-storage devices, *Advanced Materials, 21*, 2710-2714.

[22] **Lascaud, M., Lachter, A., Salardenne, J., and Barriere, A.** (1979). Electrical conduction mechanisms in FeF_3 thin films, *Thin Solid Films, 59*, 353-360.

[23] **Badway, F., Pereira, N., Cosandey, F., and Amatucci, G.** (2003). Carbon-metal fluoride nanocomposites structure and electrochemistry of FeF_3:C, *Journal of The Electrochemical Society, 150*, A1209-A1218.

[24] **Maier, J.** (2002). Nano-sized mixed conductors (Aspects of nano-ionics. Part III), *Solid State Ionics, 148*, 367-374.

[25] **Liao, P., Dunlap, R., and Dahn, J.** (2008). A Mössbauer effect study of combinatorially prepared Al_2O_3/Fe and LiF/Fe multilayers, *Journal of Physics: Condensed Matter, 20*, 055203.

[26] **Makimura, Y., Rougier, A., Laffont, L., Womes, M., Jumas, J. C., Leriche, J. B., and Tarascon, J. M.** (2006). Electrochemical behaviour of low temperature grown iron fluoride thin films, *Electrochemistry Communications, 8*, 1769-1774.

[27] **Cheng, F., Liang, J., Tao, Z., and Chen, J.** (2011). Functional materials for rechargeable batteries, *Advanced Materials, 23*, 1695-1715.

[28] **Kumar, T. P., Kumari, T. S. D., and Stephan, M. A.** (2012). Carbonaceous anode materials for lithium-ion batteries-the road ahead, *Journal of the Indian Institute of Science, 89*, 393-424.

[29] **Dahn, J., Sleigh, A., Shi, H., Reimers, J., Zhong, Q., and Way, B.** (1993). Dependence of the electrochemical intercalation of lithium in carbons on the crystal structure of the carbon, *Electrochimica Acta, 38*, 1179-1191.

[30] **Franklin, R. E.** (1951). Crystallite growth in graphitizing and non-graphitizing carbons, *Proceedings of the Royal Society A: Mathematical, Physical and Engineering Sciences, 209*, 196-218.

[31] **Noked, M., Soffer, A., and Aurbach, D.** (2011). The electrochemistry of activated carbonaceous materials: past, present, and future, *Journal of Solid State Electrochemistry, 15*, 1563-1578.

[32] **Buiel, E., and Dahn, J.** (1999). Li-insertion in hard carbon anode materials for Li-ion batteries, *Electrochimica Acta, 45*, 121-130.

[33] **Zheng, T., McKinnon, W., and Dahn, J.** (1996). Hysteresis during lithium insertion in hydrogen-containing carbons, *Journal of the Electrochemical Society, 143*, 2137-2145.

[34] **Wang, S., Kakumoto, T., Matsui, H., and Matsumura, Y.** (1999). Mechanism of lithium insertion into disordered carbon, *Synthetic Metals, 103*, 2523-2524.

[35] **Jiang, C., Hosono, E., and Zhou, H.** (2006). Nanomaterials for lithium ion batteries, *Nano Today, 1*, 28-33.

[36] **Loutfy, R. O., Hossain, S., Moravsky, A., and Saleh, M.** (2002). Nanotubes as anode material for lithium-ion batteries, *Perspectives of Fullerene Nanotechnology*, 341-355.

[37] **Zhang, H., Cao, G., and Yang, Y.** (2009). Carbon nanotube arrays and their composites for electrochemical capacitors and lithium-ion batteries, *Energy & Environmental Science, 2*, 932-943.

[38] **Deng, D., and Lee, J. Y.** (2007). One-step synthesis of polycrystalline carbon nanofibers with periodic dome-shaped interiors and their reversible lithium-ion storage properties, *Chemistry of Materials, 19*, 4198-4204.

[39] **Subramanian, V., Zhu, H., and Wei, B.** (2006). High rate reversibility anode materials of lithium batteries from vapor-grown carbon nanofibers, *The Journal of Physical Chemistry B, 110*, 7178-7183.

[40] **Cheng, F., Tao, Z., Liang, J., and Chen, J.** (2007). Template-directed materials for rechargeable lithium-ion batteries†, *Chemistry of Materials, 20*, 667-681.

[41] **Ji, L., and Zhang, X.** (2009). Fabrication of porous carbon nanofibers and their application as anode materials for rechargeable lithium-ion batteries, *Nanotechnology, 20*, 155705.

[42] **Courtney, I. A., and Dahn, J.** (1997). Electrochemical and in situ X-ray diffraction studies of the reaction of lithium with tin oxide composites, *Journal of the Electrochemical Society, 144*, 2045-2052.

[43] **Zhang, H. X., Feng, C., Zhai, Y. C., Jiang, K. L., Li, Q. Q., and Fan, S. S.** (2009). Cross-stacked carbon nanotube sheets uniformly loaded with SnO_2 nanoparticles: a novel binder-free and high-capacity anode material for lithium-ion batteries, *Advanced Materials, 21*, 2299-2304.

[44] **Beaulieu, L., and Dahn, J.** (2000). The reaction of lithium with Sn-Mn-C intermetallics prepared by mechanical alloying, *Journal of The Electrochemical Society, 147*, 3237-3241.

[45] **Ui, K., Kikuchi, S., Kadoma, Y., Kumagai, N., Ito, S.** (2009). Electrochemical characteristics of Sn film prepared by pulse electrodeposition method as negative electrode for lithium secondary batteries, *Journal of Power Sources, 189*, 224-229.

[46] **Mao, O., Dunlap, R., and Dahn, J.** (1999). Mechanically alloyed Sn-Fe (-C) powders as anode materials for Li-ion batteries: I. the Sn_2Fe-C system, *Journal of The Electrochemical Society, 146*, 405-413.

[47] **Tirado, J. L.** (2003). Inorganic materials for the negative electrode of lithium-ion batteries: state-of-the-art and future prospects, *Materials Science and Engineering: R: Reports, 40*, 103-136.

[48] **Lupu, C., Mao, J. G., Rabalais, J. W., Guloy, A. M., and Richardson, J. W.** (2003). X-ray and neutron diffraction studies on "$Li_4.4Sn$", *Inorganic Chemistry, 42*, 3765-3771.

[49] **Han, F., Li, W. C., Li, M. R., and Lu, A. H.** (2012). Fabrication of superior-performance SnO_2@C composites for lithium-ion anodes using tubular mesoporous carbon with thin carbon walls and high pore volume, *Journal of Materials Chemistry, 22*, 9645-9651.

[50] **Guo, X., Fang, X., Sun, Y., Shen, L., Wang, Z., and Chen, L.** (2012). Lithium storage in carbon-coated SnO_2 by conversion reaction, *Journal of Power Sources, 226*, 75-81.

[51] **Lou, X. W., Li, C. M., and Archer, L. A.** (2009). Designed synthesis of coaxial SnO_2@ carbon hollow nanospheres for highly reversible lithium storage, *Advanced Materials, 21*, 2536-2539.

[52] **Chen, J. S., Cheah, Y. L., Chen, Y. T., Jayaprakash, N., Madhavi, S., Yang, Y. H., and Lou, X. W.** (2009). SnO_2 nanoparticles with controlled carbon nanocoating as high-capacity anode materials for lithium-ion batteries, *The Journal of Physical Chemistry C, 113*, 20504-20508.

[53] **Sun, X., Liu, J., and Li, Y.** (2006). Oxides@C core-shell nanostructures: One-pot synthesis, rational conversion, and Li storage property, *Chemistry of Materials, 18*, 3486-3494.

[54] **Huang, X., Zhou, X., Zhou, L., Qian, K., Wang, Y., Liu, Z., and Yu, C.** (2011). A facile one-step solvothermal synthesis of SnO_2/graphene nanocomposite and its application as an anode material for lithium-ion batteries, *ChemPhysChem, 12*, 278-281.

[55] **Guo, Z. P., Du, G. D., Nuli, Y., Hassan, M. F., and Liu, H. K.** (2009). Ultra-fine porous SnO_2 nanopowder prepared via a molten salt process: a highly efficient anode material for lithium-ion batteries, *Journal of Materials Chemistry, 19*, 3253-3257.

[56] **Kim, H., and Cho, J.** (2008). Hard templating synthesis of mesoporous and nanowire SnO_2 lithium battery anode materials, *Journal of Materials Chemistry, 18*, 771-775.

[57] **Li, Y., Zhu, S., Liu, Q., Gu, J., Guo, Z., Chen, Z., Feng, C., Zhang, D., and Moon, W. J.** (2012). Carbon-coated SnO_2@C with hierarchically porous structures and graphite layers inside for a high-performance lithium-ion battery, *Journal of Materials Chemistry, 22*, 2766-2773.

[58] **Kong, J., Liu, Z., Yang, Z., Tan, H. R., Xiong, S., Wong, S. Y., Li, X., and Lu, X.** (2012). Carbon/SnO_2/carbon core/shell/shell hybrid nanofibers: tailored nanostructure for the anode of lithium ion batteries with high reversibility and rate capacity, *Nanoscale, 4*, 525-530.

[59] **He, M., Yuan, L., Hu, X., Zhang, W., Shu, J., and Huang, Y.** (2013). A SnO_2@ carbon nanocluster anode material with superior cyclability and rate capability for lithium-ion batteries, *Nanoscale, 5*, 3298-3305.

[60] **Ding, S., Chen, J. S., Lou, and X. W.** (2011). CNTs@SnO_2@ carbon coaxial nanocables with high mass fraction of SnO2 for improved lithium storage, *Chemistry-An Asian Journal, 6*, 2278-2281.

[61] **Liu, J., Li, W., and Manthiram, A.** (2010). Dense core-shell structured SnO_2/C composites as high performance anodes for lithium ion batteries, *Chemical Communications, 46*, 1437-1439.

[62] **Lou, X. W., Deng, D., Lee, J. Y., and Archer, L. A.** (2008). Preparation of SnO_2/carbon composite hollow spheres and their lithium storage properties, *Chemistry of Materials, 20*, 6562-6566.

[63] **Lou, X. W., Chen, J. S., Chen, P., and Archer, L. A.** (2009). One-pot synthesis of carbon-coated SnO_2 nanocolloids with improved reversible lithium storage properties, *Chemistry of Materials, 21*, 2868-2874.

[64] **Wang, Y., Zeng, H. C., and Lee, J. Y.** (2006). Highly reversible lithium storage in porous SnO_2 nanotubes with coaxially grown carbon nanotube overlayers, *Advanced Materials, 18*, 645-649.

[65] **Wang, Z., Chen, G., Xia, D.** (2008). Coating of multi-walled carbon nanotube with SnO_2 films of controlled thickness and its application for Li-ion battery, *Journal of Power Sources, 184*, 432-436.

[66] **Ji, L., Lin, Z., Guo, B., Medford, A. J., Zhang, X.** (2010). Assembly of carbon-SnO_2 core-sheath composite nanofibers for superior lithium storage, *Chemistry-A European Journal, 16*, 11543-11548.

[67] **Wu, H., Zheng, G., Liu, N., Carney, T. J., Yang, Y., and Cui, Y.** (2012). Engineering empty space between Si nanoparticles for lithium-ion battery anodes, *Nano Letters, 12*, 904-909.

[68] **Jang, S. M., Miyawaki, J., Tsuji, M., Mochida, I., Yoon, S. H.** (2009). The preparation of a novel Si-CNF composite as an effective anodic material for lithium-ion batteries, *Carbon, 47*, 3383-3391.

[69] **Lee, B. S., Son, S. B., Park, K. M., Seo, J. H., Lee, S. H., Choi, I. S., Oh, K. H., and Yu, W. R.** (2012). Fabrication of Si core/C shell nanofibers and their electrochemical performances as a lithium-ion battery anode, *Journal of Power Sources, 206*, 267-273.

[70] **Ji, L., Lin, Z., Zhou, R., Shi, Q., Toprakci, O., Medford, A. J., Millns, C. R., and Zhang, X.** (2010). Formation and electrochemical performance of copper/carbon composite nanofibers, *Electrochimica Acta, 55*, 1605-1611.

[71] **Zhang, Q. Zhang, W., Wan, W., Cui, Y., and Wang, E.** (2010). Lithium insertion in silicon nanowires: an ab initio study, *Nano Letters, 10*, 3243-3249.

[72] **Zhang, X., Ji, L., Toprakci, O., Liang, Y., and Alcoutlabi, M.** (2011). Electrospun nanofiber-based anodes, cathodes, and separators for advanced lithium-ion batteries, *Polymer Reviews, 51*, 239-264.

[73] **Hwang, T. H., Lee, Y. M., Kong, B. S., Seo, J. S., and Choi, J. W.** (2012). Electrospun core-shell fibers for robust silicon nanoparticle-based lithium ion battery anodes, *Nano Letters, 12*, 802-807.

[74] **Pharr, M., Zhao, K., Wang, X., Suo, Z., and Vlassak, J. J.** (2012). Kinetics of initial lithiation of crystalline silicon electrodes of lithium-ion batteries, *Nano Letters, 12*, 5039-5047.

[75] **Fu, K., Yildiz, O., Bhanushali, H., Wang, Y., Stano, K., Xue, L., Zhang, X., and Bradford, P.D.** (2013). Aligned carbon nanotube-silicon sheets: a novel nano-architecture for flexible lithium ion battery electrodes, *Advanced Materials, 25*, 5109-5114.

[76] **Xinping, H., Bo, G., Guibao, W., Jiatong, W., and Chun, Z.** (2013). A new nanocomposite: Carbon cloth based polyaniline for an electrochemical supercapacitor, *Electrochimica Acta, 111*, 210-215.

[77] **Cui, L. F., Yang, Y., Hsu, C. M., and Cui, Y.** (2009). Carbon-silicon core-shell nanowires as high capacity electrode for lithium ion batteries, *Nano Letters, 9*, 3370-3374.

[78] **Iwamura, S., Nishihara, H., and Kyotani, T.** (2012). Effect of buffer size around nanosilicon anode particles for lithium-ion batteries, *The Journal of Physical Chemistry C, 116*, 6004-6011.

[79] **Liu, B., Zhang, J., Wang, X., Chen, G., Chen, D., Zhou, C., and Shen, G.** (2012). Hierarchical three-dimensional $ZnCo_2O_4$ nanowire arrays/carbon cloth anodes for a novel class of high-performance flexible lithium-ion batteries, *Nano Letters, 12*, 3005-3011.

[80] **Chen, S., Gordin, M. L., Yi, R., Howlett, G., Sohn, H., and Wang, D.** (2012). Silicon core-hollow carbon shell nanocomposites with tunable buffer voids for high capacity anodes of lithium-ion batteries, *Physical Chemistry Chemical Physics : PCCP, 14*, 12741-12745.

[81] **Su, L., Jing, Y., and Zhou, Z.** (2011). Li ion battery materials with core-shell nanostructures, *Nanoscale, 3*, 3967-3983.

[82] **Liu, N., Wu, H., McDowell, M. T., Yao, Y., Wang, C., and Cui, Y.** (2012). A yolk-shell design for stabilized and scalable li-ion battery alloy anodes, *Nano Letters, 12*, 3315-3321.

[83] **Cao, Y., Xiao, L., Wang, W., Choi, D., Nie, Z., Yu, J., Saraf, L.V., Yang, Z. , and Liu, J.** (2011). Reversible sodium ion insertion in single crystalline manganese oxide nanowires with long cycle life, *Advanced Materials, 23*, 3155-3160.

[84] **Wu, H., Chan, G., Choi, J. W., Yao, Y., McDowell, M. T., Lee, S. W., Jackson, A., Yang, Y., Hu, L., and Cui, Y.** (2012). Stable cycling of double-walled silicon nanotube battery anodes through solid-electrolyte interphase control, *Nature Nanotechnology, 7*, 310-315.

[85] **Yang, S., Cui, G., Pang, S., Cao, Q., Kolb, U., Feng, X., Maier, J., and Müllen, K.** (2010). Fabrication of cobalt and cobalt oxide/graphene composites: Towards high-performance anode materials for lithium ion batteries, *ChemSusChem, 3*, 236-239.

[86] **Lou, X. W., Deng, D., Lee, J. Y., Feng, J., and Archer, L.A.** (2008). Self-supported formation of needlelike Co_3O_4 nanotubes and their application as lithium-ion battery electrodes, *Advanced Materials, 20,* 258-262.

[87] **Li, Y., Tan, B., and Wu, Y.** (2008). Mesoporous Co_3O_4 nanowire arrays for lithium ion batteries with high capacity and rate capability, *Nano Letters, 8*, 265-270.

[88] **Tian, L., Zou, H., Fu, J., Yang, X., Wang, Y., Guo, H., Fu, X., Liang, C., Wu, M., and Shen, P. K.** (2010). Topotactic conversion route to mesoporous quasi-single-crystalline Co_3O_4 nanobelts with optimizable electrochemical performance, *Advanced Functional Materials, 2*0, 617-623.

[89] **Sun, Y., Feng, X. Y., and Chen, C. H.** (2011). Hollow Co_3O_4 thin films as high performance anodes for lithium-ion batteries, *Journal of Power Sources, 196*, 784-787.

[90] **Fu, Y., Li, X., Sun, X., Wang, X., Liu, D., and He, D.** (2012). Self-supporting Co_3O_4 with lemongrass-like morphology as a high-performance anode material for lithium ion batteries, *Journal of Materials Chemistry, 2*2, 17429-17431.

[91] **Wu, M. S., Chiang, P. C. J., Lee, J. T., and Lin, J. C.** (2005). Synthesis of manganese oxide electrodes with interconnected nanowire structure as an anode material for rechargeable lithium ion batteries, *The Journal of Physical Chemistry B, 109*, 23279-23284.

[92] **Wu, M. S., and Chiang, P. C. J.** (2006). Electrochemically deposited nanowires of manganese oxide as an anode material for lithium-ion batteries, *Electrochemistry Communications, 8*, 383-388.

[93] **Aragón, M., Pérez-Vicente, C., and Tirado, J.** (2007). Submicronic particles of manganese carbonate prepared in reverse micelles: A new electrode material for lithium-ion batteries, *Electrochemistry Communications, 9*, 1744-1748.

[94] **Yu, X., He, Y., Sun, J., Tang, K., Li, H., Chen, L., and Huang, X.** (2009). Nanocrystalline MnO thin film anode for lithium ion batteries with low overpotential, *Electrochemistry Communications, 11*, 791-794.

[95] **Armstrong, G., Armstrong, A. R., Bruce, P. G., Reale, P., and Scrosati, B.** (2006). TiO_2 (B) nanowires as an improved anode material for lithium-ion batteries containing $LiFePO_4$ or $LiNi_{0.5}Mn_{1.5}O_4$ cathodes and a polymer electrolyte, *Advanced Materials, 18*, 2597-2600.

[96] **Wang, K., Wei, M., Morris, M.A., Zhou, H., and Holmes, J. D.** (2007). Mesoporous titania nanotubes: their preparation and application as electrode materials for rechargeable lithium batteries, *Advanced Materials, 19*, 3016.

[97] **Amine, K., Belharouak, I., Chen, Z., Tran, T., Yumoto, H., Ota, N., Myung, S. T., and Sun, Y. K.** (2010). Nanostructured anode material for high-power battery system in electric vehicles, *Advanced Materials, 22*, 3052-3057.

[98] **Goodenough, J. B., and Kim, Y.** (2009). Challenges for rechargeable Li batteries, *Chemistry of Materials, 22*, 587-603.

[99] **Seki, S., Ohno, Y., Kobayashi, Y., Miyashiro, H., Usami, A., Mita, Y., Tokuda, H., Watanabe, M., Hayamizu, K., and Tsuzuki, S.** (2007). Imidazolium-based room-temperature ionic liquid for lithium secondary batteries effects of lithium salt concentration, *Journal of The Electrochemical Society, 154*, A173-A177.

[100] **Christie, A. M., Lilley, S. J., Staunton, E., Andreev, Y. G., and Bruce, P. G.** (2005). Increasing the conductivity of crystalline polymer electrolytes, *Nature, 433*, 50-53.

[101] **Choi, S. W., Kim, J. R., Ahn, Y. R., Jo, S. M., and Cairns, E. J.** (2007). Characterization of electrospun PVDF fiber-based polymer electrolytes, *Chemistry of Materials, 19*, 104-115.

[102] **Hassoun, J., Panero, S., Reale, P., and Scrosati, B.** (2009). A New, Safe, High-rate and high-energy polymer lithium-ion battery, *Advanced Materials, 21*, 4807-4810.

[103] **Li, D., and Xia, Y.** (2004). Electrospinning of nanofibers: reinventing the wheel?, A*dvanced Materials, 16*, 1151-1170.

[104] **Thavasi, V., Singh, G., and Ramakrishna, S.** (2008). Electrospun nanofibers in energy and environmental applications, *Energy & Environmental Science, 1*, 205-221.

[105] **Huang, Z. M., Zhang, Y. Z., Kotaki, M., and Ramakrishna, S.** (2003). A review on polymer nanofibers by electrospinning and their applications in nanocomposites, *Composites Science and Technology, 63*, 2223-2253.

[106] **Sawicka, K. M., and Gouma, P.** (2006). Electrospun composite nanofibers for functional applications, *Journal of Nanoparticle Research, 8*, 769-781.

[107] **Greiner, A., and Wendorff, J. H.** (2007). Electrospinning: a fascinating method for the preparation of ultrathin fibers, *Angewandte Chemie International Edition, 46*, 5670-5703.

[108] **Reneker, D. H., Yarin, A. L., Fong, H., and Koombhongse, S.** (2000). Bending instability of electrically charged liquid jets of polymer

solutions in electrospinning, *Journal of Applied Physics, 87*, 4531-4547.

[109] **Teo, W. E., Inai, R., and Ramakrishna, S.** (2011). Technological advances in electrospinning of nanofibers, *Science and Technology of Advanced Materials, 12*, 013002.

[110] **Liu, C.K., Lai, K., Liu, W., Yao, M., and Sun, R. J.** (2009) Preparation of carbon nanofibres through electrospinning and thermal treatment, *Polymer International, 58*, 1341-1349.

[111] **Frenot, A., and Chronakis, I. S.** (2003). Polymer nanofibers assembled by electrospinning, *Current Opinion in Colloid & Interface Science, 8*, 64-75.

[112] **Lu, X., Wang, C., and Wei, Y.** (2009). One-dimensional composite nanomaterials: synthesis by electrospinning and their applications, *Small, 5*, 2349-2370.

[113] **Dong, Z., Kennedy, S. J., and Wu, Y.** (2011). Electrospinning materials for energy-related applications and devices, *Journal of Power Sources, 196*, 4886-4904.

[114] **Xie, J., MacEwan, M. R., Willerth, S. M., Li, X., Moran, D. W., Sakiyama-Elbert, S. E., and Xia, Y.** (2009). Conductive core-sheath nanofibers and their potential application in neural tissue engineering, *Advanced Functional Materials, 19*, 2312.

[115] **Kim, C., Yang, K. S., Kojima, M., Yoshida, K., Kim, Y. J., Kim, Y.A., and Endo, M.** (2006). Fabrication of electrospinning-derived carbon nanofiber webs for the anode material of lithium-ion secondary batteries, *Advanced Functional Materials, 16*, 2393-2397.

[116] **Bellan, L. M., and Craighead, H. G.** (2009). Nanomanufacturing using electrospinning, *Journal of Manufacturing Science and Engineering, 131*, 034001.

[117] **Fang, J., Niu, H., Lin, T., and Wang, X.** (2008). Applications of electrospun nanofibers, *Chinese Science Bulletin, 53*, 2265-2286.

[118] **Chand, S.** (2000). Review carbon fibers for composites, *Journal of Materials Science, 35*, 1303-1313.

[119] **Tang, M., and Bacon, R.** (1964). Carbonization of cellulose fibers-I. low temperature pyrolysis, *Carbon, 2*, 211-220.

[120] **Matsumoto, T.** (1985). Mesophase pitch and its carbon fibers, *Pure and Applied Chemistry, 57*, 1553-1562.

[121] **Xuyen, N. T., Ra, E. J., Geng, H. Z., Kim, K. K., An, K. H., and Lee, Y. H.** (2007). Enhancement of conductivity by diameter control of polyimide-

based electrospun carbon nanofibers, *The Journal of Physical Chemistry B, 111*, 11350-11353.

[122] **Inagaki, M., Yang, Y., and Kang, F.** (2012). Carbon nanofibers prepared via electrospinning, *Advanced Materials, 24*, 2547-2566.

[123] **Rahaman, M., Ismail, A. F., and Mustafa, A.** (2007). A review of heat treatment on polyacrylonitrile fiber, *Polymer Degradation and Stability, 92*, 1421-1432.

[124] **Zhu, D., Xu, C., Nakura, N., and Matsuo, M.** (2002). Study of carbon films from PAN/VGCF composites by gelation/crystallization from solution, *Carbon, 40*, 363-373.

[125] **Edie, D.** (1998). The effect of processing on the structure and properties of carbon fibers, *Carbon, 36*, 345-362.

[126] **Mittal, J., Bahl, O., and Mathur, R.** (1997). Single step carbonization and graphitization of highly stabilized PAN fibers, *Carbon, 35*, 1196-1197.

[127] **Zhu, Y., Zhang, J.C., Zhai, J., Zheng, Y.M., Feng, L., and Jiang, L.** (2006). Multifunctional carbon nanofibers with conductive, magnetic and superhydrophobic properties, *ChemPhysChem, 7*, 336-341.

[128] **Fan, X., Zou, L., Zheng, Y. P., Kang, F. Y., and Shen, W. C.** (2009). Electrospinning preparation of nanosilicon/disordered carbon composite as anode materials in li-ion battery, *Electrochemical and Solid-State Letters, 12*, A199-A201.

[129] **Yu, X., Yang, S., Zhang, B., Shao, D., Dong, X., Fang, Y., Li, Z., and Wang, H.** (2011). Controlled synthesis of SnO_2@carbon core-shell nanochains as high-performance anodes for lithium-ion batteries, *Journal of Materials Chemistry, 21*, 12295-12302.

[130] **Liu, X., Wu, M., Li, M., Pan, X., Chen, J., and Bao, X.** (2013). Facile encapsulation of nanosized SnO2 particles in carbon nanotubes as an efficient anode of Li-ion batteries, *Journal of Materials Chemistry A, 1*, 9527-9535.

[131] Zhang, L., Zhang, G., Wu, H. B., Yu, L., and Lou, X. W. D. (2013). Hierarchical tubular structures constructed by carbon-coated SnO_2 nanoplates for highly reversible lithium storage, *Advanced Materilas, 25*, 2589–2593.

[132] **Zhang, S., Li, Y., Xu, G., Li, S., Lu, Y., Toprakci, O., and Zhang, X.** (2012). High-capacity $Li_2Mn_{0.8}Fe_{0.2}SiO_4$/carbon composite nanofiber cathodes for lithium-ion batteries, *Journal of Power Sources, 213*, 10-15.

[133] **Wu, P., Du, N., Zhang, H., Yu, J., and Yang, D.** (2010). CNTs@ SnO_2@ C coaxial nanocables with highly reversible lithium storage, *The Journal of Physical Chemistry C, 114*, 22535-22538.

[134] **Fan, X. Y., Shi, X. Y., Wang, J., Shi, Y. X., Wang, J. J., Xu, L., Gou, L., and Li, D. L.** (2013). Sucrose assisted hydrothermal synthesis of SnO_2/graphene nanocomposites with improved lithium storage properties, *Journal of Solid State Electrochemistry, 17*, 201-208.

[135] **Bonino, C. A., Ji, L., Lin, Z., Toprakci, O., Zhang, X., and Khan, S. A.** (2011). Electrospun carbon-tin oxide composite nanofibers for use as lithium ion battery anodes, *ACS Applied Materials & Interfaces, 3*, 2534-2542.

[136] **Wu, M. S., Ou, Y. H., and Lin, Y. P.** (2010). Electrodeposition of iron oxide nanorods on carbon nanofiber scaffolds as an anode material for lithium-ion batteries, *Electrochimica Acta, 55*, 3240-3244.

[137] **Rasheed, A., Howe, J. Y., Dadmun, M. D., and Britt, P. F.** (2007). The efficiency of the oxidation of carbon nanofibers with various oxidizing agents, *Carbon, 45*, 1072-1080.

[138] **Lin, Z., Ji, L., and Zhang, X.** (2009). Electrodeposition of platinum nanoparticles onto carbon nanofibers for electrocatalytic oxidation of methanol, *Materials Letters, 63*, 2115-2118.

[139] **Li, Y., Lv, X., Lu, J., and Li, J.** (2010). Preparation of SnO2-nanocrystal/graphene-nanosheets composites and their lithium storage ability, *The Journal of Physical Chemistry C, 114*, 21770-21774.

[140] **Fu, K., Xue, L., Yildiz, O., Li, S., Lee, H., Li, Y., Xu, G., Zhou, L., Bradford, P. D., and Zhang, X.** (2013). Effect of CVD carbon coatings on Si@CNF composite as anode for lithium-ion batteries, *Nano Energy, 2,* 976-986.

[141] **Yang, R., Zhao, W., Zheng, J., Zhang, X., and Li, X.** (2010). One-step synthesis of carbon-coated tin dioxide nanoparticles for high lithium storage, *The Journal of Physical Chemistry C, 114*, 20272-20276.

[142] **Ding, S., Zhang, D., Wu, H.B., Zhang, Z., and Lou, X. W. D.** (2012). Synthesis of micro-sized SnO_2@carbon hollow spheres with enhanced lithium storage properties, *Nanoscale, 4*, 3651-3654.

[143] **Nam, S., Kim, S., Wi, S., Choi, H., Byun, S., Choi, S. M., Yoo, S. I., Lee, K. T., and Park, B.** (2012). The role of carbon incorporation in SnO_2 nanoparticles for Li rechargeable batteries, *Journal of Power Sources, 211*, 154-160.

[144] **Chen, L., Yin, X., Mei, L., Li, C., Lei, D., Zhang, M., Li, Q., Xu, Z., Xu, C., and Wang, T.** (2012). Mesoporous SnO_2@carbon core-shell nanostructures with superior electrochemical performance for lithium ion batteries, *Nanotechnology, 23*, 035402.

[145] **Ji, L., Toprakci, O., Alcoutlabi, M., Yao, Y., Li, Y., Zhang, S., Guo, B., Lin, Z., and Zhang, X.** (2012). α-Fe_2O_3 nanoparticle-loaded carbon

nanofibers as stable and high-capacity anodes for rechargeable lithium-ion batteries, *ACS Applied Materials & Interfaces, 4*, 2672-2679.

[146] **Dirican, M., Yanilmaz, M., Fu, K., Lu, Y., Kizil, H., and Zhang, X.** (2014). Carbon-enhanced electrodeposited SnO_2/carbon nanofiber composites as anode for lithium-ion batteries, *Journal of Power Sources, 264*, 240-247.

[147] **Lin, Z., Ji, L., Woodroof, M.D., and Zhang, X.** (2010). Electrodeposited MnOx/carbon nanofiber composites for use as anode materials in rechargeable lithium-ion batteries, *Journal of Power Sources, 195*, 5025-5031.

[148] **Liu, Y., Huang, K., Fan, Y., Zhang, Q., Sun, F., Gao, T., Wang, Z., and Zhong, J.** (2013). Binder-free Si nanoparticles@carbon nanofiber fabric as energy storage material, *Electrochimica Acta, 102*, 246-251.

[149] **JunáLee, W., HoonáHwang, T., OkáHwang, J., WookáKim, H., YoungáJeong, H., HeeáHan, T., YoungáKim, J., WookáChoi, J., and OukáKim, S.** (2014). N-doped graphitic self-encapsulation for high performance silicon anodes in lithium-ion batteries, *Energy & Environmental Science, 7*, 621-626.

[150] **Fu, K., Lu, Y., Dirican, M., Chen, C., Yanilmaz, M., Shi, Q., Bradford, P.D., and Zhang, X.** (2014). Chamber-confined silicon-carbon nanofiber composites for prolonged cycling life of Li-ion battery, *Nanoscale, 6*, 7489-7495.

[151] **Jung, D. S., Hwang, T. H., Park, S. B., and Choi, J. W.** (2013). Spray drying method for large-scale and high-performance silicon negative electrodes in Li-ion batteries, *Nano Letters, 13*, 2092-2097.

[152] **Hu, Y. S., Demir-Cakan, R., Titirici, M. M., Müller, J. O., Schlögl, R., Antonietti, M., and Maier, J.** (2008)Superior storage performance of a Si@SiO_x/C nanocomposite as anode material for lithium-ion batteries, *Angewandte Chemie International Edition, 47*, 1645-1649.

[153] **Xue, L., Fu, K., Li, Y., Xu, G., Lu, Y., Zhang, S., Toprakci, O., and Zhang, X.** (2013). Si/C composite nanofibers with stable electric conductive network for use as durable lithium-ion battery anode, *Nano Energy, 2*, 361-367.

[154] **Iimura, K., Oi, T., Suzuki, M., and Hirota, M.** (2010). Preparation of silica fibers and non-woven cloth by electrospinning, *Advanced Powder Technology, 21*, 64-68.

[155] **Pirzada, T., Arvidson, S. A., Saquing, C. D., Shah, S. S., and Khan, S. A.** (2012). Hybrid silica-PVA nanofibers via sol-gel electrospinning, *Langmuir : the ACS Journal of Surfaces and Colloids, 28*, 5834-5844.

[156] **Kim, S. Y., Kim, B. H., Yang, K. S., and Kim, K. Y.** (2012). The formation of silica nanoparticles on the polyacrylonitrile-based carbon nanofibers by graphene via electrospinning, *Materials Letters, 71*, 74-77.

[157] **Yao, Y., Zhang, J., Xue, L., Huang, T., and Yu, A.** (2011). Carbon-coated SiO_2 nanoparticles as anode material for lithium ion batteries, *Journal of Power Sources, 196*, 10240-10243.

[158] **Choi, H. S., Lee, J. G., Lee, H. Y., Kim, S. W., and Park, C. R.** (2010). Effects of surrounding confinements of Si nanoparticles on Si-based anode performance for lithium ion batteries, *Electrochimica Acta, 56*, 790-796.

[159] **Xiao, J., Xu, W., Wang, D., Choi, D., Wang, W., Li, X., Graff, G. L., Liu, J., and Zhang, J. G.** (2010). Stabilization of silicon anode for Li-ion batteries, *Journal of The Electrochemical Society, 157*, A1047-A1051.

[160] **Ji, L., and Zhang, X.** (2009). Electrospun carbon nanofibers containing silicon particles as an energy-storage medium, *Carbon, 47*, 3219-3226.

[161] **Ding, Y. S., Li, W. N., Iaconetti, S., Shen, X. F., DiCarlo, J., Galasso, F. S., and Suib, S. L.** (2006) Characteristics of graphite anode modified by CVD carbon coating, *Surface and Coatings Technology, 200*, 3041-3048.

[162] **Su, L., Zhou, Z., and Ren, M.** (2010). Core double-shell $Si@SiO_2@C$ nanocomposites as anode materials for Li-ion batteries, *Chemical Communications, 46*, 2590-2592.

[163] **Kim, C., Park, S. H., Cho, J. I., Lee, D. Y., Park, T. J., Lee, W. J., and Yang, K. S.** (2004). Raman spectroscopic evaluation of polyacrylonitrile-based carbon nanofibers prepared by electrospinning, *Journal of Raman Spectroscopy, 35*, 928-933.

[164] **Meier, C., Lüttjohann, S., Kravets, V. G., Nienhaus, H., Lorke, A., and Wiggers, H.** (2006). Raman properties of silicon nanoparticles, *Physica E: Low-Dimensional Systems and Nanostructures, 32*, 155-158.

[165] **Li, Z., Gao, W., Meng, A., Geng, Z., and Gao, L.** (2008). Large-scale synthesis and raman and photoluminescence properties of single crystalline β-SiC nanowires periodically wrapped by amorphous SiO_2 nanospheres 2, *The Journal of Physical Chemistry C, 113*, 91-96.

[166] **Wang, J., Zhao, H., He, J., Wang, C., and Wang, J.** (2011). Nano-sized SiO_x/C composite anode for lithium ion batteries, *Journal of Power Sources, 196*, 4811-4815.

[167] **Gwon, H., Kim, H. S., Lee, K. U., Seo, D. H., Park, Y. C., Lee, Y. S., Ahn, B. T., and Kang, K.** (2011). Flexible energy storage devices based on graphene paper, *Energy & Environmental Science, 4*, 1277-1283.

[168] **Wang, J. Z., Zhong, C., Chou, S. L., and Liu, H. K.** (2010). Flexible free-standing graphene-silicon composite film for lithium-ion batteries, *Electrochemistry Communications, 12*, 1467-1470.

[169] **Chew, S. Y., Ng, S. H., Wang, J., Novák, P., Krumeich, F., Chou, S. L., Chen, J., and Liu, H. K.** (2009). Flexible free-standing carbon nanotube films for model lithium-ion batteries, *Carbon, 47*, 2976-2983.

[170] **Noerochim, L., Wang, J. Z., Chou, S. L., Wexler, D., and Liu, H. K.** (2012). Free-standing single-walled carbon nanotube/SnO_2 anode paper for flexible lithium-ion batteries, *Carbon, 50*, 1289-1297.

[171] **Li, N., Chen, Z., Ren, W., Li, F., and Cheng, H. M.** (2012). Flexible graphene-based lithium ion batteries with ultrafast charge and discharge rates, *Proceedings of the National Academy of Sciences, 109*, 17360-17365.

[172] **Wang, B., Li, X., Zhang, X., Luo, B., Jin, M., Liang, M., Dayeh, S. A., Picraux, S., and Zhi, L.** (2013). Adaptable silicon-carbon nanocables sandwiched between reduced graphene oxide sheets as lithium ion battery anodes, *ACS Nano, 7*, 1437-1445.

[173] **Jiang, H., Zheng, Z., Li, Z., and Wang, X.** (2006). Effects of temperature and solvent on the hydrolysis of alkoxysilane under alkaline conditions, *Industrial & Engineering Chemistry Research, 45*, 8617-8622.

[174] **Pol, V., Pol, S., George, P., Markovsky, B., and Gedanken, A.** (2006). Synthesis of a conducting SiO_2-carbon composite from commercial silicone grease and its conversion to paramagnetic SiO_2 particles, *The Journal of Physical Chemistry B, 110*, 13420-13424.

[175] **Lee, B. S., Son, S. B., Seo, J. H., Park, K. M., Lee, G., Lee, S. H., Oh, K. H., Ahn, J. P., and Yu, W. R.** (2013). Facile conductive bridges formed between silicon nanoparticles inside hollow carbon nanofibers, *Nanoscale, 5*, 4790-4796.

[176] **Li, Y., Guo, B., Ji, L., Lin, Z., Xu, G., Liang, Y., Zhang, S., Toprakci, O., Hu, Y., Alcoutlabi, M., and Zhang, X.** (2013). Structure control and performance improvement of carbon nanofibers containing a dispersion of silicon nanoparticles for energy storage, *Carbon, 51*, 185-194.

[177] **Dirican, M., Yanilmaz, M., Fu, K., Yildiz, O., Kizil, H., Hu, Y., and Zhang, X.** (2014). Carbon-confined PVA-derived silicon/silica/carbon nanofiber composites as anode for lithium-ion batteries, *Journal of The Electrochemical Society, 161*, A2197-A2203.

[178] **Xie, J., Yang, X., Zhou, S., and Wang, D.** (2011). Comparing one-and two-dimensional heteronanostructures as silicon-based lithium ion battery anode materials, *ACS Nano, 5*, 9225-9231.

[179] **Yu, B. C., Hwa, Y., Park, C. M., Kim, J. H., and Sohn, H. J.** (2013). Effect of oxide layer thickness to nano-Si anode for Li-ion batteries, *RSC Advances, 3*, 9408-9413.

CURRICULUM VITAE

Name Surname: Mahmut Dirican

Place and Date of Birth: Merzifon-14.01.1983

E-Mail: mdirican@itu.edu.tr

EDUCATION:

B.Sc.: 2007, Ege University, Faculty of Engineering, Textile Engineering

M.Sc.: 2010, Istanbul Technical University, Faculty of Textile Technologies and Design, Textile Engineering

PROFESSIONAL EXPERIENCE AND REWARDS:

Research Assistant, Istanbul Technical University,
Department of Nano Science and Nano Engineering (2012-….)

Visiting Scholar, North Carolina State University
Department of Textile Engineering, Chemistry, and Science (2013-2015)

R&D Manager, Ozen Mensucat, Inc., Istanbul, Turkey
(Textile Dyeing and Finishing Company) (2007-2012)

PUBLICATIONS, PRESENTATIONS AND PATENTS ON THE THESIS:

- **M. Dirican**, M. Yanilmaz, K. Fu, Y. Lu, H. Kizil, X. Zhang, Carbon-Enhanced Electrodeposited SnO_2/Carbon Nanofiber Composites as Anode for Lithium-Ion Batteries, *Journal of Power Sources*, 264 (2014) 240-247.

- **M. Dirican,** M. Yanilmaz, K. Fu, O. Yildiz, H. Kizil, Y. Hu, X. Zhang, Carbon-Confined PVA-Derived Silicon/Silica/Carbon Nanofiber Composites as Anode for Lithium-Ion Batteries, *Journal of The Electrochemical Society*, 161 (2014) A2197-A2203.

- **M. Dirican**, O. Yildiz, Y. Lu, X. Fang, H. Jiang, H. Kizil, Y. Hu, X. Zhang, Flexible Binder-Free Silicon/Silica/Carbon Nanofiber Composites as Anode for Lithium-Ion Batteries, *Electrochimica Acta*, 169 (2015) 52-60.

- **M. Dirican**, Y. Lu, K. Fu, H. Kizil, X. Zhang, SiO_2-Confined Silicon/Carbon Nanofiber Composites as An Anode for Lithium-Ion Batteries, *RSC Advances*, 5 (2015) 34744-34751.

OTHER PUBLICATIONS, PRESENTATIONS AND PATENTS:

- M. Yanilmaz, Y. Lu, **M. Dirican**, K. Fu, X. Zhang, Nanoparticle-on-nanofiber hybrid membrane separators for lithium-ion batteries via combining electrospraying and electrospinning techniques, *Journal of Membrane Science*, 456 (2014) 57-65.

- K. Fu, Y. Lu, **M. Dirican**, C. Chen, M. Yanilmaz, Q. Shi , P. D. Bradford, X. Zhang, Chamber-confined silicon-carbon nanofiber composites for prolonged cycling life of Li-ion batteries, *Nanoscale*, 6, (2014) 7489-7495.

- M. Yanilmaz, **M. Dirican**, X. Zhang, Evaluation of Electrospun SiO_2/Nylon 6,6 Nanofiber Membranes as a Thermally-Stable Separator for Lithium-Ion Batteries, *Electrochimica Acta,* 133 (2014) 501-508.

- K. Fu, Y. Li, **M. Dirican**, C. Chen, Y. Lu, J. Zhu, Y. Li, L. Cao , P. D. Bradford, X. Zhang, Sulfur Gradient-Distributed CNF Composite: A Self-Inhibiting Cathode for Binder-Free Lithium-Sulfur Batteries, *Chemical Communications,* 50 (2014) 10277-10280.

- **M. Dirican**, M. Yanilmaz, X. Zhang, Free-Standing Polyaniline-Porous Carbon Nanofiber Electrodes for Symmetric and Asymmetric Supercapacitors, *RSC Advances*, 4 (2014) 59427-59435.

- H. Jiang, Y. Ge, K. Fu, Y. Lu, C. Chen, J. Zhu, **M. Dirican**, X. Zhang, Centrifugally-Spun Tin-Containing Carbon Nanofibers as Anode Material for Lithium-Ion Batteries, *Journal of Materials Science*, 50 (2014) 1094-1102.

- Y. Lu, K. Fu, S. Zhang, Y. Li, C. Chen, J. Zhu, M. Yanilmaz, **M. Dirican**, X. Zhang, Centrifugal Spinning: A Novel Approach to Fabricate Porous Carbon Fibers as Binder-Free Electrodes for Electric Double-Layer Capacitors, *Journal of Power Sources*, 273 (2015) 502-510.

- **M. Dirican**, Y. Lu, Y. Ge, O. Yildiz, X. Zhang, Carbon-Confined SnO_2-Electrodeposited Porous Carbon Nanofiber Composite as High-Capacity Sodium-Ion Battery Anode Material, *ACS Applied Materials & Interfaces,* 2015 (Accepted Manuscript)